

A Dissertation

entitled

Structure and Enzymatic Characterization of *Mycobacterium tuberculosis* Transferases

by

Lorenza Favrot

Submitted to the Graduate Faculty as partial fulfillment of the requirements for the

Doctor of Philosophy Degree in Chemistry

Dr. Donald R. Ronning, Committee Chair

Dr. John J. Bellizzi, Committee Member

Dr. Steven J. Sucheck, Committee Member

Dr. Choong-Min Kang, Committee Member

Dr. Patricia R. Komuniecki, Dean
College of Graduate Studies

The University of Toledo

August 2014

Copyright 2014, Lorenza Favrot

This document is copyrighted material. Under copyright law, no parts of this document may be reproduced without the expressed permission of the author.

An Abstract of
Structure and Enzymatic Characterization of *Mycobacterium tuberculosis* Transferases

by

Lorenza Favrot

Submitted to the Graduate Faculty as partial fulfillment of the requirements for the
Doctor in Philosophy Degree in
Chemistry

The University of Toledo

August 2014

Tuberculosis (TB) remains the second leading cause of death from an infectious disease after human immunodeficiency virus (HIV). The bacterium that causes TB infects one third of the world's population. In 2012, nearly 9 million persons developed an active infection and 1.3 million perished from this disease. The infectious disease predominantly affects developing countries in which access to healthcare is difficult. The TB treatment regimen typically requires a combination of several drugs and lasts between 6 and 9 months. Patient noncompliance and difficulty in accessing the treatments lead to the burden of multi, extensively and even totally drug-resistant TB. Co-infection with HIV arises as another challenge, as several common antiviral drugs are not compatible with TB treatments. For these reasons, it is critical to find new drug targets and identify new antitubercular compounds to improve TB treatment. These issues also emphasize the need to understand the protection mechanisms that the organism utilizes to survive the host's immune system.

The mycobacterial cell wall is essential for the survival of *Mycobacterium tuberculosis* (*M. tb*) as it forms an impermeable barrier that prevents the entry of many

potential antibiotics. The Antigen 85 complex (Ag85) consists of three secreted enzymes that play a role in the cell wall biosynthesis. The three mycolyltransferases catalyze the attachment of mycolic acids to either the arabinogalactan (AG) to form the mycolylarabinogalactan (mAG) or to trehalose monomycolate (TMM) to produce the cord factor trehalose dimycolate (TDM). The genes encoding the Ag85 proteins are synthetically lethal; two Ag85 enzymes are required for the viability of *M. tb*. Additionally, the inactivation of one enzyme among the Ag85 complex affects the mycobacterial cell growth and the cell envelope integrity is altered. Taken together, these facts demonstrate that the Ag85 complex is a valuable TB drug target. The development of a high-throughput fluorometric assay allowed the identification of a potent inhibitor of the Ag85 complex called ebselen. TDM and mAG biosynthesis are inhibited by ebselen in culture-based studies, implying that the Ag85 complex is the major target of ebselen *in vivo*. Mass spectrometry and X-ray crystallographic experiments led to the determination of its mechanism of action. The compound acts as an allosteric and suicide inhibitor of the Ag85 complex. A lone cysteine residue located near the active site is covalently modified by ebselen. Although this cysteine is not important for the catalytic reaction performed by the enzymes, the residue plays a significant structural feature. Modifications of the residue by any thiol-reactive compound or mutation at this position alter the active site structure by disrupting the hydrogen-bonding network between the catalytic triad residues. The same inactive conformation is observed when any residue of the catalytic triad is mutated.

M. tb can also enter a latent phase under environmental stresses such as low oxygen availability or low pH. *M. tb* slows down its growth but remains viable. Most

antibiotics used to treat TB target replicating bacteria. In a dormant state, the bacteria become tolerant to the antibiotics, challenging the treatment of TB. To reach latency, *M. tb* alters its metabolism. The tricarboxylic acid (TCA) cycle plays an important role in the metabolism of *M. tb*. The citrate synthase enzyme is involved in the first step of the TCA cycle and catalyzes the formation of citrate from acetyl-CoA (AcCoA) and oxaloacetate. Little is known about this enzyme. To gain more insight about this enzyme, we solved the X-ray crystal structure of *M. tb* citrate synthase in complex with oxaloacetate. We also developed an absorbance-based assay to characterize the enzyme using steady-state kinetic.

Finally, unlike many other bacteria, *M. tb* thrives following phagocytosis by human macrophages. This characteristic differentiates pathogenic mycobacteria and non-pathogenic species such as *Mycobacterium smegmatis*. Although it is known that *M.tb* actively prevents phagosome-lysosome fusion, the mechanism by which it resists macrophage killing has not been fully characterized. While the Enhanced Intracellular Survival (Eis) protein is known to play a role in modulating the immune response and autophagocytosis in macrophages, no studies to date have succeeded in unambiguously identifying its molecular function in pathogenesis. To aid in identifying the function of Eis and its likely substrates, we have solved the crystal structure of the *M. tb* encoded Eis protein. This structure has confirmed the previous hypothesis that Eis is a member of the GCN5 superfamily of N-acetyltransferases (GNAT): the acetyl moiety from AcCoA is transferred to an amine of an acetyl acceptor. We also attempted to identify the co-substrate of Eis *in vivo* using diverse tools such as profiling experiments and mass spectrometry.

Acknowledgements

First, I would like to thank my advisor Dr. Donald Ronning who kindly trained me for the past five years and shared with me endless knowledge and numerous skills. Thank you for your patience, your enthusiasm and your guidance. I would also like to extend my gratitude to my committee members Dr. John Bellizzi, Dr. Steven Sucheck and Dr. Choong-Min Kang for their valuable suggestions and support.

I would like to acknowledge the members from Dr. Ronning's laboratory, past and present, particularly Vidhi, Jared, Erica, Mike, Cecile, Thomas and Chris. Thank you for all the fun times and laughs we shared. An immense thank you to Vidhi for her constant support and her friendship. I would like to extend my gratitude to Dr. Julie Boucau for all the advice she gave me when I first started my graduate research. I also would like to acknowledge Nathan Howell, an undergraduate who helped me in the early stages of the citrate synthase project, and Sandeep Thanna from Dr. Sucheck's group, who synthesized compounds for the Antigen 85 project.

I would like to thank the entire department of chemistry for welcoming me among them and for all of the help those persons provided to me throughout the years.

Last but not least, I would like to thank my family, especially my Mom who constantly supported all my decisions. And thank you to my grandfather; I hope he would be proud of me if he were still with us. I could not have done it without both of you.

Table of Contents

Abstract.....	iii
Acknowledgements.....	vi
Table of Contents.....	vii
List of Tables	xii
List of Figures.....	xiii
List of Equations.....	xvii
List of Abbreviations	xviii
List of Symbols.....	xxi
1 Introduction	1
1.1 Background on Tuberculosis	1
1.1.1 Tuberculosis in numbers.....	1
1.1.2 Pathogenesis.....	2
1.1.3 Treatments.....	3
1.1.4 Challenge of drug resistance and co-infection with HIV.....	5
1.2 Characterization of <i>M. tb</i>	6
1.2.1 <i>M. tb</i> organism	6
1.2.2 Description of the mycobacterial cell wall	6
1.2.3 Significance of the mycobacterial cell envelope as a drug target.....	9
1.3 Overview and significance of the different projects.....	10

1.3.1	Antigen 85 complex.....	10
1.3.2	Citrate Synthase.....	10
1.3.3	Enhanced Intracellular Survival protein	11
2	Characterization of the inhibitory mechanism of Ag85 complex by ebselen.....	12
2.1	Background.....	12
2.1.1	Antigen 85 complex.....	12
2.1.2	Antigen 85 complex as a validated drug target.....	15
2.1.3	Research aims	16
2.2	Experimental procedures	18
2.2.1	Molecular cloning.....	18
2.2.2	Protein purification of Ag85s and mutants	19
2.2.3	Ag85C fluorescence-based assay.....	21
2.2.4	Mass spectrometry	22
2.2.5	Crystallization.....	23
2.2.6	Structure determination.....	23
2.3	Results and discussion	24
2.3.1	Ebselen as a potent Ag85C inhibitor <i>in vitro</i> and <i>in vivo</i>	24
2.3.2	Ebselen binds covalently to C209 of Ag85C.....	26
2.3.3	C209 modifications lead to a significant loss in Ag85C activity.....	32
2.3.4	C209 mutants display a nearly complete loss in Ag85C activity	36
2.3.5	Ebselen disrupts the Ag85C active site structure.....	38
2.3.6	Screening of Ebsulfur and Ebsulfur derivatives	45
2.3.7	Screening of Ebselen derivatives.....	49

	2.4 Conclusion and future work.....	51
3	A novel approach to target the <i>M. tb</i> Ag85 complex.....	53
	3.1 Background.....	53
	3.2 Experimental procedures	54
	3.2.1 Molecular cloning.....	54
	3.2.2 Protein purification of Ag85s and mutants	55
	3.2.3 Enzymatic activity assay.....	55
	3.2.4 Crystallization and structure determination.....	56
	3.3 Results and discussion	58
	3.3.1 Modification of C209 by thiol reactive compounds triggers structural changes in the Ag85C active site.....	58
	3.3.2 Ag85C-C209G mutant displays a similar inactive conformation.....	65
	3.3.3 Mutation of any catalytic triad residue results in a loss of enzymatic activity and relaxation of helix α 9.....	68
	3.3.4 Further work: Ag85A and Ag85B-S126A.....	74
	3.4 Conclusion and future work.....	76
4	Citrate Synthase	78
	4.1 Background.....	78
	4.1.1 Tricarboxylic acid cycle.....	78
	4.1.2 Role of citrate synthase.....	80
	4.1.3 Tricarboxylic cycle and citrate synthase in <i>M. tb</i>	82
	4.2 Experimental procedures	85
	4.2.1 Cloning of <i>citA</i>	85

4.2.2	Purification of Citrate Synthase	87
4.2.3	Preparation of a selenomethionine derivatized protein.....	90
4.2.4	Mass spectrometry	91
4.2.5	Absorbance-based assay	92
4.2.6	Crystallization studies.....	93
4.2.7	Single-wavelength anomalous dispersion experiment.....	94
4.3	Results and discussion	95
4.3.1	Identification of a contaminant using mass spectrometry.....	95
4.3.2	Development of an absorbance-based assay.....	97
4.3.2.1	Kinetic parameters determination.....	97
4.3.2.2	Z' value determination.....	102
4.3.2.3	Test inhibition of citrate synthase by NADH	103
4.3.3	Determination of citrate synthase structure	104
4.3.3.1	Citrate synthase in complex with oxaloacetate.....	104
4.3.3.2	Crystallization attempts with CoA and citrate.....	113
4.4	Conclusion and future work.....	116
5	Enhanced intracellular survival protein as a potential <i>M. tb</i> therapeutic target...117	
5.1	Background.....	117
5.2	Experimental procedures	121
5.2.1	Purification of Eis	121
5.2.2	Crystallization studies.....	124
5.2.3	Structure determination of Eis	124
5.2.4	Identification of Eis co-substrate <i>in vivo</i> : first approach	125

5.2.4.1	Analogs of myristoylCoA and AcCoA: synthesis	125
5.2.4.2	Cloning and purification of Green Fluorescent Protein ...	126
5.2.4.3	Proteomic experiment using CoA analogs and GFP.....	128
5.2.5	Identification of Eis co-substrate <i>in vivo</i> : second approach.....	129
5.2.5.1	Bisubstrate inhibitor approach	129
5.2.5.2	Substrate profiling experiment.....	129
5.3	Results and discussion	130
5.3.1	Solving Eis structure	130
5.3.2	Identification of Eis co-substrate <i>in vivo</i> : first approach	135
5.3.3	Identification of Eis co-substrate <i>in vivo</i> : second approach.....	139
5.3.3.1	Preliminary results	139
5.3.3.2	Bisubstrate inhibitor approach	140
5.3.3.3	Substrate profiling experiment.....	141
5.4	Conclusion	143
	References.....	145

List of Tables

1.1	First-line and second-line drugs currently used in TB treatment regimen.....	4
2.1	Primers used for site-directed mutagenesis on pET29- <i>fbpC</i>	18
2.2	Peptide mass fingerprinting of Ag85C incubated with ebselen	31
2.3	Peptide mass fingerprinting of Ag85C incubated with IAA.....	34
2.4	Data collection and refinement statistics	45
3.1	Primers used for site-directed mutagenesis on pET29- <i>fbpC</i>	55
3.2	Data collection and refinement statistics for Ag85C-IAA/Hg/ebselen.....	64
3.3	Data collection and refinement statistics for Ag85C-C209G	66
3.4	Data collection and refinement statistics for Ag85C-E228Q and H260Q.....	70
4.1	Primers used for the amplification of <i>citA</i> gene.....	85
4.2	Data collection and refinement statistics for citrate synthase.....	106
5.1	Primers used for the amplification of <i>gfp</i> gene.....	126
5.2	Data collection, phasing and refinement statistics.....	131
5.3	Bioinformatic analysis of the preliminary structure of Eis.....	135

List of Figures

1-1	Scheme of the mycobacterial cell wall	8
2-1	Roles of the different Ag85 enzymes.....	13
2-2	Ag85C structure and mechanism	14
2-3	Ag85C fluorescent-based assay	17
2-4	Purification of Ag85C.....	20
2-5	Kirby-Bauer diffusion disk assay.....	25
2-6	Hypothetic mechanism of Ag85C inhibition by ebselen	27
2-7	Modification of Ag85C by ebselen.....	28
2-8	Modification of Ag85A and Ag85B by ebselen	29
2-9	Deconvoluted mass spectra of Ag85C-C209S.....	30
2-10	Deconvoluted mass spectrum of Ag85C-ebselen treated with DTT	32
2-11	Reversibility of Ag85C inhibition by ebselen.	33
2-12	Modification of Ag85C by IAA.....	35
2-13	Time course of Ag85C inhibition by ebselen	35
2-14	Potential mutations of C209 residue and effects on enzymatic activity	37
2-15	Close up view of Ag85C active site.....	39
2-16	Stereo view for the disordered region observed near the C209 residue.	40
2-17	Superimposition of Ag85C, Ag85C-DEP and Ag85C-EBS.....	42

2-18	Superimposition of Ag85C-DEP, Ag85C-EBS and Ag85C-C209S	44
2-19	Screening of ebsulfur derivatives.....	46
2-20	KU198 and KU251 dose-dependences	47
2-21	Crystals of Ag85C-KU198 grown in presence of different additives.....	48
2-22	Time course experiment with the different ebselen analogs.....	50
3-1	Ag85C-ebselen structure.....	59
3-2	Ag85C-IAA and Ag85C-Hg structures	62
3-3	Inhibition of Ag85C by <i>p</i> -chloromercuribenzoic acid.....	63
3-4	Superimposition of Ag85C, Ag85C-EBS, Ag85C-C209S and Ag85C-C209G....	67
3-5	Effect of mutations among the catalytic triad residues.....	69
3-6	Superimposition of Ag85C-S124A, Ag85C-E228Q and Ag85C-H260Q	72
3-7	Ag85A-S126A and Ag85B-S126A crystals	76
4-1	Scheme of the TCA cycle	79
4-2	Reaction catalyzed by citrate synthase	80
4-3	Citrate synthase mechanism.....	81
4-4	Sequencing results of pET32- <i>citA</i>	86
4-5	Chromatogram from cobalt affinity purification of citrate synthase	88
4-6	Chromatogram and SDS-PAGE gel size exclusion chromatography of citrate synthase.....	89
4-7	Purification of selenomethionine derivatized citrate synthase.....	91
4-8	SDS-PAGE gel of citrate synthase after purification	95
4-9	Amino acids sequence of <i>M. tb</i> citrate synthase.....	96
4-10	Scheme of <i>M. tb</i> citrate synthase absorbance-based assay	97

4-11	Enzymatic activity test of <i>M. tb</i> citrate synthase	98
4-12	Michaelis-Menten curves for oxaloacetate	100
4-13	Michaelis-Menten curve for AcCoA	101
4-14	Crystals of <i>M. tb</i> citrate synthase	105
4-15	Overall structure of selenomethionine derivatized citrate synthase	107
4-16	Comparison of <i>T. thermophilus</i> and <i>M. tb</i> citrate synthase structures	109
4-17	Superimposition of <i>T. thermophilus</i> and <i>M. tb</i> citrate synthase momomers	110
4-18	Sequence alignment of <i>M. tb</i> citrate synthase with <i>E. coli</i> citrate synthase	111
4-19	Superimposition of <i>E. coli</i> and <i>M. tb</i> citrate synthase momomers	112
4-20	Crystals of citrate synthase with citrate and CoA	114
4-21	Crystals of citrate synthase with CoA	115
5-1	Sequence alignment of Eis with AvGNAT	119
5-2	Proposed N-acetyltransferase mechanism	120
5-3	Chromatogram and SDS-PAGE gel from nickel affinity purification of Eis	122
5-4	Chromatogram and SDS-PAGE gel from anion exchange purification of Eis	123
5-5	General scheme for the synthesis of AcCoA and myristoyl-CoA analogs	125
5-6	SDS-PAGE gel showing purity of GFP after nickel affinity purification	127
5-7	Crystals of Eis co-crystallized in presence of different concentrations of CoA	130
5-8	Comparison of Eis and AvGNAT	132
5-9	Active site of Eis	133
5-10	New crystals of Eis co-crystallized with CoA and KAN	134
5-11	First approach to identify Eis co-substrate <i>in vivo</i>	138
5-12	2D Western Blot gels	139

5-13	Proposed experimental scheme for the identification of the acetyl acceptor.....	140
5-14	SDS-PAGE corresponding to substrate profiling experiment	142

List of Equations

4-1	Michaelis-Menten equation	99
4-2	Substrate inhibition equation	101
4-3	Z'-factor	102

List of Abbreviations

Abs.....	Absorbance
AcCoA.....	Acetyl coenzyme A
Add.....	Additive
ADP.....	Adenine diphosphate
AG.....	Arabinogalactan
Ag85.....	Antigen 85
Alk-CoA.....	Tetradec-13-ynoyl-Coenzyme A
AMK.....	Amikacin
APS-ANL.....	Advance Photon Source Argonne National Laboratory
ATP.....	Adenine triphosphate
βME.....	β-mercaptoethanol
BCG.....	Bacille-Calmette-Guérin
CHCA.....	α-Cyano-4-hydroxycinnamic acid
ClAc-CoA.....	Chloroacetyl coenzyme A
CMC.....	Critical Micelle Concentration
CoA.....	Coenzyme A
CO ₂	Carbon dioxide
Cond.....	Condition
DDAO.....	N,N-dimethyldodecylamine N-oxide
DMSO.....	Dimethyl sulfoxide
DTNB.....	5,5'-dithio-bis-(2-nitrobenzoic acid)
DTT.....	Dithiothreitol
Det.....	Detergent
EBS.....	Ebselen
<i>E. coli</i>	<i>Escherichia coli</i>
EDTA.....	Ethylenediaminetetraacetic acid
Eis.....	Enhanced Intracellular Survival protein
eLBOW.....	electronic Ligand Builder and Optimization Workbench
EMB.....	Ethambutol
EPMR.....	Evolutionary Program for Molecular Replacement
ESI.....	Electrospray ionization

ETH.....	Ethionamide
FADH ₂	Flavin adenine dinucleotide
<i>fbp</i>	Fibronectin-binding protein
GDP.....	Guanosine diphosphate
GFP.....	Green fluorescent protein
GTP.....	Guanosine triphosphate
HIV.....	Human Immunodeficiency Virus
HEPES.....	2-[4-(2-hydroxyethyl)piperazin-1-yl]ethanesulfonic acid
HTG.....	n-heptyl-β-D-thioglucopyranoside
IAA.....	Iodoacetamide
INH.....	Isoniazid
IPTG.....	Isopropyl β-D-1-thiogalactopyranoside
KAN.....	Kanamycin
KCl.....	Potassium chloride
keV.....	kiloelectron volt
LAM.....	Lipoarabinomannan
LC.....	Liquid Chromatography
LS-CAT.....	Life Sciences Collaborative Access Team
mAGP.....	Mycolyl-arabinogalactan-peptidoglycan complex
MAD.....	Multiwavelength Anomalous Dispersion
MALDI.....	Matrix-assisted laser desorption/ionization
MAME.....	Cell wall-bound mycolic acids
<i>M. bovis</i>	<i>Mycobacterium bovis</i>
MDR.....	Multidrug-resistant
MgCl ₂	Magnesium chloride
MIC.....	Minimum Inhibitory Concentration
MME.....	Monomethyl ether
MOM.....	Mycobacterial outer membrane
MPD.....	(+/-)-2-methyl-2,4-pentanediol
MS.....	Mass spectrometry
<i>M. smegmatis</i>	<i>Mycobacterium smegmatis</i>
<i>M.tb</i>	<i>Mycobacterium tuberculosis</i>
NaCl.....	Sodium chloride
NADH.....	Nicotinamide adenine dinucleotide
NDDS.....	n-dodecanoylsucrose
NDS.....	n-decanoylsucrose
NIH.....	National Institutes of Health
NOS.....	n-octanoylsucrose

OD.....	Optical Density
OG.....	n-octyl- β -D-glucoside
OTG.....	n-octyl- β -D-thioglucoside
PEG.....	Polyethylene glycol
PDIM.....	Phthiocerol dimycocerosate
PG.....	Peptidoglycan
PGL.....	Phenolic glycolipids
PIM.....	Phosphatidylinositol mannosides
PZA.....	Pyrazinamide
Q-TOF.....	Quadripole Time-of-Flight
RMP.....	Rifampicin
RMS.....	Root Mean Square
ROS.....	Reactive oxygen species
SAD.....	Single-wavelength Anomalous Dispersion
SDS-PAGE.....	Sodium dodecyl sulfate polyacrylamide gel electrophoresis
TB.....	Tuberculosis
TCA.....	Tricarboxylic acid (cycle)
TCEP.....	Tris(2-carboxyethyl)phosphine
TDM.....	Trehalose dimycolate
TFA.....	Trifluoroacetic acid
THF.....	Tetrahydrofuran
TMM.....	Trehalose monomycolate
<i>T. thermophilus</i>	<i>Thermus thermophilus</i>
WHO.....	World Health Organization
WT.....	Wild-type (enzyme)
XDR.....	Extensively drug-resistant

List of Symbols

Å.....	Angstrom
°C.....	degree Celsius
M.....	molar
mg.....	milligrams
mL.....	milliliter
mM.....	millimolar
nm.....	nanometer
nM.....	nanomolar
pH.....	potential hydrogen
rpm.....	revolution per minute
µM.....	micromolar
v/v.....	volume/volume
w/v.....	weight/volume

Chapter 1

Introduction

1.1 Background on Tuberculosis (TB)

1.1.1 Tuberculosis in numbers

Tuberculosis (TB) is still one of the most important health problems worldwide. Indeed, TB is responsible for more deaths each year than any other bacterial disease and remains the second leading cause of death from an infectious disease, with the first being human immunodeficiency virus (HIV)²⁶. TB typically results from an infection caused by *Mycobacterium tuberculosis* (*M. tb*). The disease affects mainly the lungs. In healthy individuals, the infection enters into a latent stage that can last for many years. Among the 2 billion people infected around the world, approximately 9 million people per year develop an active infection²⁶. The World Health Organization (WHO) reported 1.3 million TB deaths in 2012²⁶. 25 % of these deaths occurred among HIV-positive patients. The highest rate of cases/deaths occurred in South-East Asia, China, India, and Africa. For instance, South Africa, Namibia or Mozambique exhibit more than 500 new cases of TB per 100,000 population every year²⁶. The disease predominantly affects third-world countries in which access to treatments is difficult.

1.1.2 Pathogenesis

As mentioned in the previous section, the organism *M. tb* is the causative agent for human TB. The disease is transmitted through aerosolization; the infection is initiated by inhaling aerosol droplets containing the bacilli²⁷. Then the bacilli travel to the lungs where the bacteria are recruited within the alveolar macrophages via phagocytosis. The normal step after entry within a macrophage would be formation of the phagosomal envelope around the foreign molecule²⁸. However, the pathogenic mycobacteria *M.tb* possess the ability to thrive following phagocytosis by human macrophages. The mechanism by which the mycobacterium is able to survive macrophage killing is not yet completely understood, although several mechanisms have been hypothesized such as the inhibition of phagosome-lysosome fusion or inhibition of phagosome acidification²⁹⁻³¹.

In a majority of cases, the infection is latent and the infected person does not exhibit any symptoms. The active infection generally presents the following symptoms: chest pain, cough (often with blood and sputum), fever, fatigue, weight loss, loss of appetite, and night sweats. Active TB leads to the eventual formation of granulomas within the lungs. The Mantoux tuberculin skin test, blood testing, sputum smear microscopy or chest radiography can be used to diagnose a TB infection.

In some rare cases (about 10 % of the new cases diagnosed in 2012), infected macrophages travel to other organs, resulting in an extrapulmonary TB²⁶.

1.1.3 Treatments

In the 1920's, a vaccine called bacillus Calmette-Guerin or BCG was developed³². This vaccine was derived from a non-pathogenic strain of *Mycobacterium bovis* (*M. bovis*). The BCG vaccine is usually used as prevention against TB and is distributed for infants, but it does not treat the disease once a person is infected. No other vaccine has been approved for human use since.

Later, TB was treated with streptomycin^{16, 17}. However, strains resistant to streptomycin emerged very quickly¹⁷. Following this failure, new antibiotics were discovered and used to treat TB. These drugs and their targets are summarized in table 1-1. These drugs are commonly classified into three groups: first-line, second-line and third-line drugs. The typical treatment regimen includes isoniazid (INH), rifampicin (RMP), ethambutol (EMB) and pyrazinamide (PZA). Second-line drugs include aminoglycosides (amikacin, kanamycin, etc.), polypeptides (capreomycin, viomycin, etc.), thioamides (ethionamide) or fluoroquinolones (levofloxacin, ofloxacin, etc.). Some examples of third-line drugs are thioacetazone, macrolides or clofazimine. TB treatments generally last from 6 to 9 months. Second-line drugs are used when a patient does not respond to the first-line treatment. However, these drugs often exhibit increased toxicity and lower efficiency than the first-line, leading to longer, riskier treatment duration^{33,34}. The third-line drugs are not often used because their efficacy has often not been proven.

It is notable that all the drugs used to treat TB have been discovered in the 1950's and 1960's. No new major drug has been brought to the market since the 1970's. With the emergence of major challenges that will be discussed in the following section, current

research is focusing on the discovery of new drug targets and new drugs to use in the treatment of TB.

Table 1-1: First-line and second-line drugs currently used in TB treatment regimen. Adapted from Zumla *et al.*, *Nat. Rev. Drug Discov.*, 2013¹.

Drug (Year of discovery)	Target	Inhibits
<i>First-line drugs</i>		
INH (1952)	Enoyl-[acyl-carrier-protein]reductase	Mycolic acid biosynthesis ^{2, 3}
RMP (1963)	RNA polymerase, β subunit	Transcription ⁴⁻⁶
PZA (1954)	S1 component of 30S ribosomal subunit	Translation and <i>trans</i> -translation, acidifies cytoplasm ^{7, 8}
EMB (1961)	Arabinosyl transferase	Arabinogalactan biosynthesis ⁹⁻¹²
<i>Second-line drugs</i>		
<i>p</i> -amino salicylic acid (1948)	Dihydropteroate synthase	Folate biosynthesis ¹³⁻¹⁵
Streptomycin (1944)	S12 and 16S rRNA components of 30S ribosomal subunit	Protein synthesis ¹⁶⁻¹⁸
Ethionamide or ETH (1961)	Enoyl-[acyl-carrier-protein]reductase	Mycolic acid biosynthesis ^{2, 19, 20}
Ofloxacin (1980)	DNA gyrase and DNA topoisomerase	DNA supercoiling ²¹
Capreomycin (1963)	Interbridge B2a between 30S and 50S ribosomal subunits	Protein synthesis ²²
Kanamycin (1957)	30S ribosomal subunit	Protein synthesis ²⁴
Amikacin (1972)	30S ribosomal subunit	Protein synthesis ²²
Cycloserine (1955)	D-alanine racemase and ligase	Peptidoglycan synthesis ²⁵

1.1.4 Challenge of drug resistance and co-infection with HIV

Treatment for TB typically lasts 6 to 9 months and requires the combination of several drugs. As mentioned previously, TB affects mainly developing countries, most notably Africa and South-East Asia, where access to healthcare or treatment is often difficult²⁶. Patient noncompliance leads to the emergence of drug-resistance such as multidrug-resistant TB (MDR-TB) and extensively drug-resistant (XDR-TB). MDR-TB strains are resistant to INH and RMP at least while XDR-TB strains are resistant to these first-line drugs in addition to several of the second-line drugs. Recently, totally drug-resistant strains have been discovered, and such strains do not respond to any known treatments³⁵. The WHO reported an estimated 450,000 cases of MDR-TB and 170,000 deaths from MDR-TB in 2012²⁶. Treatment of MDR-TB was successful for only 48 % of the cases. The WHO estimates that 9.6 % of MDR-TB cases exhibit XDR-TB.

Another challenge to account for the difficulty to eradicate completely is the co-infection with HIV. Among the 8.6 millions persons who developed TB in 2012, the WHO estimates that 13 % were HIV-positive²⁶. Additionally, patients infected with HIV accounted for 25 % of the deaths. Patients co-infected with HIV and TB possess a higher risk of developing active TB due to their weakened immune systems^{26, 36}. Most of the anti-retroviral drugs used in the treatment of HIV are not compatible with certain TB treatments³⁷⁻³⁹.

Taken together, these facts emphasize the necessity to discover new drug targets and identify new antitubercular compounds.

1.2 Characterization of *M. tb*

1.2.1 *M. tb* organism

Dr. Robert Koch discovered *M. tb*, the rod-shape bacterium responsible for most of the TB cases, in 1882⁴⁰. It is a gram-positive and acid-fast bacilli that is very slow-growing, with a division rate of 12 to 24 hours⁴¹. *Mycobacterium* belongs to the order of *Actinobacteria* that also includes *Corynebacterium* and *Streptomyces* for instance⁴².

M. tb is part of the *Mycobacterium tuberculosis* complex that includes diverse mycobacteria such as *M. tb*, *M. bovis*, *Mycobacterium africanum*, *Mycobacterium caprae*, *Mycobacterium canettii*, *Mycobacterium microti* and *Mycobacterium pinnipedii*¹. *M. tb* only infects human and shares 99.95 % identity with *M. bovis*, which causes TB in cows, but rarely in humans⁴³. *M. tb* is derived from the strain *M. canetti*⁴⁴. The organism is characterized by its cell wall that confers many unique properties⁴⁵. For instance, the cell envelope forms a hydrophobic barrier that prevents the entry of many antibiotics. Additionally, the different cell wall components participate in the recognition of *M. tb* by the macrophages^{27, 46, 47}.

1.2.2 Description of the mycobacterial cell wall (text reproduced from Favrot *et al.*, *Expert Rev. Anti Infect. Ther.*, 2012²³)

The mycobacterial cell envelope contains three covalently linked macromolecules (peptidoglycan, arabinogalactan, and mycolic acid) referred to as mycolyl-arabinogalactan-peptidoglycan complex (mAGP), as well as free glycolipids that are not covalently attached to the mycobacterial cell wall but associate with or are a part of the

mycobacterial outer membrane (MOM)⁴⁸⁻⁵¹. The peptidoglycan abbreviated as PG is formed with repeating N-acetyl- β -D-glucosaminyl-(1 \rightarrow 4)-N-glycolylmuramic acid. The PG is cross-linked via an L-alanyl-D-isoglutaminyl-*meso*-diaminopymelyl-D-alanine tetrapeptide attached to the muranic acid residues. The arabinogalactan (AG) consists of covalently coupled homogalactan and homoarabinan polymers⁵². In the homogalactan, β -D-galactofuranose units are linked alternatively through C-5 or C-6. The reducing residue of the galactan is linked to the PG through a phosphoryl-N-acetylglucosaminosyl-rhamnosyl linkage. The branched arabinan chains containing α -D-arabinofuranosyl (Araf) are attached through the reducing end to C-5 of the β -D-galactofuranose units. The arabinan domain is arranged with different α (1 \rightarrow 5), α (1 \rightarrow 3) and β (1 \rightarrow 2) Araf linkages. A branched hexaarabinofuranosyl structure is located at the non-reducing terminus of the arabinan polymer: two-thirds of the Araf hexasaccharide residues are esterified to mycolic acid, which are α -alkyl, β -hydroxy fatty acids that consist of a saturated, 20-26 carbon α -branch and a meromycolic acid moiety (chain up to 60 carbon atoms) that contain different functional groups such as ethoxy, methoxy, keto groups (methoxymycolates or ketomycolates) or cyclopropane rings (α -mycolates)⁵⁰. The α -mycolates are the most abundant type found in *M.tb*. The mycolates esterified to the arabinan form the inner leaflet of the MOM.

Free glycolipids are important components of the mycobacterial cell wall. Among them can be found trehalose dimycolate (TDM, often referred as cord factor), trehalose monomycolate (TMM), phosphatidylinositol mannosides, sulfolipids, phenolic glycolipids and phthiocerol dimycocerosate⁵³. These lipids interact with the mycolyl moiety of the mAGP skeleton forming a bilayer that functions as a formidable

permeation barrier. Another major glycolipid is the lipoarabinomannan (LAM). LAM is a polysaccharide chain containing Ara_f and mannopyranosyl residues that spans the MOM and the AGP terminating in a phosphatidylinositol-diacylglycerol moiety that is embedded in the cytoplasmic membrane. At the non-reducing end of LAM is a hexasaccharide moiety that, contrary to the AG, lacks any mycolic acid elaboration. ManLAM or mannose-capped lipoarabinomannam is a variant of LAM that appears to be involved in the host immune response⁵⁴. The merging of the MOM and the mAGP creates an extremely efficient permeability layer embedded with a growing list of possible porin proteins and other predicted outer membrane proteins⁵⁵. A schematic representation of the mycobacterial cell wall is given in figure 1-1.

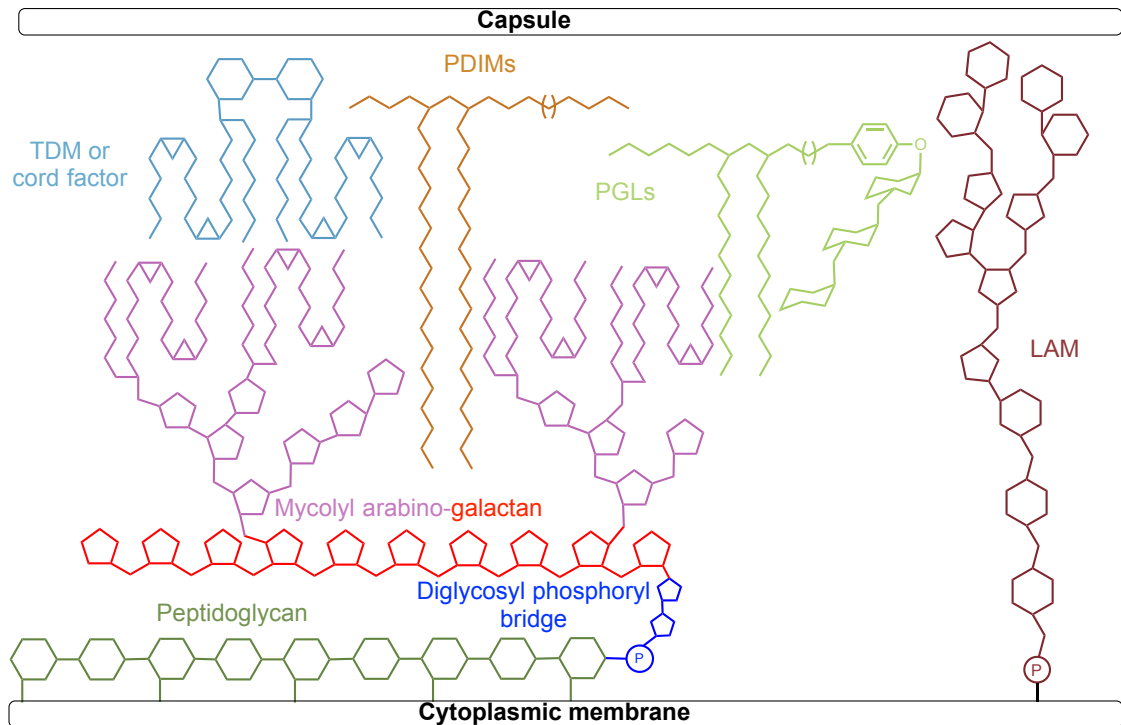


Figure 1-1: Scheme of the mycobacterial cell wall. Adapted from Favrot *et al.*, *Expert Rev. Anti Infect. Ther.*, 2012²³. LAM: lipoarabinomannan; P: phosphate; PDIMs: phthiocerol dimycocerosates; PGLs: phenolic glycolipids; TDM: trehalose dimycolate.

1.2.3 Significance of the mycobacterial cell envelope as a drug target (part of this text reproduced from Favrot *et al.*, *Expert Rev. Anti Infect. Ther.*, 2012²³)

The low permeability of the cell wall appears to be essential for the mycobacterial survival in the host. Since the hydrophobic nature of the outer cell membrane forms an impermeable barrier that prevents the entry of potential antibiotics into the bacterial cell, penetrating the mycobacterial cell wall with anti-TB drugs is a major challenge in TB treatment⁵⁶. Therefore, enzymes involved in the biosynthesis of these different mycobacterial cell wall components, as well as the enzymes necessary for the attachment of those components, are potentially excellent drug targets. Several current anti-tubercular drugs-including INH, EMB and ETH-inhibit enzymes involved the cell wall biosynthesis (Table 1-1) but with the appearance of *M. tb* strains resistant to these antitubercular drugs, it is necessary to find new ones.

Numerous research articles published over the past two decades describe efforts to identify new drugs and define their mechanism of action, as well as to discover compounds capable of inhibiting them^{23, 57, 58}. Several compounds targeting enzymes involved in the biosynthesis of cell wall components or proteins that transport those components are currently in clinical trials (SQ109, OPC-67683, PA-824, BTZ043)⁵⁹⁻⁶².

1.3 Overview and significance of the different projects

1.3.1 Antigen 85 complex

The Antigen 85 complex includes three proteins that function as mycolyltransferases. They are important enzymes that contribute to the biosynthesis of cell wall components. More specifically they attach the mycolic acids to either the AG or to TMM. A fluorescent-based assay developed in our laboratory lead to the identification of an inhibitor of the complex, ebselen. Chapter 2 describes the efforts in understanding the mechanism of action of ebselen on the Antigen 85 complex. Based on mass spectrometry and X-ray crystallography experiments, ebselen appears to be a covalent inhibitor that modifies a conserved cysteine in the complex and triggers a conformational change in the structure of the enzymes, leading to inactivation of the complex. Chapter 3 illustrates how covalent modification or mutation of this cysteine residue triggers the enzyme to adopt an inactive conformation.

1.3.2 Citrate Synthase

Citrate synthase is an enzyme that plays a role in the first step of the citric acid cycle and is found in nearly all living cells. The enzyme converts acetyl-CoA and oxaloacetate to citrate and coenzyme A. Little is known about the *M. tb* citrate synthase except that based on bioinformatics analysis, the enzyme would be a citrate synthase type II. A type II enzyme exhibits an extra N-terminal β -sheet domain and in some cases, the enzyme may be allosterically inhibited by nicotinamide adenine dinucleotide. Chapter 4

describes the efforts to gain more insights about *M. tb* citrate synthase by solving the crystal structure of the enzyme and developing an absorbance-based assay.

1.3.3 Enhanced intracellular survival protein

The enhanced intracellular survival protein is known to play a role in modulating the immune response and autophagocytosis in macrophages following infection by *M. tb*. Based on bioinformatic analysis, the enzyme appears to be an acetyltransferase that catalyses the transfer of an acetyl moiety from acetyl-CoA to another unknown substrate. However, no studies to date have succeeded in unambiguously identifying its molecular function in pathogenesis. Chapter 5 describes the efforts to solve the crystal structure of the enhanced intracellular survival protein and to identify its co-substrate(s) using profiling experiments and mass spectrometry.

Chapter 2

Characterization of the inhibitory mechanism of Ag85 complex by ebselen

2.1 Background

2.1.1 Antigen 85 complex function

The *M. tb* antigen 85 complex is composed of three proteins, Ag85A, Ag85B and Ag85C, encoded by the *fbpA*, *fbpB* and *fbpC* genes, respectively. All three enzymes share between 68 and 80 % sequence similarity. Each protein contains a N-terminal signal sequence that allows them to be secreted. Ag85B is the major secreted protein present in *M. tb*⁶³.

Using a radiometric assay, Belisle and coworkers demonstrated that the three proteins are mycolyltransferases: the antigen 85 enzymes catalyze a transesterification reaction to produce trehalose dimycolate (TDM) from trehalose monomycolate (TMM)⁶⁴. Additionally, research by Jackson *et al.* established that the inactivation of *fbpC* results in a 40 % decrease of the cell wall-bound mycolic acids, suggesting that Ag85C is involved in the esterification of the AG complex⁶⁵. However, Ag85C does not appear to be specific to a particular type of mycolic acid. The activity of Ag85C was also confirmed with the use of synthetic substrates⁶⁶. Another study indicated that knockout of *fbpA* leads to a 45

% reduction of TDM production but does not affect the cell wall-bound mycolic acids⁶⁷. More recently, research by Matsunaga and coworkers suggests that Ag85A participates in the glucose monomycolate biosynthesis in *Mycobacterium avium*⁶⁸. The role of Ag85B in the cell wall biosynthesis remains unclear⁶⁹. Figure 2-1 summarizes the role of each Ag85 enzyme.

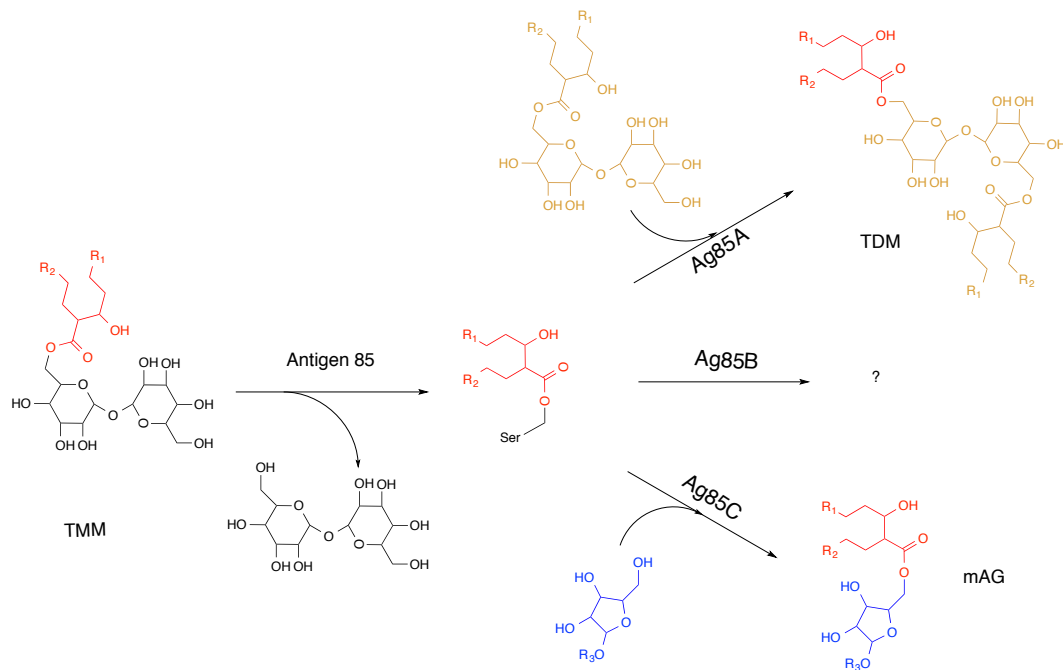


Figure 2-1: Roles of the different Ag85 enzymes. Ag85A appears to be involved in the TDM production while Ag85C participates in the transfer of mycolic acids to the AG complex. The role of Ag85B remains unclear. Adapted from Favrot *et al.*, *Expert Rev. Anti Infect. Ther.*, 2012²³.

The structures of all three Ag85 proteins have been solved⁷⁰⁻⁷². The three enzymes display an α/β -hydrolase fold and a conserved catalytic triad. The crystal structure of Ag85C revealed that the transfer of mycolic acids is carried out through a ping-pong

mechanism⁷⁰. S124 serves as a nucleophile that attacks the carboxyl carbon of TMM leading to the formation of an acyl-enzyme intermediate, whereas H260 and hypothetically E228 assist the nucleophilic attack by playing the role of general bases. Then a second molecule of TMM binds in the carbohydrate-binding pocket of Ag85C and attacks the acyl-enzyme intermediate, resulting in a tetrahedral transition state. The protonation of S124 triggers the release of TDM (Figure 2-2). Site-directed mutagenesis of S124 confirmed the role of the residue, as a S124A mutant disrupts the production of TDM or any other acylated product⁶⁴.

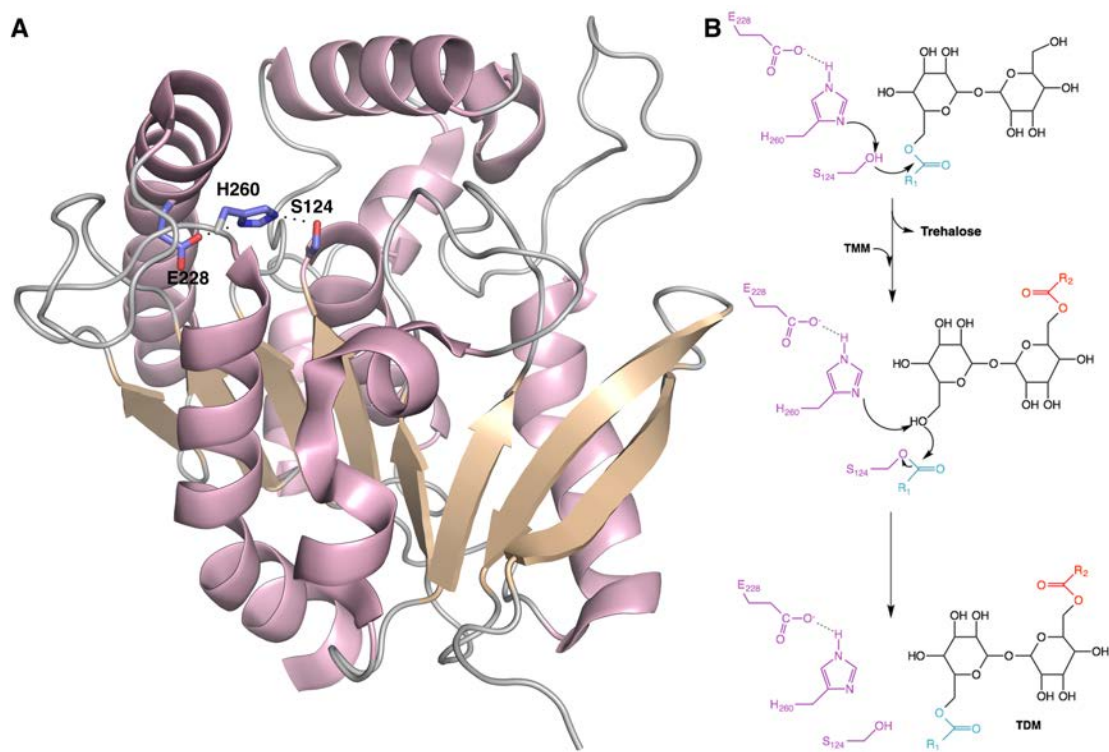


Figure 2-2: Ag85C structure and mechanism. A) Cartoon representing Ag85C structure (PDB 1DQZ). The catalytic triad residues (S124, E228 and H260) are represented with sticks. The hydrogen-bonded network is displayed between the three residues involved in the Ag85C mechanism. B) Scheme representing the catalytic mechanism of Ag85 enzymes.

2.1.2 Antigen 85 complex as a validated drug target

All three enzymes exhibit a similar active site structure and share the same mycolic acid donor⁷⁰⁻⁷². Hence, a single molecule should inhibit all three Ag85 enzymes. Furthermore, the *fbp* genes appear to be synthetically lethal; no viable double knockout has been observed previously. Consequently, the risk of developing drug resistance is minimized since the probability to have mutations arising coincidentally in two different *fbp* genes to promote resistance to a single drug is very low.

Additionally, the secreted Ag85 enzymes are located in the periplasmic space and thus are more accessible to drugs; therefore, the probability of rejection of a drug from the cell by efflux pumps or chemical modifications when the drug passes through the membrane is minimized⁷³.

Research by Jackson and co-workers showed that a *M. tb* strain containing a deletion mutant of *fbpC* is more permeable to hydrophobic and small hydrophilic molecules such as glycerol⁶⁵. More recently, Nguyen *et al.* demonstrated that knockout of *fbpA* increased the sensitivity of *M. tb* to both broad-spectrum antibiotics and diverse antitubercular drugs, in particular erythromycin, imipenem, rifampin or vancomycin⁶⁷. Moreover, the decrease in mycolyltransferase expression promotes the bacterial sensitivity to INH⁷⁴.

Taken together, these data validate the Ag85 complex as drug target. Targeting the Ag85 enzymes increases the permeability of the cell wall and facilitates the entrance of other antibiotics inside the cell. Thus, a drug targeting these enzymes could be used in a combination regimen to improve the efficacy of other drugs.

2.1.3 Research aims

As a validated drug target, the search for Ag85 inhibitors has been pursued over the years. First, the assay developed by Belisle and coworkers was used to screen libraries of either substrate-based compounds⁷⁵⁻⁷⁸ or transition state analogs⁷⁹⁻⁸¹. However, this assay utilizes radioactive [¹⁴C]-trehalose and extracted TMM and is not reliable at a high-throughput level. In 2009, Boucau *et al.*, as well as Elamin *et al.*, developed high-throughput assays⁸²⁻⁸⁴. Nonetheless, these assays exhibit limitations due to problems with lipid solubility, assay precision or reproducibility. More recently, a label-free assay using electrospray ionization mass spectrometry was used to determine kinetic parameters, as well as to design and test a selective covalent inhibitor of the Ag85 complex⁸⁵. However, the process is not high-throughput and the identified compound displays some cytotoxicity. Finally, Warriar *et al.* identified I3-AG85, a new inhibitor of Ag85C among a library of 5000 synthetic fragments⁸⁶. The inhibitor exhibits activity against drug-resistant strains of *M. tb*. However, the determined MIC (200 μ M against *M. tb* H37Rv and diverse drug-resistant strains) is still high and further improvements are necessary.

Hence, the search for potent inhibitors of the Ag85 complex is still ongoing. Our laboratory developed a more robust, reproducible and high-throughput assay in order to identify new inhibitors of the Ag85 complex^{87, 88}. This fluorescent-based assay utilizes resorufin butyrate as an acyl donor and trehalose as an acyl acceptor (Figure 2-3). Once Ag85C transfers the butyrate chain to trehalose, resorufin, a fluorescent compound ($\lambda_{exc} = 500$ nm; $\lambda_{em} = 590$ nm), is released; by monitoring the fluorescence, the activity of Ag85C can be measured. The assay provided a Z' value of 0.82, validating the assay for

high-throughput screening⁸⁹. The screening of the NIH Clinical Collection performed by Dr. Daniel Lajiness led to the identification of a selenazole compound, ebselen, as a potent inhibitor of the Ag85 complex⁸⁷. Dose dependence revealed a K_i of 63 nM. However, the mechanism of Ag85 inhibition was initially unclear.

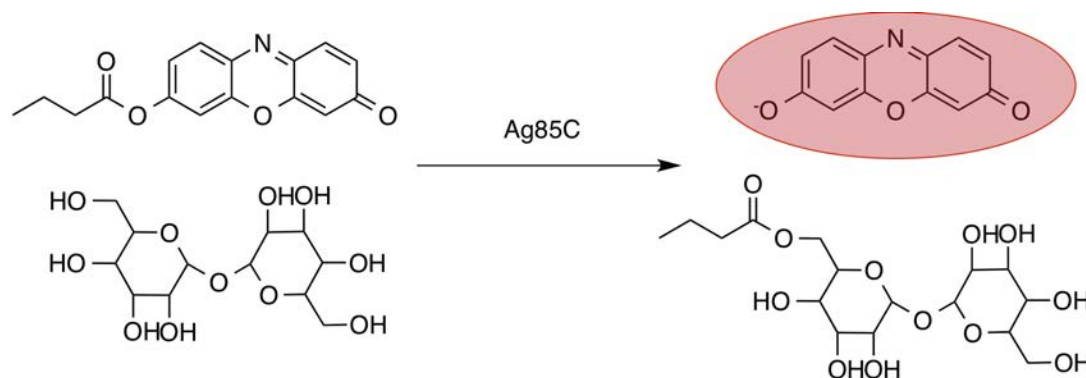


Figure 2-3: Ag85C fluorescent-based assay. In presence of Ag85C, the butyrate chain is transferred from resorufin butyrate to trehalose, leading to the release of resorufin, a fluorescent molecule ($\lambda_{exc} = 500$ nm; $\lambda_{em} = 590$ nm).

The aim of this research was to characterize the mechanism of inhibition of the Ag85 complex by ebselen. To this purpose, mass spectrometry, X-ray crystallography, site-directed mutagenesis and enzymatic assays were utilized.

2.2 Experimental procedures

2.2.1 Molecular cloning

The molecular cloning of the *M. tb fbpA/B and C* genes encoding respectively the secreted portion of Ag85A/B and C was carried out by Dr. Julie Boucau^{83, 90}. Briefly, the genes *fbpA* and *B* were inserted between *NdeI* and *BamHI* restriction sites in a pET28 plasmid (EMD biosciences), allowing a cleavable N-terminal poly-histidine tag. The segment of *fbpC* was ligated into a pET29 plasmid (EMD biosciences) between the *NdeI* and *XhoI* restriction sites. The construct contains a non-cleavable C-terminal poly-histidine tag.

Mutants of Ag85C (C209G, C209S, C209F, and C209A) were obtained using site-directed mutagenesis. Site directed mutagenesis was carried out using the construct pET29-*fbpC* as a template, as well as the primers and their respective complements described in Table 2-1 (Integrated DNA Technology). The mutations were confirmed by DNA sequencing (Eurofins MWG Operon).

Table 2-1: Primers used for site-directed mutagenesis on pET29-*fbpC*. *The C209S mutant was obtained by Dr. Julie boucau.

C209G	GGATCTGGGTGTAC GG CGGTAACGGCACA
C209S*	CGGATCTGGGTGTAC AG CGGTAACGGCACACCC
C209F	CCGGATCTGGGTGTACT TC GGTAACGGCAC
C209A	CGGATCTGGGTGTAC GCC GGTAACGGCACACC

2.2.2 Protein purification of Ag85s and mutants

The different plasmids were used to transform T7 express *E. coli* cells (New England BioLabs). Bacterial cells were cultured at 37 °C in Luria Broth (Research Products International) to an OD_{600nm} of 0.6. Isopropyl β-D-1-thiogalactopyranoside (1 mM, IPTG) was added to induce protein expression and the incubation temperature was decreased to 16 °C. The bacterial cells were harvested after 36 hours induction using centrifugation. The pelleted cells were resuspended into 20 mM Tris pH 8.0, 25 mM imidazole and 5 mM β-mercaptoethanol (β-Me). Then, cell lysis was performed by addition of lysozyme (Hampton Research) and DNase I (Roche), and a sonication step was also included (Sonicator 3000, Misonix). Nickel affinity and anion exchange chromatography were carried out (Figure 2-4). In some cases, size exclusion chromatography was used as a polishing step.

The protein was concentrated using an ammonium sulfate precipitation step (2.6 M and 2.8 M for Ag85C and Ag85A/B respectively). The pelleted protein was resuspended into either crystallization buffer (10 mM Tris pH 7.5, 2 mM EDTA and 1 mM dithiothreitol (DTT)) or assay buffer (50 mM sodium phosphate pH 7.5, 1 mM DTT). The sample was dialyzed overnight against the respective buffers.

Absorbance spectroscopy at a wavelength of 280 nm was used to determine the enzyme concentration. The theoretical extinction coefficients of the different proteins were calculated with the ProtParam function from the ExPASy proteomics server⁹¹.

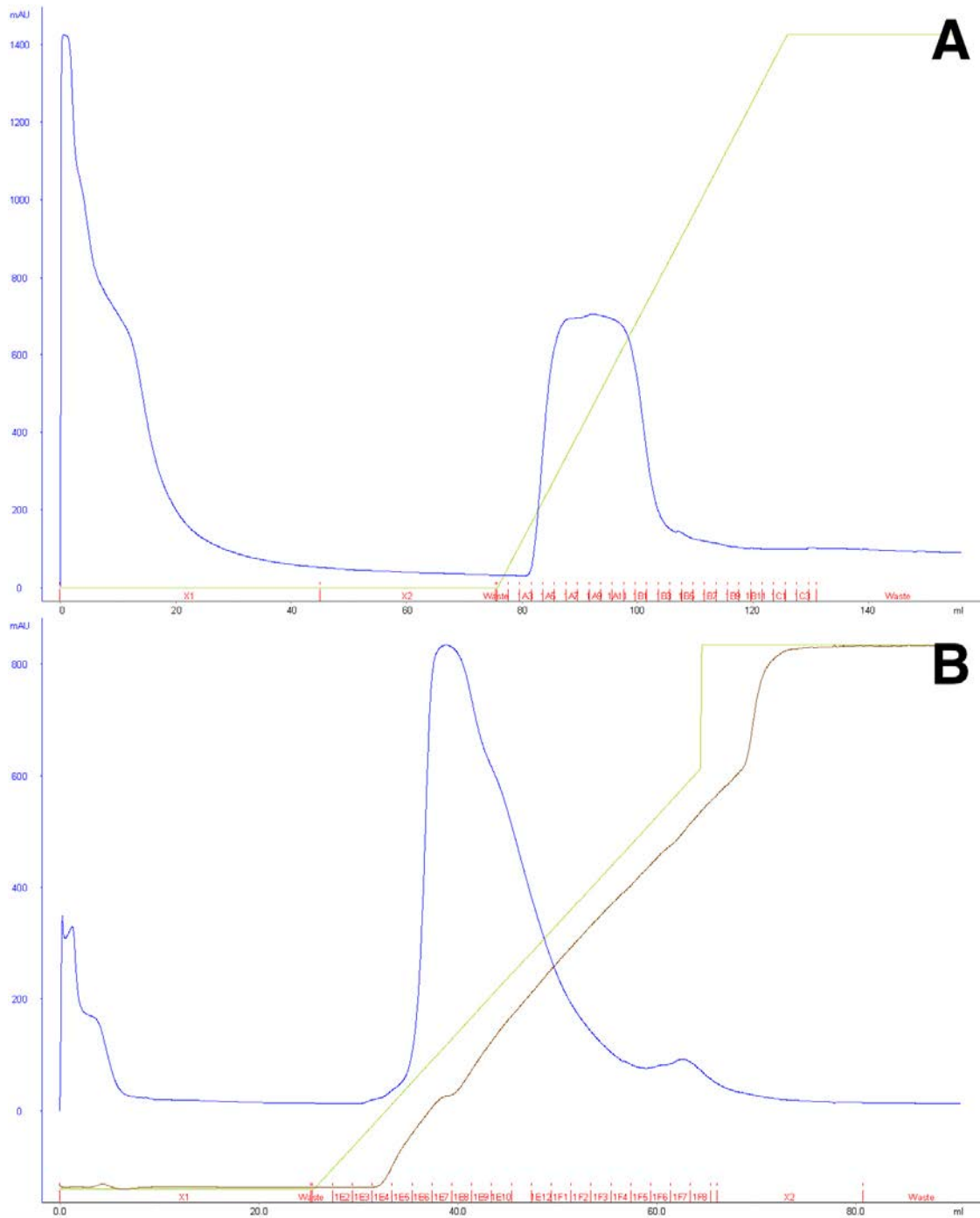


Figure 2-4: Purification of Ag85C. A) Chromatogram from nickel affinity purification of Ag85C. B) Chromatogram from anion exchange purification of Ag85C. The blue line corresponds to the absorbance monitored at 280 nm while the green line represents the concentration of buffer B (higher concentration in imidazole). The brown line corresponds to the conductivity measured.

2.2.3 Ag85C fluorescence-based assay

The activity of Ag85C and its different mutants was tested using a fluorescence-based assay⁸⁸. Resorufin butyrate, a fluorescent compound (Santa Cruz Biotechnology), was used as an acyl donor whereas trehalose was used as an acyl acceptor. All reactions were performed in 50 mM sodium phosphate pH 7.5. Trehalose was dissolved in the reaction buffer while a 10 mM stock solution of resorufin butyrate was prepared using DMSO. The reactions were performed in triplicate at 37 °C on a Synergy H4 Hybrid Reader (BioTek) using 500 nM Ag85C or the tested mutants, 4 mM trehalose and 100 µM resorufin butyrate. Resorufin butyrate was added last to initiate the reaction. Analysis of the data was carried out using Prism 5 software.

Iodoacetamide (AK Scientific Inc), abbreviated as IAA, was used as an alkylating agent. The alkylation reactions were performed using concentrations from 2.6 mM to 51.2 mM. The activity of the alkylated enzyme was tested after 1 hour and 24 hours incubation, using the assay described above. A control reaction with a non-alkylated enzyme was run in parallel.

A time course experiment was performed using 5 µM ebselen (Cayman Chemical Company) and similar conditions to the ones described earlier. Additionally, a library of ebsulfur derivatives was tested using similar conditions as described. The compounds were incubated for 15 minutes with Ag85C prior to starting the reaction with the addition of resorufin butyrate. The dose-dependence experiments were carried out in triplicate reactions.

2.2.4 Mass spectrometry

The different samples (Ag85A, Ag85B, Ag85C and Ag85C-C209S) were buffer exchanged against 10 mM ammonium acetate pH 7.0 to a concentration of 0.5 mg/mL using a 3 kDa ultrafiltration device (Millipore). The protein samples were incubated with 200 μ M ebselen (10 mM stock solution of ebselen prepared in DMSO) for 2 hours on ice. After one hour, half of the sample containing Ag85C and ebselen was treated with 1 mM DTT and incubated for an hour. A control reaction was also performed in which DMSO (final concentration of 2%) was added to Ag85C. In order to remove the excess ebselen, the samples were again buffer exchanged three times with the same buffer previously mentioned. Finally the protein complexes were diluted using a solution containing acetonitrile/water (1:1, v/v) and 0.1 % formic acid to a concentration of 0.1 mg/mL. Each reaction was analyzed on an ESI Q-TOF Micro mass spectrometer (Waters) in positive ion mode. MassLynx software (Waters) was used to acquire and analyze the ESI-MS data.

For peptide fingerprinting experiments, in-solution trypsin digestion was carried out using sequencing-grade trypsin (Promega) following standard procedures provided by Promega guidelines. Peptide mass fingerprinting was carried on a MALDI-TOF/TOF mass spectrometer (Bruker Daltonics). α -Cyano-4-hydroxycinnamic acid (CHCA, Acros Organics) was dissolved in acetonitrile/water (1:1, v/v) and 0.1 % formic acid and used as a matrix. The data were analyzed using MASCOT server.

An alkylation reaction using 38 mM IAA was performed. In-solution trypsin digestion was performed with sequencing-grade trypsin and analysis of the tryptic peptides were analyzed as previously described.

2.2.5 Crystallization

The crystals were grown using the hanging-drop vapor diffusion technique. The protein samples dialyzed against the crystallization buffer described in section 2.2.2 were concentrated to 5 mg/mL. The initial crystallization experiments use the index screen purchased from Hampton Research. Ag85C was incubated with 200 μ M ebselen (10 mM stock dissolved in DMSO) for 2 hours on ice. The crystal of Ag85C co-crystallized in the presence of ebselen was grown in 25 % w/v PEG 1500 while Ag85C-C209S was crystallized against a well solution of 0.1 M bis-tris pH 6.5 and 25 % w/v PEG 3350. Both crystals formed after one month.

Crystals were flash-cooled in liquid nitrogen before data collection. Diffraction data were collected at the LS-CAT beamline at the Advance Photon Source Argonne National Laboratory (APS-ANL, IL).

2.2.6 Structure determination

X-ray data were indexed, integrated and scaled using HKL2000⁹². Molecular replacement was carried out using Evolutionary Program for Molecular Replacement (EPMR)^{93, 94}. The structure of native Ag85C (PDB 1DQZ) was used as a model⁷⁰. The refine tool in PHENIX was used to perform rigid body refinement, simulated annealing, positional and B-factor refinements⁹⁵. Finally, the models were manually corrected using COOT⁹⁶.

2.3 Results and Discussion

Most of the figures from this section are reproduced from Favrot *et al.*, *Nat. Commun.*, 2013⁸⁸.

2.3.1 Ebselen as a potent Ag85C inhibitor *in vitro* and *in vivo*

Ebselen was identified as a potent inhibitor of the Ag85 complex based on the fluorescent-based assay ($K_i = 63$ nM). Lu *et al.* demonstrated the antimycobacterial activity of ebselen against *M. tb* drug-sensitive and drug-resistant strains⁹⁷.

A Kirby-Bauer disk diffusion assay was carried out. This assay allows us to ascertain whether or not bacteria are susceptible to a particular antibiotic. *Mycobacterium smegmatis* (*M. smegmatis*), a non-pathogenic bacterium used as a model for *M. tb*, was spread onto an agar plate containing carbenicillin antibiotic (0.1 mg/mL). Then, paper disks impregnated with varying amounts of ebselen are placed on the surface of the agar. One of the disks contains only DMSO and serves as a control. If *M. smegmatis* is susceptible to the compound, growth inhibition should be observed around the disk.

Growth inhibition in presence of ebselen was observed and exhibited dose-dependence (Figure 2-5-A). Ebselen was also tested on *E. coli* but the growth was not inhibited (Figure 2-5-B). Thus, ebselen appears to specifically inhibit the growth of mycobacteria.

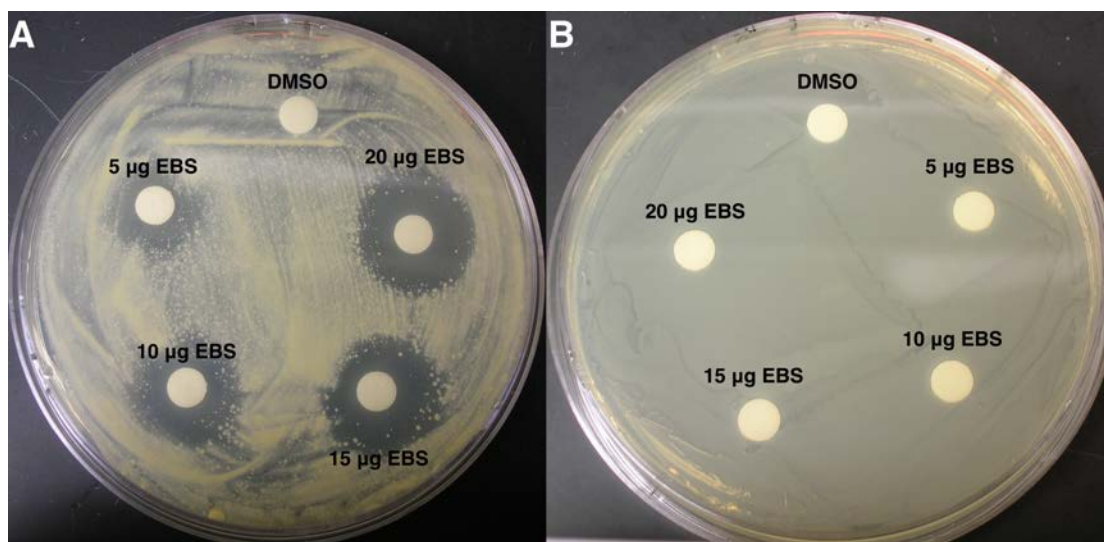


Figure 2-5: Kirby-Bauer diffusion disk assay. A) The zone of *M. smegmatis* growth inhibition is larger as the amount of ebselen (EBS) increases. B) Ebselen does not inhibit the growth of *E. coli*.

With the collaboration of Dr. Anna Grzegorzewicz from Dr. Mary Jackson's laboratory, the selenazole compound was tested using an orthogonal assay for all three enzymes. Dr. Grzegorzewicz performed the same radiometric mycolyltransferase assay developed by Belisle *et al.*^{64, 88}. The mycolyltransferase activity of Ag85C was measured in presence of [U-¹⁴C]-trehalose, TMM and either 0 or 10 µM ebselen; the radiolabeled substrates and products were visualized on TLC plates and the amounts of each were determined by autoradiography. The reaction containing ebselen displays clear inhibition of TDM production. Similar results were obtained with Ag85A and Ag85B, confirming the inhibition of the Ag85 complex by ebselen. Then, a resazurin-based growth assay was carried out; the determined minimum inhibitory concentration (MIC) of ebselen against

M. tb mc²6206 was found to be 20 µg/mL, a result similar to the MIC published by Lu *et al.* against both *M. tb* drug-resistance and drug-sensitive strains⁹⁷.

Based on the determined MIC, Dr. Grzegorzewicz monitored the effect of ebselen treatment on [¹⁴C]-acetate incorporation into TMM, TDM and cell wall-bound mycolic acids (MAMEs, mycolates esterifying the AG complex). Ebselen clearly inhibits the production of TDM (60 % decrease) and cell wall-bound mycolic acids (50 % reduction), but does not seem to affect TMM biosynthesis. This result suggests that the Ag85 complex is the target of ebselen *in vivo* as TDM and mAG production is inhibited in by the application ebselen. Data are presented in Favrot *et al.*, *Nat. Commun.*, 2013⁸⁸.

2.3.2 Ebselen binds covalently to C209 of Ag85C

The identification of ebselen as an inhibitor of Ag85C was intriguing. Indeed, the chemical structure of ebselen does not resemble any of the substrates, products or transition states of the Ag85 complex. Ebselen is known to present glutathione peroxidase-like activity⁹⁸⁻¹⁰² and can inhibit diverse enzymes such as NO synthases¹⁰³, dimethylarginine dimethylaminohydrolase¹⁰⁴, diguanylate cyclase¹⁰⁵, inositol monophosphatase¹⁰⁶, heme enzyme indoleamine 2,3-dioxygenase¹⁰⁷, etc. Ebselen was tested through phase 1-3 clinical trials to treat strokes^{108, 109}. Ebselen has also been shown to trigger DNA damage responses¹¹⁰ and reactive oxygen species (ROS) cytotoxicity¹¹¹.

Recently, Xu *et al.* demonstrated the ability of ebselen to form a stable and specific selenenylsulfide bond with thiols¹¹². Ag85C possesses one cysteine (C209) positioned on β-strand β7 near the active site. However, the cysteine does not participate

in catalysis. We hypothesized that the inhibitor effect of ebselen on Ag85C is a result of covalent modification of C209 (Figure 2-6).

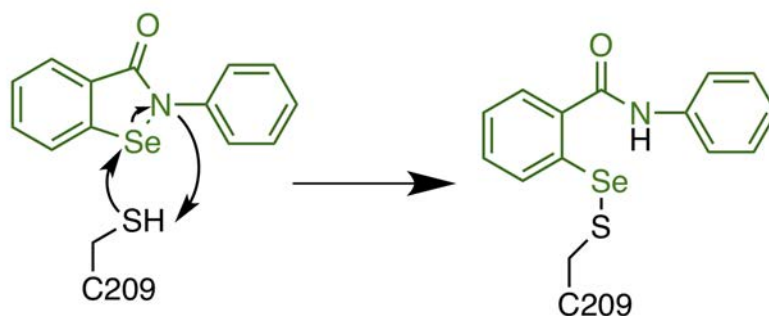


Figure 2-6: Hypothetic mechanism of Ag85C inhibition by ebselen

To ascertain whether or not ebselen reacts and forms a covalent bond with Ag85C, the enzyme was incubated with ebselen for two hours and the sample was subjected to electrospray ionization mass spectrometry (ESI-MS) under denaturing conditions. Any unreacted ebselen was removed by buffer exchange using ultrafiltration prior to performing the MS experiment. A control reaction in which only DMSO was added to a sample of Ag85C was also carried out. The deconvoluted mass spectra between the control reaction and the sample display a mass difference of 274.0 Da (Figure 2-7), which corresponds to one ebselen molecule (average molecular mass of 274.18). The shift in mass highlights the formation of a covalent complex between ebselen and the enzyme.

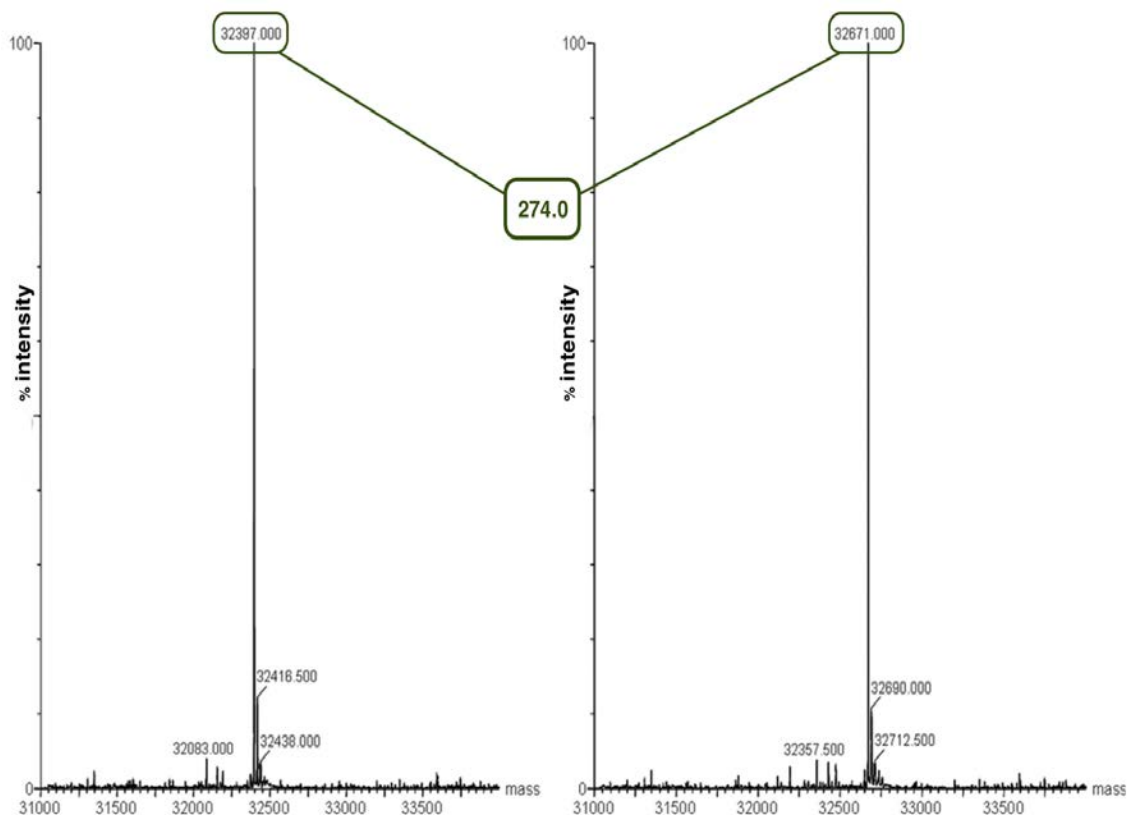


Figure 2-7: Modification of Ag85C by ebselen. Deconvoluted mass spectra of Ag85C with (right) or without (left) display a shift of 274.0 Da, corresponding to one ebselen molecule.

Contrary to Ag85C, Ag85A and Ag85B each contain three cysteine residues. One cysteine is conserved in all three enzymes and is located at position 209 in Ag85C or 211 in Ag85A and B while the two additional cysteine residues found in Ag85A and B form an intramolecular disulfide bond. Samples of Ag85A and B incubated with ebselen were also subjected to ESI-MS and compared to control reactions without ebselen. The experiment shows that both enzymes were covalently modified at a single site (Figure 2-8). These data suggest that ebselen modifies all three enzymes in a similar manner at position 209 or 211, and does not disrupt the disulfide bond found in Ag85A and B.

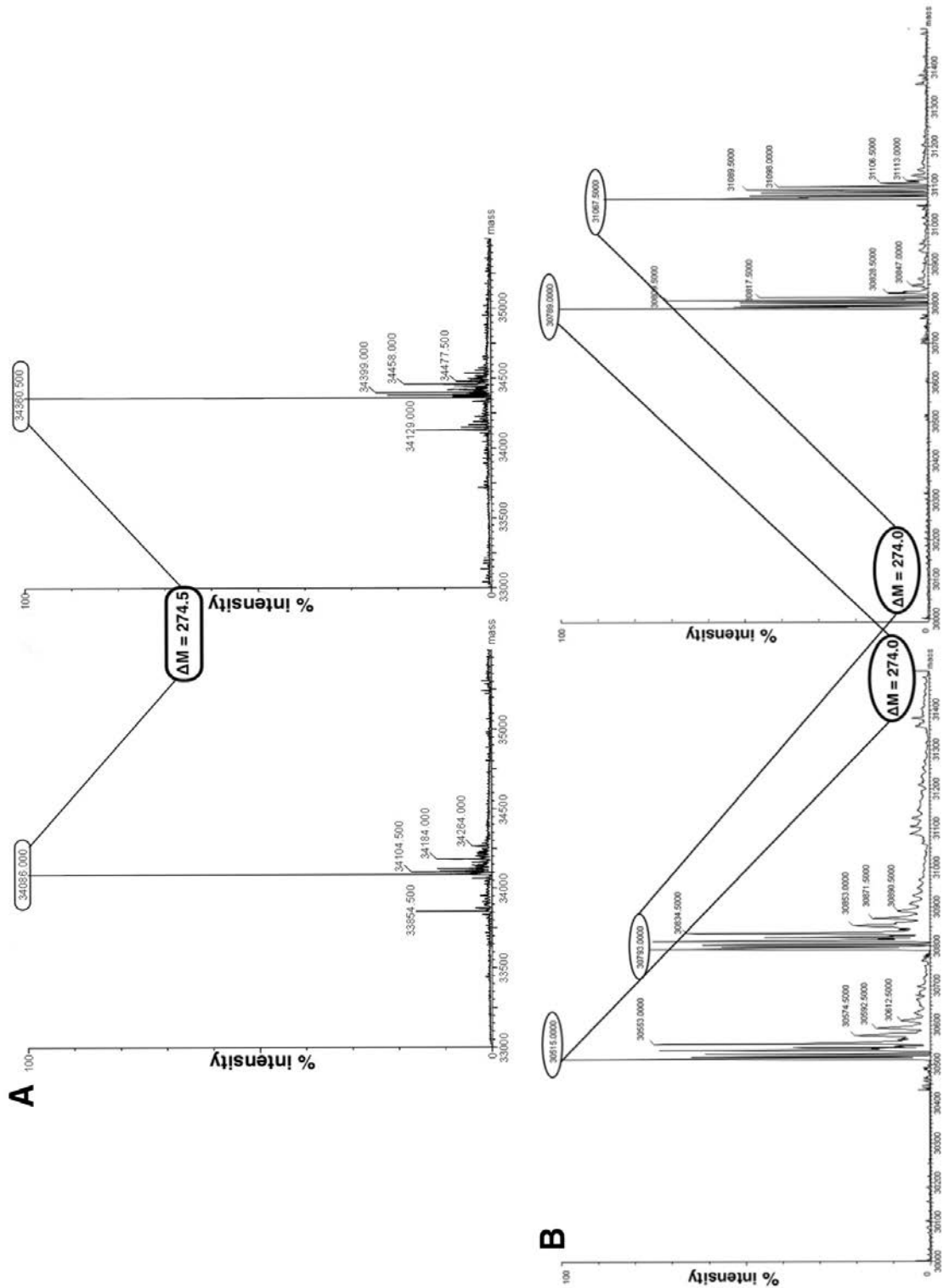


Figure 2-8: Modification of Ag85A and Ag85B by ebselen. A) Intact mass of Ag85A with (right) or without ebselen (left). B) Intact mass of Ag85B with (right) or without ebselen (left).

To further strengthen the hypothesis that ebselen modifies Ag85C at C209, two other experiments were carried out. First, the same experiment as previously described was performed with a cysteine to serine mutant at position 209. If ebselen reacts with a cysteine as hypothesized, it should not modify covalently this mutant in which the cysteine was replaced with a serine. The Ag85C-C209S mutant does not exhibit any change in its intact mass when incubated with ebselen (Figure 2-9), indicating that ebselen does not modify Ag85C-C209S. This experiment suggests that the covalent modification of Ag85C by ebselen occurs at C209. Additionally, peptide fingerprinting was carried out on a sample of Ag85C incubated with ebselen and another sample incubated with DMSO as a control. A shift in the mass corresponding to one ebselen molecule was observed in the peptides harboring the cysteine residue (Table 2-2).

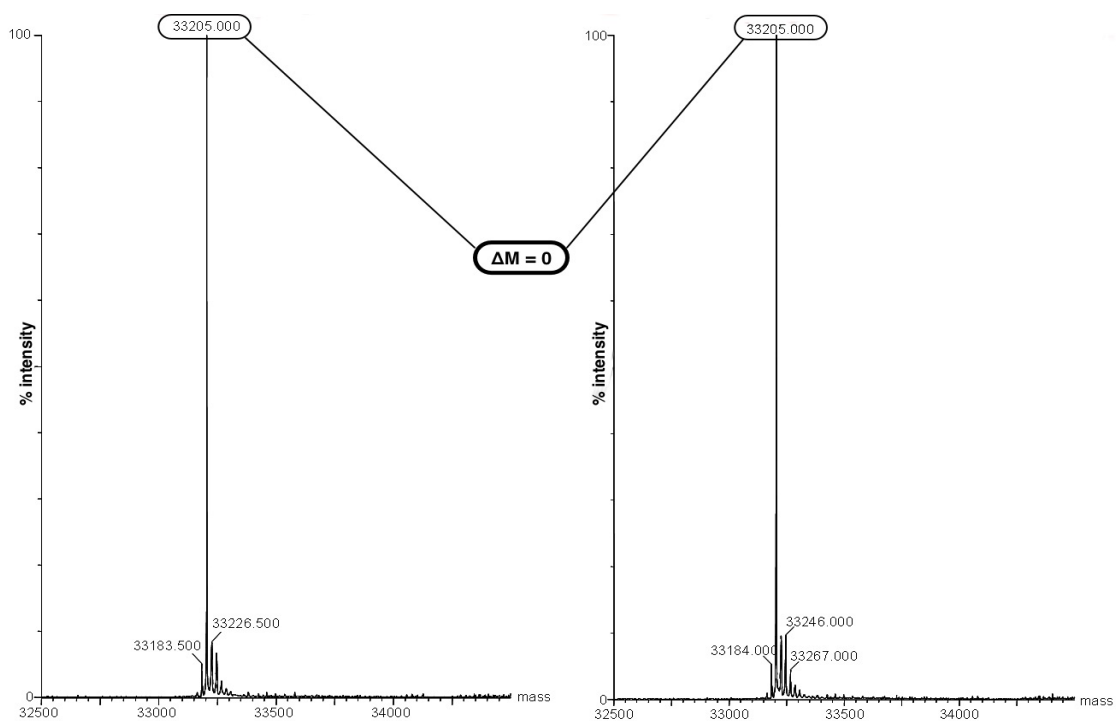


Figure 2-9: Deconvoluted mass spectra of Ag85C-C209S with (right) or without ebselen (left). No mass shift was observed between the two samples, confirming that C209 is the residue modified by ebselen.

Table 2-2: Peptide mass fingerprinting of Ag85C incubated with DMSO or ebselen. The m/z values provided correspond to monoisotopic singly-charged ions. A shift in mass (*) was observed for the sample covalently modified by ebselen (monoisotopic mass = 274.98). n/o: not observed.

Samples	Peptides harboring C209	m/z (calculated)	m/z (observed)	ΔM
Ag85C	(R)IWVY <u>C</u> GNNGTPSDLGGDNIPAK(F)	2177.0332	n/o	n/o
	(R)LVANNTRIWVY <u>C</u> GNNGTPSDLGGDNIPAK(F)	2945.4574	n/o	n/o
	(R)IWVY <u>C</u> GNNGTPSDLGGDNIPAKFLEGLTLR(T)	3106.5666	3106.5357	0.0309
Ag85C- ebselen	(R)IWVY <u>C</u> GNNGTPSDLGGDNIPAK(F)	2177.0332	2452.1400	275.1068*
	(R)LVANNTRIWVY <u>C</u> GNNGTPSDLGGDNIPAK(F)	2945.4574	3219.5860	274.1286*
	(R)IWVY <u>C</u> GNNGTPSDLGGDNIPAKFLEGLTLR(T)	3106.5666	3381.6710	275.1044*

The formed selenenylsulfide bond results from C209 oxidation by ebselen. For this reason, the covalent complex formation should be reversible when subjected to a reducing agent such as DTT. A sample of Ag85C modified by ebselen was reacted with 1 mM DTT. The sample was then subjected to ESI-MS under denaturing conditions. The deconvoluted mass spectrum displays two peaks: the lowest peak corresponds to the Ag85C-ebselen covalent complex while the most intense peak exhibits a decrease in mass corresponding to the loss of one ebselen molecule from the covalent complex (Figure 2-10). The reversibility of the reaction under reducing conditions suggests that the ebselen target is more likely to take place in an oxidizing environment, such as the extracellular environment or the periplasmic space, rather than in the reducing environment of the cytoplasm. This data supports again that the Ag85 complex is a likely target of ebselen *in vivo*.

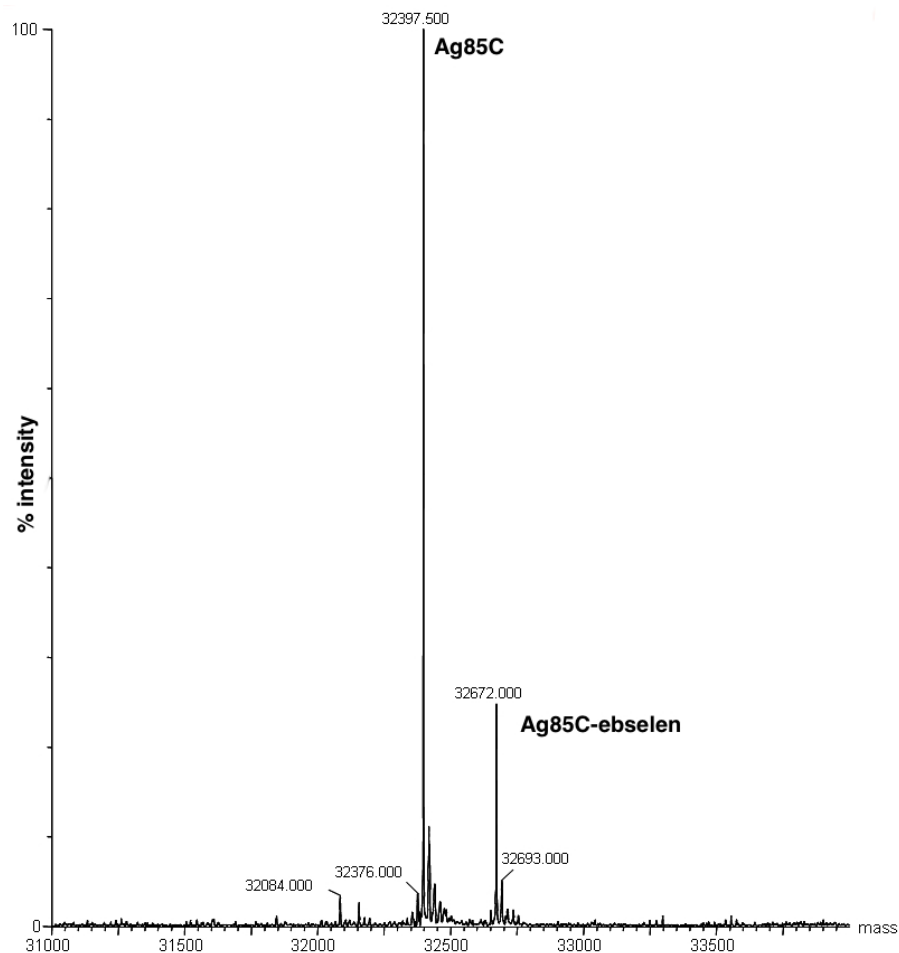


Figure 2-10: Deconvoluted mass spectrum of Ag85C-ebseen treated with DTT. The most intense peak corresponds to wild-type Ag85C, indicating the reduction of the covalent complex by DTT.

2.3.3 C209 modifications lead to a significant loss in Ag85C activity

To determine the effect of the covalent modification on Ag85C enzymatic activity, the samples of Ag85C incubated with either DMSO or ebselen for the purpose of ESI-MS were assayed using the fluorometric assay previously described. As a reminder, all excess ebselen was removed using buffer exchange and ultrafiltration, meaning that

only ebselen covalently attached to C209 is present in the sample. A control reaction lacking enzyme was also carried out. The reactions were performed in triplicate to ensure reproducibility, and activity was normalized to wild-type Ag85C. The covalent complex exhibited less than 10 % activity compared to the wild-type enzyme (Figure 2-11, bars 1 and 2).

To assess if the reduction of the selenenylsulfide bond and consequently the reversion of C209 covalent modification by ebselen can rescue enzymatic activity, a complex of Ag85C-ebselen lacking enzymatic activity was treated with DTT for 24 hours. The sample was then assayed using the previously mentioned fluorometric assay. Reducing selenenylsulfide bond leads to almost complete recovery of Ag85C enzymatic activity (Figure 2-11, bar 3), indicating that the attachment of ebselen to C209 is the reason of the inhibition of the enzyme activity.

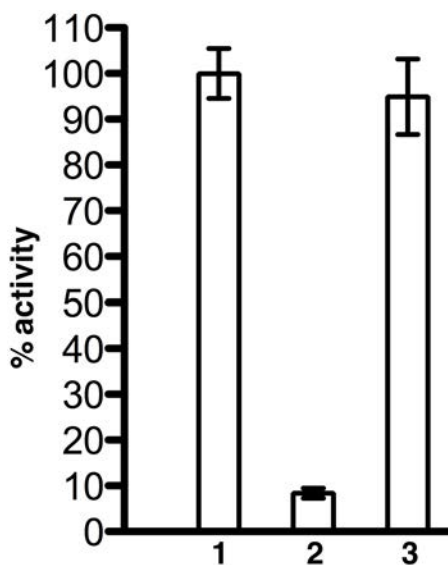


Figure 2-11: Reversibility of Ag85C inhibition by ebselen. Bars 1 and 2 correspond to Ag85C normalized activity without or with ebselen, respectively; bar 3 corresponds to the sample treated with DTT. Error bars were calculated from triplicate reactions.

To further understand if the inhibition of the enzymatic activity is specific to ebselen or if any modification at C209 results in enzyme inhibition, Ag85C was modified with IAA. IAA is an alkylating reagent that is commonly used to detect thiols in biomolecules (Figure 2-12-A). Peptide fingerprinting using in-solution trypsin digestion was performed to confirm the modification of C209 (Table 2-3). Tryptic peptides were analyzed with MALDI-TOF/TOF mass spectrophotometry.

Table 2-3: Peptide mass fingerprinting of Ag85C incubated with IAA. The *m/z* values provided correspond to monoisotopic singly-charged ions. A shift in mass (*) was observed for the sample covalently modified by IAA (monoisotopic mass = 57.02). n/o: not observed.

Samples	Peptides harboring C209	<i>m/z</i> (calculated)	<i>m/z</i> (observed)	ΔM
Ag85C- IAA	(R)IWVY <u>C</u> GNGTPSDLGGDNIPAK(F)	2177.0332	2235.1330	58.0998*
	(R)LVANNTRIWVY <u>C</u> GNGTPSDLGG DNIPAK(F)	2945.4574	n/o	n/o
	(R)IWVY <u>C</u> GNGTPSDLGGDNIPAKFL EGLTLR(T)	3106.5666	n/o	n/o

Ag85C was modified with different amounts of IAA (2.6-51.2 mM) and the different samples were assayed after 1 hour and 24 hours incubation using the resorufin butyrate assay. As the concentration of IAA increases, a dose dependent effect is observed on Ag85 enzymatic activity. At 51.2 mM of IAA, a 60 % decrease in enzyme activity was observed after 1 hour incubation whereas 24 hours incubation at the same concentration led to 80 % loss in activity (Figure 2-12-B). The inhibition by IAA appears less effective than ebselen. Indeed, 5 μ M ebselen used to covalently modify Ag85C results in 75 % inhibition after 10 min and more than 90 % inhibition of Ag85C activity

after 20 min (Figure 2-13). IAA reacts with thiols non-specifically; thus, it was expected to observe low levels of modification/inhibition.

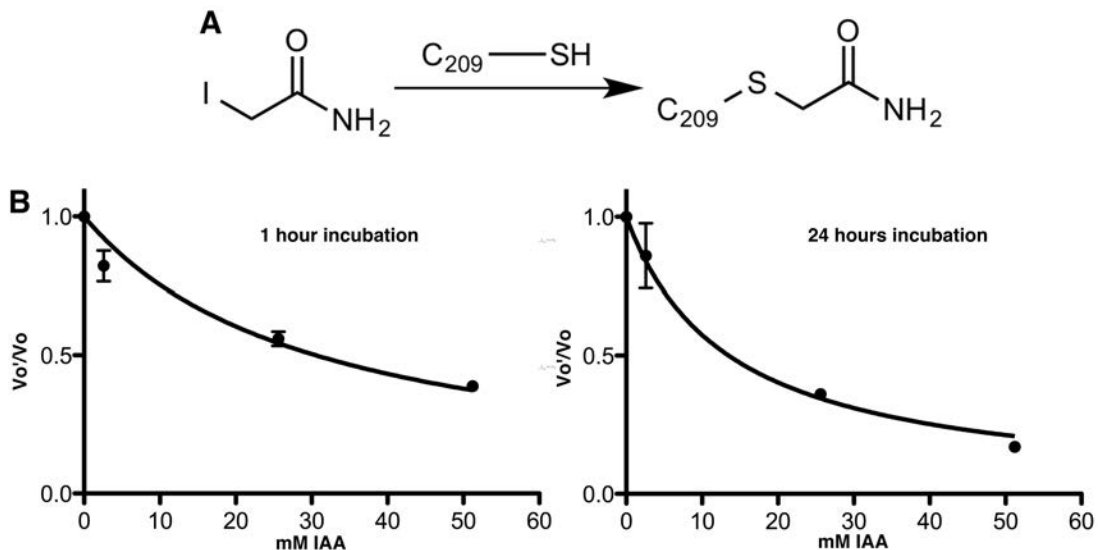


Figure 2-12: Modification of Ag85C by IAA. A) Scheme of C209 residue modified with iodoacetamide. B) IAA dose-dependence after one hour (left) and 24 hours (right) incubation. V_0'/V_0 corresponds to the ratio of the initial velocities for the inhibited reaction (V_0') and the uninhibited reaction (V_0). Error bars were calculated from triplicate reactions.

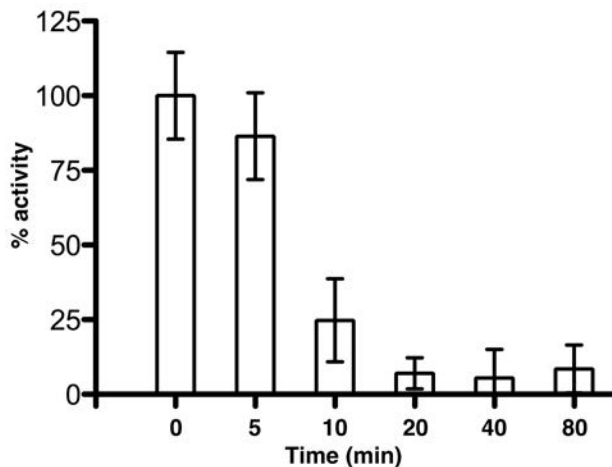


Figure 2-13: Time course of Ag85C inhibition by ebselen. Activity was normalized to wild-type enzyme. Error bars were calculated from triplicate reactions. Less than 10 % activity remains after 20 min incubation of Ag85C with ebselen.

2.3.4 C209 mutants display a nearly complete loss in Ag85C activity

M. tb has the ability to easily promote resistance to drugs through missense mutations. BTZ043 is an example that illustrates the emergence of *M. tb* resistance to drugs⁶². BTZ043 is a benzothiazinone compound currently in clinical trials that targets DprE1. The latter is a protein part of the heteromeric enzyme named decaprenylphosphoryl- β -D-ribofuranose involved in the formation of decaprenylphosphoryl- β -D-arabinofuranose (DPA), a key intermediate in the biosynthesis of AG and LAM. Recently, BTZ043 was shown to act as a suicide inhibitor of DprE1 by forming a covalent adduct with a cysteine (C387) located in the active site¹¹³⁻¹¹⁵. The covalently modified cysteine is not involved in the catalysis performed by DprE1. *M. tb* strains resistant to BTZ043 have been discovered; each of these strains present a missense mutation to either glycine or serine at the 387 residue. Therefore, it is important to look for potential missense mutations at the cysteine codon in the *fbp* genes.

To this purpose, site-directed mutagenesis was performed to obtain the following single-nucleotide mutants: Ag85C-C209S, Ag85C-C209G and Ag85C-C209F. Additionally, following a BLAST search using the *M. tb* Ag85C (H37Rv strain) sequence, a multiple sequence alignment of 564 mycobacterial Ag85 and related proteins was carried out. Based on the sequence alignment (Figure 2-14-A), a cysteine residue at position 209 is observed in 85 % of the Ag85 enzymes, while a serine residue is found in 13 % of the cases. An alanine residue is present in 2 % of the sequences. Consequently, site-directed mutagenesis was again used to produce the double-nucleotide mutant C209A.

The different mutants were assayed using the fluorometric Ag85 activity assay and their relative enzymatic activities were compared to the wild-type enzyme (Figure 2-14-B). A reaction using Ag85C and an excess of ebselen was also performed for comparison. Each of the mutants displayed a profound loss in activity *in vitro*. The double-nucleotide mutant Ag85C-C209A exhibits the highest level of activity among the mutants, but it only retains 10 % of the wild-type Ag85C activity.

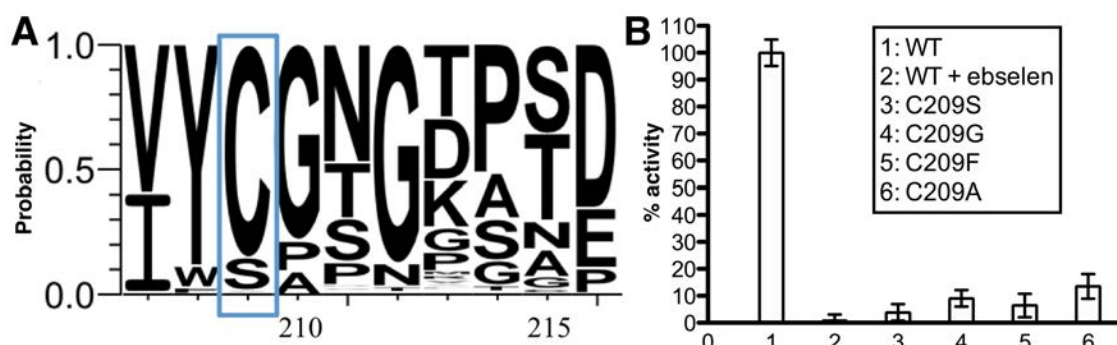


Figure 2-14: Potential mutations of C209 residue and effects on enzymatic activity. A) Sequence alignment of 564 mycobacterial Ag85 and related proteins. The residue 209 is highlighted in blue. B) Comparison of the enzymatic activity for the different Ag85C mutants. Activity was normalized to wild-type Ag85C, error bars were calculated from triplicate reactions. A reaction of Ag85C modified with an excess of ebselen was carried out as a control.

Functional redundancy is a phenomenon commonly observed in mycobacteria. For instance, the Ag85 complex actually includes four secreted proteins. The fourth enzyme, Ag85D, is inactive¹¹⁶⁻¹¹⁸. For that reason, there is no guarantee that the different mutations observed for the Ag85 enzymes among all the mycobacterial strains lead to active enzymes; some of them might be redundant proteins lacking any enzymatic activity. Interestingly, Ag85D possesses a serine instead of a cysteine at residue 209.

Although C209 does not participate directly in the catalysis performed by Ag85C, the lack of enzymatic activity for the different mutants leads to the hypothesis that C209 might play a significant role in the Ag85 activity.

2.3.5 Ebselen disrupts the Ag85C active site structure

As mentioned previously, all three enzymes display an α/β -hydrolase polypeptide fold and a conserved catalytic triad⁷⁰⁻⁷². The latter is formed by residues S124, E228 and H260 in Ag85C. The hydrogen-bonded network between the catalytic triad residues confers a strained kink in helix α_9 , which harbours E228⁷⁰ (Figure 2-15).

Covalent modification of S124 with a non-specific serine protease inhibitor, diethyl-*p*-nitrophenylphosphate, disrupts the hydrogen-bonded network connecting the residues of the catalytic triad and triggers the relaxation of the strained kink in helix α_9 (Figure 2-15)⁷⁰. An intriguing aspect of this change is the location of C209 relative to the kink in helix α_9 . Residue C209 is located at the C-terminus of β -strand β_7 in a buried hydrophobic pocket where the C209 side chain residue interacts with the peptide bond connecting T231 to L232 via van der Waals interactions. The kink in helix α_9 is positioned at the peptide bond linking residues T231 and L232.

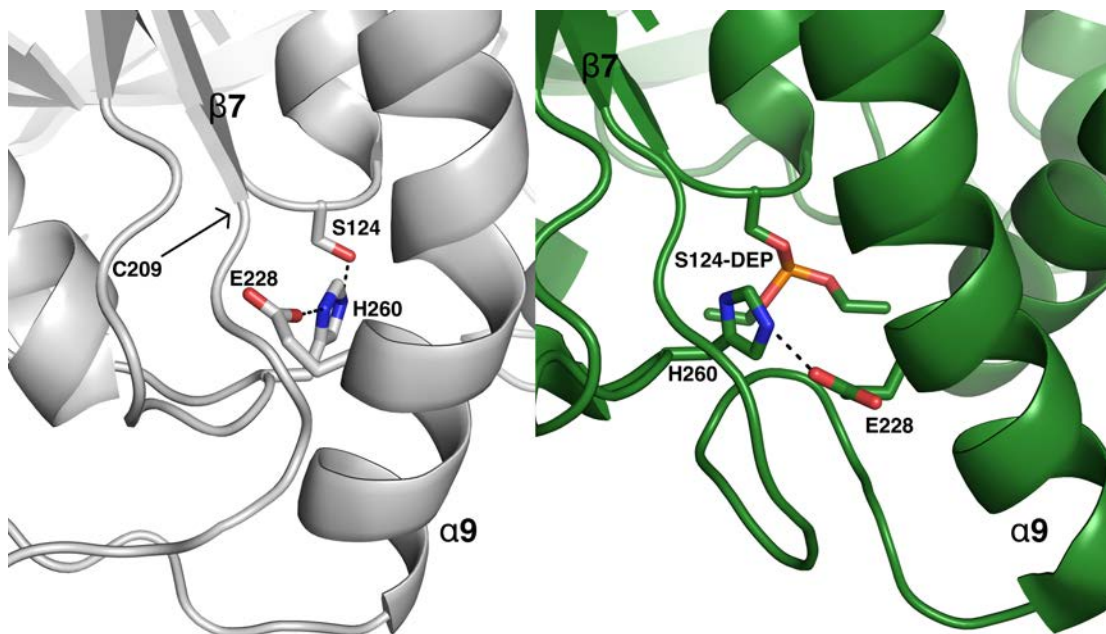


Figure 2-15: Close up view of the Ag85C active site in the native enzyme (PDB: 1DQZ, grey) and the enzyme covalently modified with diethylphosphate or DEP (PDB: 1DQY, green). The residues of the catalytic triad are represented with sticks and colored by CPK. The position of C209 is highlighted with an arrow.

To gain more insights on the structural effects of C209 modification resulting in Ag85C inactivation, X-ray crystallography experiments were carried out. Ag85C was co-crystallized with ebselen, and the structure was solved to 1.35 Å resolution (PDB: 4MQM). Information about data collection and refinement statistics is displayed in Table 2-4. For clarity, the structure will be referred to as the Ag85C-EBS structure for the rest of the manuscript. Although the mass spectrometry data clearly demonstrated the formation of a covalent adducts between Ag85C and ebselen and the 2Fo-Fc density of C209 appears clearly visible, no visible density corresponding to the ebselen moiety was observed (Figure 2-16). An interesting fact is that the Ag85C-EBS is isomorphous with

the Ag85C-mercury crystal structure that was originally used to solve the native Ag85C⁷⁰. In this structure, a mercury atom was covalently attached to residue C209.

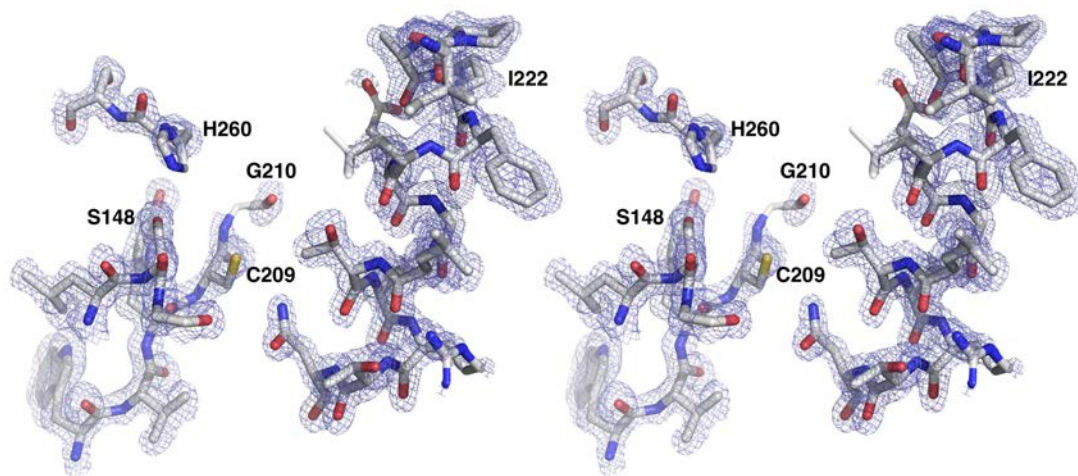


Figure 2-16: Stereo view for the disordered region observed near the C209 residue. The 2Fo-Fc map (blue) was contoured at 1σ . The residues 147-149, 206-235 and 260-261 are modelled in sticks. The lack of density for the loop region T212-N221 suggests significant flexibility. The side chain of H260 residue is not resolved.

Low RMS displacement values for the C α atoms (0.53 Å) when superimposing the Ag85C-EBS structure onto the native Ag85C structure indicate that both structures are very similar. However, some differences are noticeable upon closer inspection. As mentioned previously, C209 side chain interacts with the strained kink of helix α 9 through van der Waals interactions. More specifically, the side chain interacts with the peptide bond between T231 and L232. When C209 is modified by ebselen, the van der Waals interaction with the strained kink in helix α 9 is lost, leading to a relaxation of helix α 9 similar to the one observed in Ag85C-DEP⁷⁰. Indeed, a low RMS displacement value for the C α atoms (0.44 Å) when superimposing Ag85C-EBS and Ag85C-DEP indicates

the notable similarity between the two structures. Therefore, the Ag85C-EBS appears more similar to the DEP-modified structure than the native Ag85C structure.

The relaxation of helix $\alpha 9$ promotes the repositioning of residue E228 away from H260 and consequently disrupts the hydrogen-bonded network between the catalytic triad, leading to an inactive enzyme. In the DEP-modified structure, as S124 is covalently modified by DEP, H260 side chain repositions itself to maintain a hydrogen bond with E228, and additionally interacts with the side chain of S148 instead of the serine nucleophile, residue S124⁷⁰. Nevertheless, the shift of helix $\alpha 9$ is more exaggerated in the Ag85C-EBS structure than in the Ag85C-DEP structure when compared to the native form of the enzyme. Steric hindrance due to covalent modification of C209 by ebselen can explain the larger shift (Figure 2-17). As a result, the C α for residue E228 has shifted 6.1 Å from its original position in the native Ag85C structure and the hydrogen bond between E228 and H260 is broken. This phenomenon promotes disorder in the H260 side chain (Figure 2-16). The B-factor for H260 C γ is 36.4 Å², which is much higher than for previous Ag85C structures (14.7 Å² in average).

Another significant difference between the Ag85C-EBS and the native or the DEP-modified structure is the lack of electron density for the loop region (residues T211-N221), suggesting significant flexibility. This loop region is thought to be involved in the binding of the mycolyl acceptor to the active site⁷⁰⁻⁷².

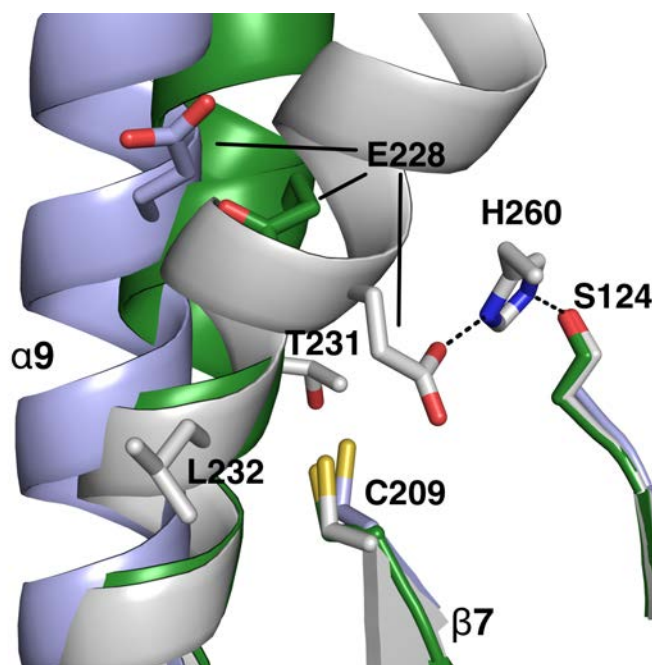


Figure 2-17: Superimposition of Ag85C (grey, 1DQZ), Ag85C-DEP (green, 1DQY) and Ag85C-EBS (blue, 4MQM). The covalent attachment of ebselen to C209 residue promotes the relaxation of helix $\alpha 9$ and consequently the disruption of the active site hydrogen-bonded network.

The lack of observable density for ebselen in the Ag85C-EBS structure can be attributed to two different phenomena. First, ebselen only possesses three heteroatoms; the hydrophobic nature of ebselen does not promote any specific interaction within the Ag85C active site. Thus it would be expected to see very little density for ebselen. The C209 S γ atom in Ag85C-EBS exhibits a higher B-factor (33 \AA^2) than in the native or the DEP-modified structure (17 and 20 \AA^2 , respectively), indicating that the C209 side chain is more dynamic in the Ag85C-EBS structure. Additionally, another phenomenon that could explain the lack of density for ebselen is radiation damage. Indeed, it has been shown that solvent-exposed disulfide bonds can be easily oxidized when subjected to X-

ray radiation¹¹⁹⁻¹²³. Hence, a selenenylsulfide bond would likely be even less stable than a disulfide bond. The combination of these two phenomena could explain the lack of density for ebselen.

The structure of Ag85C-C209S was solved to determine whether or not the same structural change is responsible for the inactivity of the C209 mutants. The structure was solved to 1.3 Å resolution. Data collection and refinement statistics are displayed in Table 2-4. Superimposing the Ag85C-EBS and Ag85C-C209S structures provides a low RMS displacement value for C α atoms (0.47 Å), indicating the strong similarity between the two structures. Again, the relaxation of helix α 9 is observed. However, compared to the Ag85C-EBS structure, the H260 side chain is resolved and maintains a hydrogen bond with S148 instead of the serine nucleophile (Figure 2-18). Although the shift of helix α 9 is less pronounced than in the Ag85C-EBS structure and more closely resembles the shift observed in the DEP-modified structure, the hydrogen bond between H260 and E228 is broken (Figure 2-18). Additionally, the loop region composed of residues T211 to N221 is resolved in this structure.

Again, the straightening of helix α 9 and consequently the alteration of the hydrogen-bonded network within the residues of the catalytic triad explains the lack of activity for this mutant. Thus it appears that replacing the cysteine at position 209 by a more polar residue such as serine weakens the van der Waals interaction with the strained kink in helix α 9 (Figure 2-18). It is expected that the C209 mutants with similar or larger polar side chains would exhibit a similar structure to the Ag85C-C209S mutant. Additionally, a large hydrophobic residue such as phenylalanine would likely promote

some steric hindrance, preventing the van der Waals interaction. This is suggested by the low enzymatic activity of the Ag85C-C209F mutant.

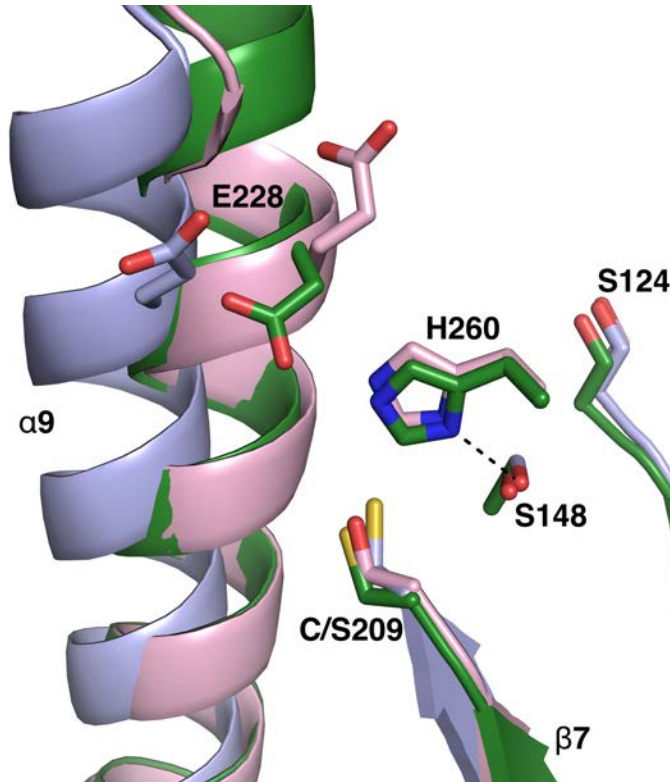


Figure 2-18: Superimposition of Ag85C-DEP (green, 1DQY), Ag85C-EBS (blue, 4MQM), and Ag85C-C209S (pink, 4MQL). The mutation of C209 to a more polar residue leads to the relaxation of helix $\alpha 9$ and the disruption of the catalytic triad interactions. H260 interacts with S148 instead of the serine nucleophile S124.

Table 2-4: Data collection and refinement statistics

Data Collection	Ag85C-EBS	Ag85C-C209S
Space Group	P2 ₁ 2 ₁ 2 ₁	C2
Unit Cell Dimensions		
<i>a</i> , <i>b</i> , <i>c</i> (Å)	60.6, 68.1, 75.1	135.8, 68.2, 35.9
α , β , γ (°)	90.0, 90.0, 90.0	90.0, 94.0, 90.0
Resolution (Å)	50.0-1.35	50.0-1.30
<i>R</i> _{sym}	6.9 (63.6)	5.1 (24.1)
<i>I</i> / σ <i>I</i>	11.3 (2.6)	15.3 (6.8)
Completeness (%)	99.2 (93.6)	99.5 (96.4)
Redundancy	10.5 (8.2)	7.4 (5.7)
Refinement		
Resolution (Å)	50.0-1.35	50.0-1.30
No. Reflections (Unique)	723910 (68823)	588562 (79869)
<i>R</i> _{work} / <i>R</i> _{free}	17.0/19.1	15.9/16.9
No. atoms		
Protein	2105	2226
Water	163	278
<i>B</i> -factors (Å ²)		
Protein	16.8	12.1
Water	26.0	21.6
R.m.s. deviations		
Bond lengths (Å)	0.005	0.006
Bond angles (°)	1.061	1.132

2.3.6 Screening of Ebsulfur and Ebsulfur derivatives

Ebsulfur is a compound similar to ebselen, except it possesses a sulfur atom in place of the selenium atom. The replacement of the selenium atom by a sulfur atom is an interesting feature to study, as ebselen could be cytotoxic due to the presence of the selenium atom. Dr. David Frick from University of Wisconsin-Milwaukee and the Milwaukee Institute for Drug Discovery provided us with a library of ebsulfur derivatives.

The library of ebsulfur derivatives was tested using the fluorometric Ag85 assay previously described. The compounds were incubated for 15 minutes with Ag85C before initiating the reaction by addition of resorufin butyrate. Three negative controls (no enzyme present) and three positive controls (with enzymes) were run in parallel. The result of the screening is displayed in figure 2-19. Two compounds, KU198 and KU208, exhibit levels similar to the negative controls. However, further testing indicated that KU208 was a false positive. In fact, the structure of KU208 is comparable to KU200, KU201 or KU207, which do not display any significant level of inhibition.

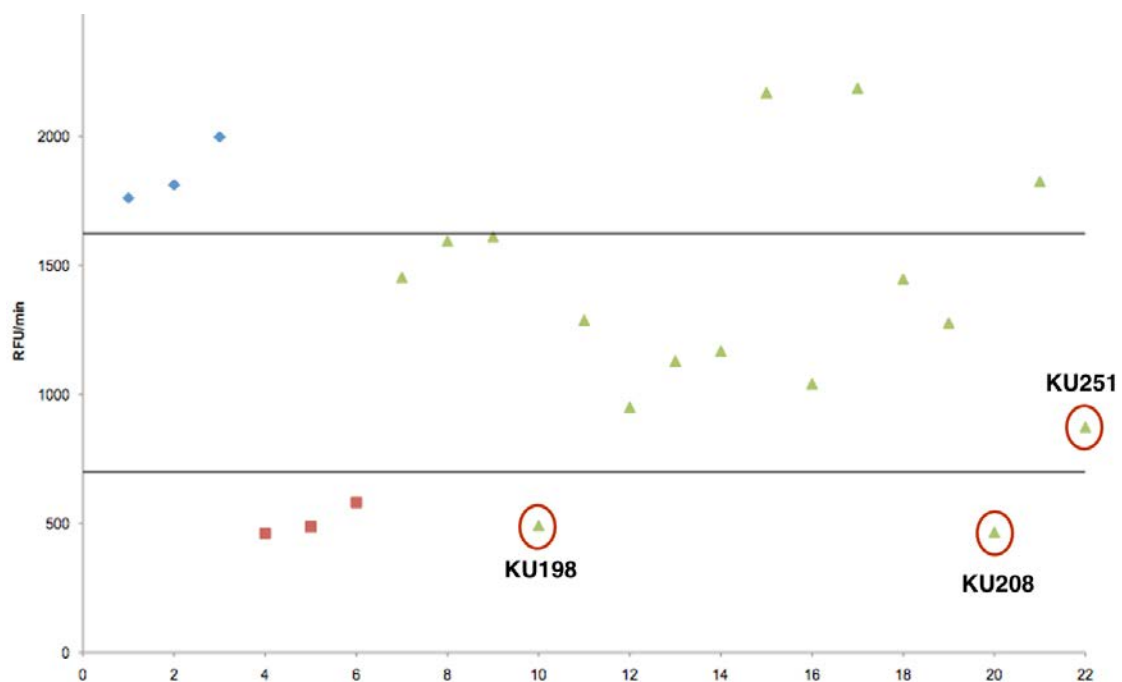


Figure 2-19: Screening of ebsulfur derivatives. Positive controls are colored in blue, negative in red and compounds tested in green. The two black lines represent the three times standard for each control. Those circled in red are compounds further characterized.

A dose-dependence experiment was carried out for KU198, the derivative showing the highest level of inhibition from the previous screening (Figure 2-20-A). Additionally, a dose-dependence experiment was performed for KU251, i.e. ebsulfur, to compare the inhibition level with ebselen (Figure 2-20-B). Ebsulfur exhibits a K_i in the low micromolar range (7.51 μM), indicating that ebsulfur has a binding affinity significantly lower than ebselen ($K_i = 63.0 \text{ nM}$). Thus, ebsulfur seems less reactive with C209 residue than ebselen. KU198 displays a K_i of 381.8 nM, which is still six times higher than ebselen, again exhibiting the lower reactivity of sulfur compared to selenium. However, KU198 is clearly more reactive than ebsulfur. Since this X-ray crystal structure has not yet been determined, the interactions promoting stronger inhibition by KU198 are not yet known. However differences in chemical properties between KU198 and ebsulfur may explain the differences in inhibition levels. Specifically, KU198 possesses an imide moiety that can act as a better leaving group than the amide due to resonance stabilization generated by the two carbonyl groups.

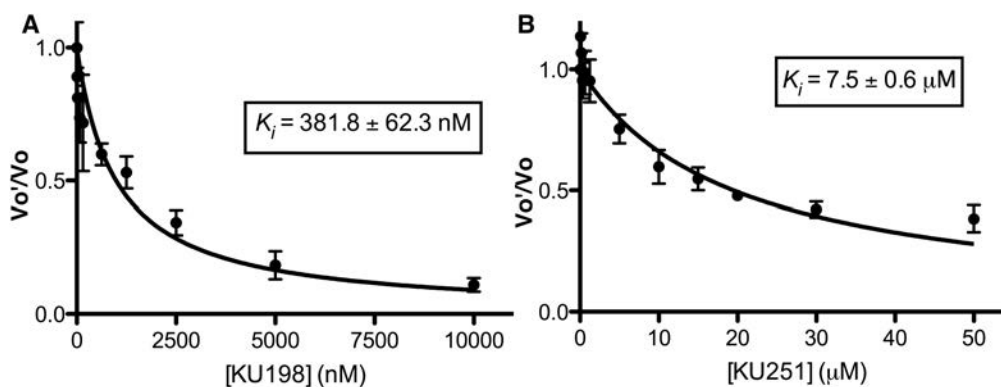


Figure 2-20: KU198 and KU251 dose-dependences. V_0'/V_0 corresponds to the ratio of the initial velocities for the inhibited reaction (V_0') and the uninhibited reaction (V_0). Error bars were calculated from triplicate reactions.

The reaction of C209 from Ag85C with KU198 leads to the formation of a disulfide bond that might be more stable when subjected to X-ray diffraction studies when compared to the selenenylsulfide bond formed with ebselen. For that reason, co-crystallisation of Ag85C with KU198 was attempted. Ag85C (1.5 mg/mL) was incubated with 100 μ M of KU198 for 1 hour. Then, the complex was concentrated using ultracentrifugation. Ag85C-KU198 was crystallized against a well solution of 1.26 M potassium phosphate monobasic monohydrate and 0.14 M sodium phosphate dibasic at pH 5.6 using the hanging-drop vapor diffusion technique. Different additives such as glycerol, ethylene glycol or diverse NDSB (non-detergent sulfobetaines) were added to improve the quality of the crystals (Figure 2-21). The data will be collected at the APS-ANL (IL).

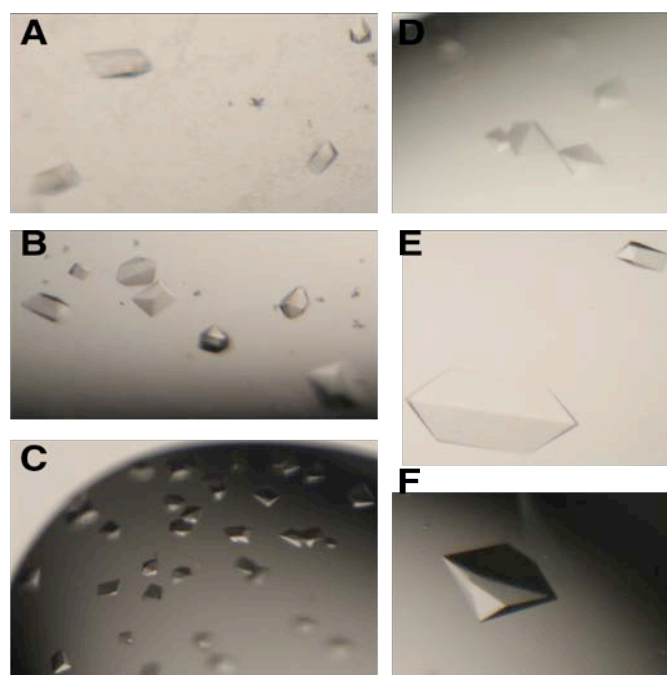


Figure 2-21: Crystals of Ag85C-KU198 grown in presence of different additives. A) Glycerol. B) Ethylene glycol. C) NDSB-201. D) (+/-)-1,3-butanediol. E) NDSB-256. F) NDSB-195.

2.3.7 Screening of Ebselen derivatives

Sandeep Thanna from Dr. Steven Sucheck's laboratory synthesized a small library of ebselen derivatives. The compounds were derivatized on the second aromatic moiety.

The compounds are expected to exhibit K_i values very similar to the one obtained for ebselen. Therefore, time course experiments were carried out to compare the efficiency of the different ebselen analogs. The enzymatic activity of the different samples of Ag85C covalently modified with these analogs was tested using the fluorometric Ag85C assay following different incubation times (0, 5, 10, 20, 40 and 80 minutes). All the reactions were performed in triplicate. The results are displayed in figure 2-22.

TSN-02-159(b) appears to be the least efficient compound as it takes 80 minutes to reach 90% inhibition. This might be due the presence of a cyclohexane group that is an electron-donating group and therefore makes the nitrogen of the amide a poorer leaving group. TSN-02-140(a) is also less efficient when compared to ebselen. Overall, all the derivatives are fairly similar and inactivate the enzyme in less than 20 minutes. Nonetheless, a larger library of derivatives is required to produce interpretable trends and reach reliable conclusions about which chemical factors affect the inhibitory activity of these compounds.

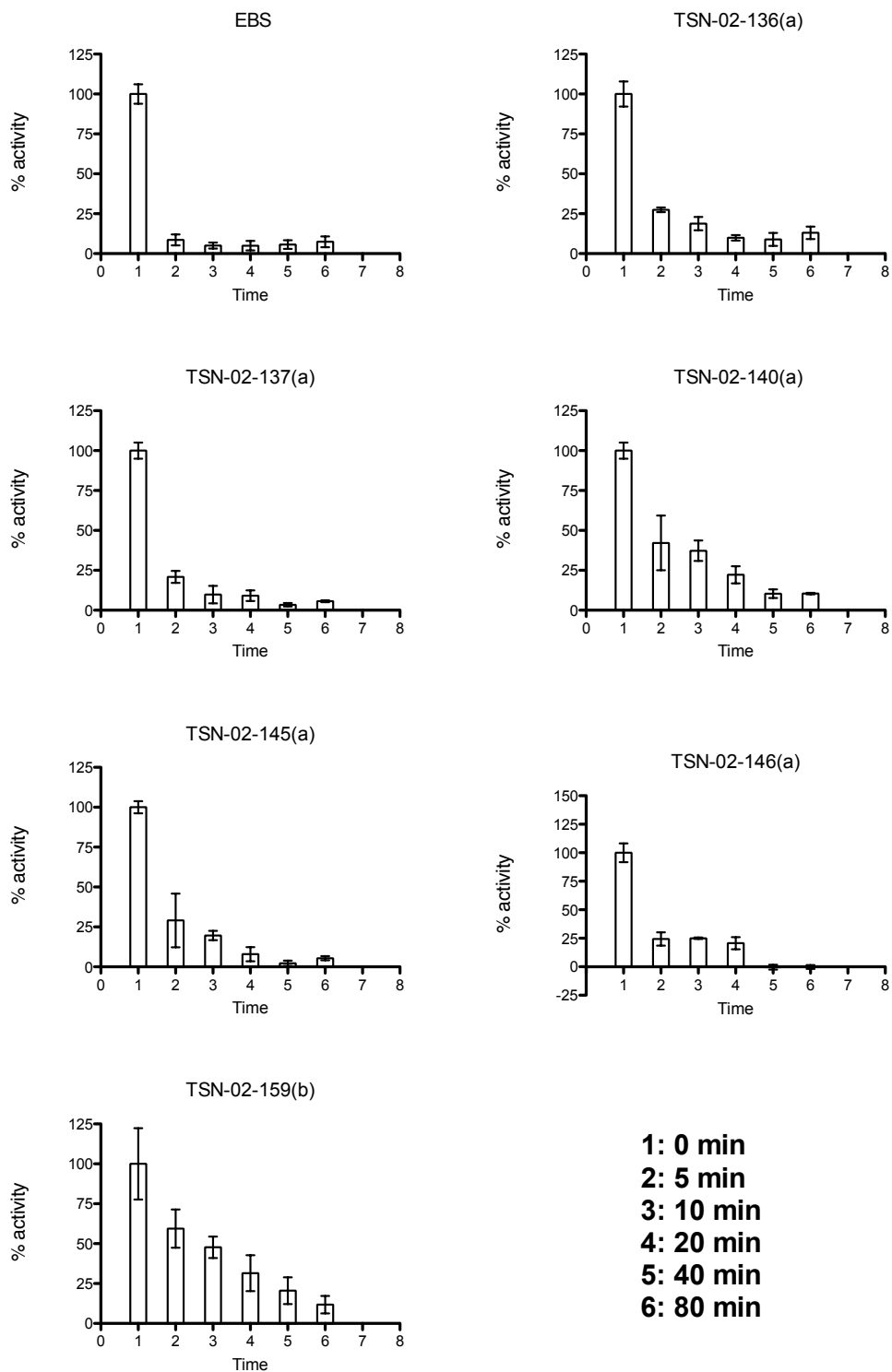


Figure 2-22: Time course experiment with the different ebselen analogs. The activities were normalized to wild-type enzyme and the error bars are calculated from triplicate reactions.

2.4 Conclusion and future work

This study allowed us to identify a potent inhibitor of the Ag85 complex. Ebselen was shown to specifically inhibit mycobacterial growth with a MIC of 20 $\mu\text{g/mL}$ against *M. tb* mc²6206. Because of the presence of mycothiol (a functional analog to glutathione) in the mycobacterial cytoplasm, the inhibitor effects produced by ebselen should occur in an oxidizing environment, such as the extracellular environment or the periplasmic space. As the Ag85 enzymes are secreted proteins, they are located in the periplasmic space. Ebselen was shown to inhibit mAG, as well as TDM production in culture, confirming the Ag85 complex as the target of ebselen.

Mass spectrometry experiment confirms that ebselen acts as an allosteric covalent inhibitor. The compound covalently modifies a lone cysteine located near the active site, resulting in the formation of a selenenylsulfide bond. Based on the structure of Ag85C crystallized in presence of ebselen, the modification of C209 forces the kinked helix $\alpha 9$ to adopt a straightened conformation. Consequently, the hydrogen-bonded network between the residues of the catalytic triad is disrupted and the enzyme is inactivated. The cysteine at position 209 was mutated to smaller (G and A) and larger hydrophobic (F) residues, as well as more polar residues (S). The different mutants exhibit almost no enzymatic activity. The Ag85C-C209S structure adopts a similar inactive conformation as observed for the Ag85C-EBS structure.

Although C209 does not participate in the catalytic reaction carried out by Ag85C, the cysteine is an important structural feature of the enzyme. The presence of the cysteine maintains the strained kink in helix $\alpha 9$ and allows the positioning of the catalytic

triad residues to perform catalysis. Any modification or mutations of C209 result in a significant to a complete loss of enzymatic activity. This mechanism of inhibition suggests a very low probability of developing drug resistance. In fact, if the organism were to mutate one of the Ag85 enzymes to generate resistance to ebselen, the mutant would likely exhibit low level of activity while the two other enzymes would still be inhibited. The same would still be true if two enzymes would undergo mutation with the third one being inhibited. Inhibition/mutation(s) of the Ag85 complex would lead to a significant reduction of TDM and mAG productions, and consequently would enhance the permeability of the mycomembrane to other antibiotics.

Efforts continue to identify compounds that would inhibit the Ag85 complex in a similar manner as ebselen but with more specificity toward the three enzymes. Additionally, Dr. Sucheck's laboratory is synthesizing ebselen conjugated with biotin. This compound could be used for a pull-down assay in order to identify the Ag85 complex and any other potential targets of ebselen *in vivo*. Upon covalent modification of a protein by a biotin derivatized ebselen in culture, the modified protein could bind to streptavidin and thus be isolated and identified using mass peptide fingerprint. A construct containing streptavidin was cloned with a C-terminal poly-histidine tag for that purpose.

Chapter 3

A novel approach to target the Ag85 complex

3.1 Background

The selenazole compound ebselen was found to inhibit the Ag85 complex using a mechanism not previously considered for these proteins as described in the prior chapter. Ebselen reacts with a conserved cysteine residue (C209 in Ag85C) located near the active site of the enzyme resulting in the formation of a selenenylsulfide bond. This covalent modification forces a kinked α helix ($\alpha 9$) to adopt a relaxed or straightened conformation that disrupts the hydrogen-bonded network within the catalytic triad of the enzyme and inactivates Ag85C. The covalent modification and enzymatic inactivation were confirmed for each of the *M. tb* encoded Ag85 enzymes using mass spectrometry and enzymatic inactivation, respectively. However, the X-ray crystal structure solved using Ag85C crystallized in the presence of ebselen (Ag85C-EBS, PDB 4MQM) did not exhibit density representing the covalent modification.

Since the lack of visible ebselen was likely due to radiation damage during the diffraction experiment, Chapter 3 describes the efforts to better understand how covalent modification or mutation at the cysteine residue is responsible for the inactive

conformation adopted by the enzyme. Toward this aim, Ag85C was covalently modified with the thiol reactive compounds iodoacetamide and *p*-chloromercuribenzoate; the resulting crystal structures exhibit the same disruption of the hydrogen-bonded network within the active site as the ebselen structure. A new crystal structure of Ag85C reacted with ebselen was also solved, with density observed for ebselen. Mutation of the cysteine to a glycine leads to an identical conformational change. Finally, because the conformation of helix $\alpha 9$ is highly sensitive to chemical changes near the active site, the effects of mutations in the catalytic triad were assessed using activity assays and by structure determination. These data provide further insights toward novel mechanisms to efficiently inhibit the Ag85 complex in mycobacteria.

3.2 Experimental procedures

3.2.1 Molecular cloning

The molecular cloning for *fbpC-S124A* and *fbpA-S126A* was carried out by Dr. Lajiness⁸⁷. The mutants C209G, E228Q and H260Q were cloned by site-directed mutagenesis using the construct pET29-*fbpC* as the template. The construct pET28-*fbpB* was used as a template for the site-directed mutagenesis of Ag85B-S126A. The constructs pET28-*fbpA-H262Q* and pET28-*fbpB-H262Q* were also cloned; however, only pET28-*fbpC-H260Q* was further studied. The primers and their respective complements (Integrated DNA Technology) used to carry out the different site-directed mutagenesis are presented in table 3-1. DNA sequencing was performed by Eurofins MWG Operon to confirm the presence of the mutations.

Table 3-1: Primers used for site-directed mutagenesis on pET29-*fbpC*

C-E228Q	GGCGAAGTTCCTGCAGGGCCTCACCCCTGC
C-H260Q	CCGCCCAACGGAACACAGTCGTGGCCC
B-S126A	GCTGCAATCGGCTTGGCGATGGCCG

3.2.2 Protein purification of Ag85s and mutants

The different protein samples were prepared following a similar protocol described in section 2.2.2. The main difference is the first step of purification; a cobalt affinity was used instead of a nickel affinity column. The binding buffer included 20 mM Tris and 5 mM β -Me; the protein was eluted with a buffer containing 20 mM Tris 8.0, 150 mM imidazole and 5 mM β -Me. In some instances, the protein was dialyzed against a crystallization buffer that did not contain any DTT.

3.2.3 Enzymatic activity assay

The enzymatic activity of the different enzymes was tested using a fluorometric assay previously described in section 2.2.3. Each of the enzymes was tested at a concentration of 500 nM and compared to wild-type Ag85C.

The inhibition of Ag85C by *p*-chloromercuribenzoic acid was tested using the same fluorometric assay described previously. The enzyme was reacted with *p*-chloromercuribenzoic acid at a 5.0-fold molar excess. The enzymatic activity of the sample was tested after two hours incubation and an overnight incubation. A control

reaction with an unmodified Ag85C enzyme was also performed. All the reactions were carried out in triplicate. Analysis of the data was performed using Prism 5 software.

3.2.4 Crystallization and structure determination

All crystals were grown using the hanging-drop vapor diffusion method. Ag85C (6.2 mg/ml) was reacted with sodium *p*-chloromercuribenzoic acid (1.4 molar excess) for 2 hours and was crystallized against a well solution of 0.1 M sodium acetate trihydrate pH 4.5 and 25 % w/v PEG 3350. Ag85C (5.5 mg/ml) was incubated with iodoacetamide (IAA, 50 mM) at room temperature for 1 hour in the dark. Ag85C-IAA was crystallized in 0.2 M lithium sulfate monohydrate, 0.1 M bis-tris pH 5.5 and 25 % w/v PEG 3350. Ag85C (5.1 mg/mL) was also reacted with 200 μ M ebselen (10 mM stock solution in DMSO) for two hours on ice. The Ag85C-ebsele complex was crystallized in 0.1 M sodium acetate trihydrate pH 4.5 and 25 % w/v PEG 3350. These three samples lacked DTT in the crystallization buffer.

The crystals of Ag85C-C209G (5 mg/ml) were grown in 1.0 M ammonium sulfate, 0.1 M bis-tris pH 5.5 and 1 % w/v PEG 3350. For cryoprotection, PEG 3350 was added to a final concentration of 25 % prior to flash cooling in liquid nitrogen. Ag85C-E228Q (5 mg/ml) and H260Q (6.5 mg/ml) were crystallized in 0.1 M sodium acetate trihydrate pH 4.5 and 25 % or 20 % w/v PEG 3350 respectively in presence of 13 mM hexaethylene glycol monoethyl ether or 6 mM CHAPSO (Hampton Research).

All crystals were flash-cooled in liquid nitrogen before data collection. Diffraction data were collected at the LS-CAT beamline (Ag85C-Hg, Ag85C-IAA,

Ag85C-ebesen, Ag85C-C209G, and Ag85C-E228Q) or at the GM/CA-CAT beamline (Ag85C-H260Q) at the APS-ANL.

HKL2000 was used to index, integrate and scale the diffraction data⁹². Molecular replacement, when necessary, was carried out using EPMR⁹³. PDB 4MQM (Ag85C-EBS) was used as the template for each data set. Using the best solution from EPMR, rigid body refinement, simulated annealing, positional and B-factor refinement were performed with the refine tool in PHENIX⁹⁵. The model was manually corrected using COOT⁹⁶. The electronic Ligand Builder and Optimization Workbench (eLBOW) tool was used to define the geometric restraints of the ligands in the Ag85C-ebesen, Ag85C-Hg, Ag85C-E228Q and Ag85C-H260Q structures¹²⁴.

3.3 Results and Discussion

3.3.1 Modification of C209 by thiol reactive compounds triggers structural changes in the Ag85C active site

A new crystal structure of Ag85C reacted with ebselen was solved to 1.40 Å. To distinguish it from the previous Ag85C-EBS structure that lacked observable density for ebselen, the new crystal structure will be referred to as Ag85C-ebselen. Information about data collection and refinement statistics is displayed in table 3-2. The data were collected at a wavelength of 1.078 Å (11.5 keV). Collecting at a wavelength below the selenium K-edge (12.7 keV) decreases X-ray absorption and decreases the potential for further oxidation of the selenium and disruption of the selenenylsulfide bond. As expected, the new Ag85C-ebselen structure displays a similar conformational change to that previously observed. However, compared to the previously published crystal structure of Ag85C incubated with ebselen (referred as Ag85C-EBS; PDB 4MQM), difference density is observed for the selenenylsulfide bond, as well as the aromatic moiety harbouring the selenium atom. In contrast, difference density for the distal aromatic moiety is not. Nonetheless, the Fo-Fc omit map did not initially appear to account perfectly for the entire Ag85C/ebselen covalent complex (Figure 3-1-A). To further confirm the location of the selenium atom, an anomalous difference map was calculated. Although the data was collected at energy below the absorption edge of selenium, some anomalous scattering signal was observed and the resulting difference map gives the position of the selenium (Figure 3-1-B). In spite of the hydrophobic nature of ebselen, the molecule seems to be oriented toward the surface of Ag85C. There are two interactions that allow visualization of the proximal phenyl moiety of ebselen. The

amide moiety on ebselen is likely interacting with R239, even though the side chain of the arginine, particularly the guanidinium moiety, is not well resolved. The B-factors for atoms of the guanidinium moiety are between 30.4 and 39.4 Å², which is significantly higher than the average protein B-factor. Second, a π - π stacking interaction is observed between the first aromatic ring of ebselen and F254 of Ag85C.

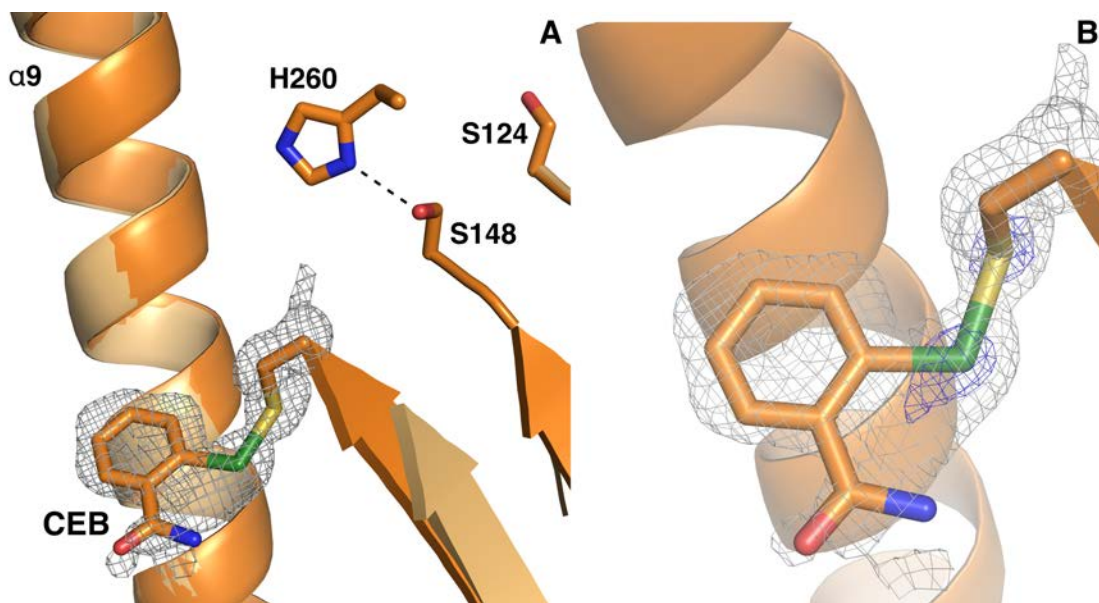


Figure 3-1: Ag85C-ebselen structure. A) Superimposition of the new Ag85C-ebselen (bright orange) and Ag85C-EBS (orange) structures. The electron density of a Fo-Fc omit map is shown contoured at 3σ (grey); the side chain of CEB (C209 modified by ebselen) residue was omitted during map calculation. B) Ag85C-ebselen structure (bright orange). The electron density of an anomalous map is shown contoured at 4σ (blue) in addition to the electron density of a Fo-Fc omit map for CEB side chain.

The rest of the structure is almost identical to the previous Ag85C-EBS as indicated by the low RMS displacement values observed for the C α atoms (0.4 Å). However, the loop connecting strand β 7 and helix α 9 (L β 7- α 9) composed of residues 210-222 is well ordered in this new crystal structure contrary to the previously published

structure. The conformation of L β 7- α 9 is similar to the one observed in the Ag85C-C209S structure (PDB 4MQL). Moreover, the H260 side chain, which was disordered in the Ag85C-EBS structure, is ordered in the Ag85C-ebsele structure and is forming a hydrogen bond with S148. Thus, the hydrogen-bonded network normally observed for the residues of the catalytic triad is disrupted.

To determine if covalent modification of cysteine at position 209 by any thiol reactive compound triggers a similar active site rearrangement, Ag85C was reacted with iodoacetamide and *p*-chloromercuribenzoate. Iodoacetamide is an alkylating reagent commonly used to characterize cysteine residues in biomolecules and previous studies show that covalent modification by iodoacetamide at C209 of Ag85C inactivates the enzyme⁸⁸. Additionally, *p*-chloromercuribenzoate is known to inhibit some enzymes requiring a cysteine residue for their activity. Both complexes were crystallized using a hanging-drop vapor diffusion technique and the corresponding X-ray crystal structures were solved. The crystal structures will be referred to as Ag85C-IAA (iodoacetamide-modified Ag85C) and Ag85C-Hg (Ag85C modified with *p*-chloromercuribenzoate), respectively. The Ag85C-IAA and Ag85C-Hg were solved to 1.50 Å and 1.90 Å, respectively. Information about data collection and refinement statistics is displayed in table 3-2. The two structures are isomorphous with the previously published Ag85C-EBS structure. Low RMS displacement values for the C α atoms (0.3 Å for Ag85C-IAA and 0.2 Å for Ag85C-Hg) when superimposing each structure onto the original Ag85C-EBS structure highlight the fact that both structures are very similar to the ebsele-modified form of Ag85C.

Each structure exhibits a relaxation of helix $\alpha 9$, but some differences are present upon closer inspection of the active site. The covalent modification of C209 promotes the observed conformational change stems by disrupting the van der Waals interactions between C209 and the kinked region of helix $\alpha 9$. Because of the covalent modification of C209 by these thiol-reactive compounds, the C209 side chain no longer interacts with the kink in helix $\alpha 9$ as observed in the native structure (Figure 2-15, Chapter 2), which alters the Ag85C active site structure.

In the Ag85C-IAA structure, H260 interacts via hydrogen bonding with S148 instead of the serine nucleophile S124. Additionally, the C α position for E228 shifted 6.2 Å away in comparison to the native Ag85C structure. Consequently, E228 and H260 no longer interact through a hydrogen bond between their side chains in contrast to that observed in the native structure. The structure exhibits complete difference density for the acetamide moiety (YCM residue) as shown in figure 3-1-A. In fact, the resulting thioether moiety is more stable than the selenenylsulfide bond formed when Ag85C is reacted with ebselen. The better resolution of the acetamide-containing product might be explained by the fact that the thioether is less sensitive to radiation damage compared to the selenenylsulfide bond.

Comparable to the Ag85C-EBS structure, disorder is observed in the H260 side chain in Ag85C-Hg structure (Figure 3-1-B), the B-factor for H260 C γ is 43.4 Å², which is much higher than for previous Ag85C structures (14.7 Å² in average). H260 does not strongly interact with either S124 or S148. Additionally, as in the Ag85C-EBS and Ag85C-IAA structures, a hydrogen bond is lacking between E228 and H260 for the Ag85C-Hg structure (Figure 3-1-B).

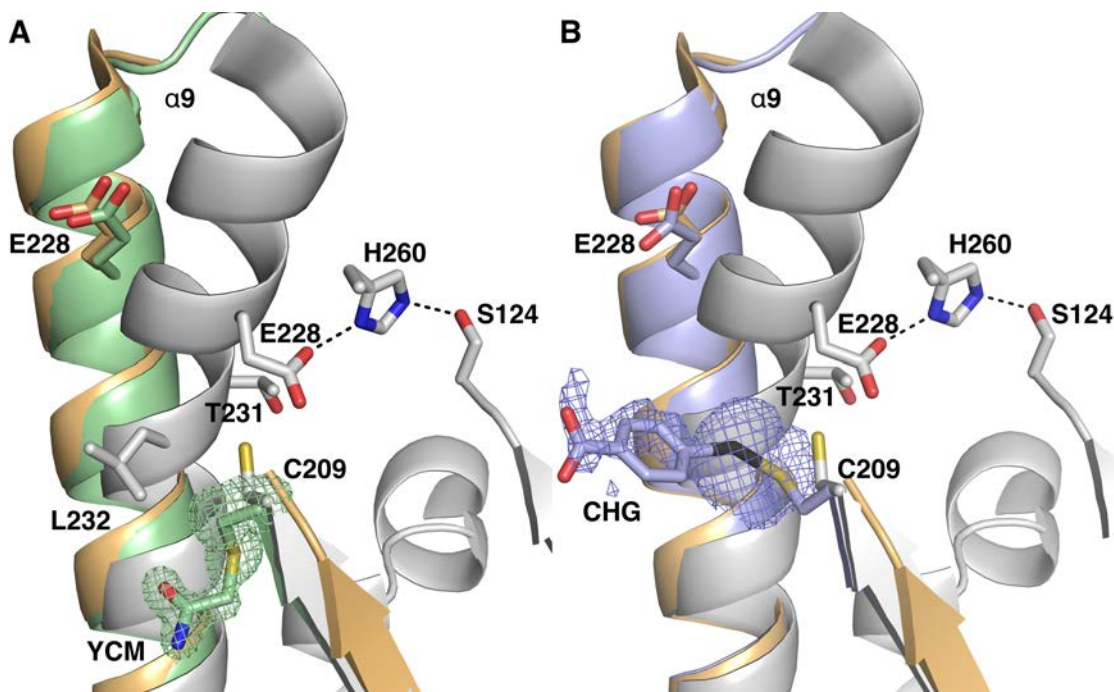


Figure 3-2: Ag85C-IAA and Ag85C-Hg structures. A) Superimposition of the native Ag85C (grey), Ag85C-EBS (orange) and Ag85C-IAA (green) structures. The density of a Fo-Fc omit map is shown contoured at 3σ (green); the side chain of YCM residue was omitted during map calculation. B) Superimposition of the native Ag85C (grey), Ag85C-EBS (orange) and Ag85C-Hg (blue) structures. The density of a Fo-Fc omit map is shown contoured at 3σ (blue); the side chain of CHG residue was omitted during map calculation.

Reaction of Ag85C with *p*-chloromercuribenzoic acid leads to inhibition of the enzymatic activity (Figure 3-3). After two hours incubation, the modified enzyme displays about 60 % of activity whereas after an overnight incubation, the enzymes retains about 30 % activity. The inhibition was expected based on the conformation adopted by helix α 9 in the Ag85C-Hg structure.

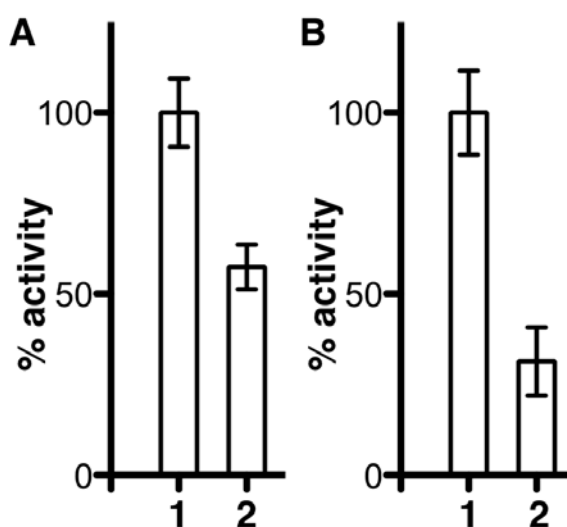


Figure 3-3: Inhibition of Ag85C by *p*-chloromercuribenzoic acid (5.0 molar excess). The enzymatic activity of the different samples was tested using a fluorescence-based assay. The activity is normalized to the unmodified enzyme Ag85C and the error bars are calculated from triplicate reactions. A) Inhibition of Ag85C by *p*-chloromercuribenzoic acid after 2 hours incubation. Bar 1 corresponds to the unmodified Ag85C while bar 2 relates to the Ag85C enzyme modified with *p*-chloromercuribenzoic acid. B) Inhibition of Ag85C by *p*-chloromercuribenzoic acid after overnight incubation. Bar 1 corresponds to the unmodified Ag85C whereas bar 2 relates to the Ag85C enzyme modified with *p*-chloromercuribenzoic acid.

Table 3-2: Data collection and refinement statistics for Ag85C-IAA/Hg/ebselen

Data Collection	Ag85C- ebselen	Ag85C- IAA	Ag85C-Hg
PDB Code	4QDU	4QDT	4QDO
Space Group	P2 ₁ 2 ₁ 2 ₁	P2 ₁ 2 ₁ 2 ₁	P2 ₁ 2 ₁ 2 ₁
Unit Cell Dimensions			
<i>a</i> , <i>b</i> , <i>c</i> (Å)	59.5, 67.8, 75.2	60.7, 68.0, 76.3	60.7, 68.0, 74.4
α , β , γ (°)	90.0, 90.0, 90.0	90.0, 90.0, 90.0	90.0, 90.0, 90.0
Resolution Range (Å)	50.0-1.40	50.0-1.50	50.0-1.90
Wavelength (Å)	1.07818	0.97872	0.97856
R _{sym} (Highest shell)	6.6 (30.4)	6.6 (37.0)	9.7 (45.8)
I/ σ I	26.8 (5.4)	28.2 (5.7)	27.7 (5.8)
Completeness (%) (Highest shell)	98.5 (90.8)	99.9 (100.0)	98.2 (96.2)
Redundancy (Highest shell)	6.4 (4.2)	7.3 (7.3)	13.1 (9.3)
Refinement			
Total Reflections (Unique)	384079 (59726)	375222 (51419)	319977 (24485)
R _{work} /R _{free}	14.6/18.2	14.7/17.5	19.3/24.0
B factors (Å ²)			
Protein	20.0	20.8	25.1
Water	32.6	32.0	28.1
Wilson B factor	14.9	16.4	20.2
R.m.s. deviations			
Bond lengths (Å)	0.006	0.006	0.009
Bond angles (°)	1.095	1.075	1.405
Ramachandran plot			
Favored (%)	96.14	96.32	95.49
Outliers (%)	0.70	0.00	0.38

3.3.2 Ag85C-C209G mutant displays a similar inactive conformation

Since each of the chemical modifications increases the bulk of the residue at position 209 and published data show that single nucleotide changes in codon 209 have a universally detrimental effect on enzyme activity, it is necessary to determine if C209 mutations that encode residues with a smaller molecular volume also disrupt the catalytic triad hydrogen bonded network.

To assess this, we determined the X-ray crystal structure of an Ag85C-C209G mutant. We have shown previously that the Ag85C-C209G mutant, although the side chain is a smaller hydrophobic residue, exhibits a very low level of enzymatic activity when compared to wild-type Ag85C (less than 10 % remaining activity)⁸⁸. The X-ray crystal structure of Ag85C-C209G was solved to 1.50 Å (Table 3-3). Again, the structure was isomorphous with Ag85C-EBS. When superimposing the Ag85C-C209G and Ag85C-EBS structures, the RMS displacement observed for the C α atoms is 0.2 Å, indicating clearly that the structure of the C209G mutant mimics that of the ebselen inactivated form. The crystal structure of Ag85C-C209G confirms that helix α 9 relaxes, repositions E228 resulting in the disruption of the hydrogen bond between E228 and H260, and H260 is positioned to form a hydrogen bond with S148.

Moreover, the Ag85C-C209G mutant structure is also comparable to the previously solved Ag85C-C209S structure (PDB 4MQL) (Figure 3-4)⁸⁸. Superimposing these two structures provides a RMS displacement value of 0.8 Å for the C α atoms. The main difference between the two mutants structures is the extent of the shift in helix α 9

when relaxed; the helix $\alpha 9$ in the Ag85C-C209G structure has shifted 6.2 Å compared to the wild-type enzyme whereas $\alpha 9$ in Ag85C-C209S has only shifted 3.5 Å.

Table 3-3: Data collection and refinement statistics for Ag85C-C209G

Data Collection	Ag85C-C209G
PDB Code	4QDX
Space Group	P2 ₁ 2 ₁ 2 ₁
Unit Cell Dimensions	
<i>a, b, c</i> (Å)	60.2, 68.4, 76.4
α, β, γ (°)	90.0, 90.0, 90.0
Resolution Range (Å)	50.0-1.50
Wavelength (Å)	0.97856
R _{sym} (Highest shell)	7.1 (39.8)
I/σI	35.7 (7.9)
Completeness (%) (Highest shell)	99.2 (100.0)
Redundancy (Highest shell)	13.9 (14.6)
Refinement	
Total Reflections (Unique)	695388 (50123)
R _{work} /R _{free}	17.9/19.3
B factors (Å ²)	
Protein	20.6
Water	28.9
Wilson B factor	18.1
R.m.s. deviations	
Bond lengths (Å)	0.006
Bond angles (°)	1.063
Ramachandran plot	
Favored (%)	97.00
Outliers (%)	0.37

The C209S mutant confers a stronger polarity than the cysteine while the C209G mutant imparts a lower polarity at that site and, as stated previously, has a much smaller

volume than the corresponding cysteine, which likely results in much weaker van der Waals interactions between residue 209 and helix $\alpha 9$. Therefore, the low level of Ag85C-C209G enzymatic activity appears to be a consequence of active site structural alterations identical to that observed for the other C209 mutants and the wild type enzyme covalently modified by thiol-reactive compounds but for different chemical reasons. This suggests that this region of the protein is supremely sensitive to chemical changes near the active site, which further suggests that the structural dynamics maybe significant for substrate recognition and binding during enzyme turnover.

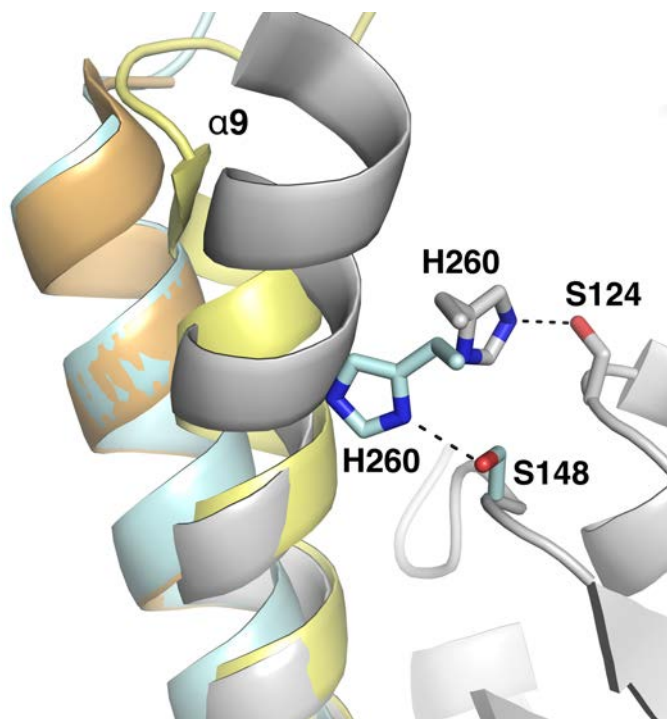


Figure 3-4: Superimposition of Ag85C (grey), Ag85C-EBS (orange), Ag85C-C209S (yellow) and Ag85C-C209G (cyan) structures. The H260 side chain interacts with the serine nucleophile S124 in the native structure whereas it interacts with a different serine residue (S148) in the Ag85C-C209G structure, explaining the lack of activity displayed by the mutant. The mutation promotes the relaxation of helix $\alpha 9$ similar to the one observed in Ag85C-C209S or Ag85C-EBS structures.

3.3.3 Mutation of any catalytic triad residue results in a loss of enzymatic activity and relaxation of helix α 9

Ultimately, since both the Ag85C-C209G and Ag85C-C209S structures exhibit the same conformational change, this suggests that the van der Waals interactions between C209 and helix α 9 help to maintain the strained kink in this helix and the hydrogen-bonded network between the three catalytic triad residues.

Using a radiometric mycolyltransferase assay, Belisle and co-workers have shown previously that mutation of the catalytic nucleophile S124 to an alanine leads to an inactive Ag85C enzyme⁶⁴. It was assumed that loss of enzymatic activity stems only from loss of the nucleophile that initiates the reaction. However, in the light of the new structural information, is useful to determine if mutation of any of the catalytic triad residues affects the structure helix α 9.

Site-directed mutagenesis was carried out to clone mutants corresponding to the other residues of the catalytic triad; both E228 and H260 were mutated to glutamine in order to disrupt the enzymatic activity while potentially maintaining the hydrogen bonds between the catalytic triad. The resorufin butyrate-based fluorometric assay used to assess the enzymatic activity of the C209 mutants was again used to test the enzymatic activity of the active site mutants. Ag85C-H260Q displays less than 10 % of activity when compared to the wild-type enzyme, while Ag85C-E228Q retains about 17 % of the wild-type activity (Figure 3-5).

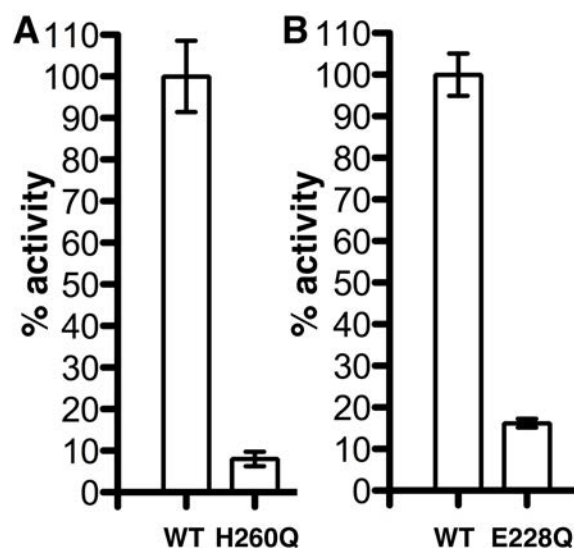


Figure 3-5: Effect of mutations among the catalytic triad residues. The enzymatic activity of the mutants was tested using a fluorescence-based assay. The activity is normalized to the wild-type enzyme Ag85C and the errors bars are calculated from triplicate reactions. The mutant Ag85C-H260Q exhibits less than 10% of activity compare to the wild-type Ag85C (A) whereas Ag85C-E228Q retains about 17% of wild-type activity (B).

X-ray crystallography experiments were carried out to gain insight into the structures of the three mutants. The crystal structures of Ag85C-E228Q and Ag85C-H260Q were solved to 1.90 and 1.35 Å, respectively (Table 3-4). Dr. Lajiness solved the crystal structure of Ag85C-S124A⁸⁷.

Table 3-4: Data collection and refinement statistics for Ag85C-E228Q and H260Q.

Data Collection	Ag85C-E228Q	Ag85C-H260Q
PDB Code	4QDZ	4QE3
Space Group	I222	P2 ₁ 2 ₁ 2 ₁
Unit Cell Dimensions		
<i>a</i> , <i>b</i> , <i>c</i> (Å)	68.2, 74.9, 136.1	60.7, 68.1, 76.3
α , β , γ (°)	90.0, 90.0, 90.0	90.0, 90.0, 90.0
Resolution Range (Å)	50.0-1.90	50.0-1.35
Wavelength (Å)	0.97872	0.97936
R _{sym} (Highest shell)	9.3 (56.1)	7.8 (51.3)
I/ σ I	31.5 (5.8)	16.0 (2.8)
Completeness (%) (Highest shell)	99.5 (98.8)	97.9 (85.5)
Redundancy (Highest shell)	13.1 (12.1)	5.5 (3.9)
Refinement		
Total Reflections (Unique)	371096 (28231)	377990 (68542)
R _{work} /R _{free}	16.3/18.7	17.2/19.4
B factors (Å ²)		
Protein	26.7	14.9
Water	31.1	27.1
Wilson B factor	24.1	11.5
R.m.s. deviations		
Bond lengths (Å)	0.007	0.005
Bond angles (°)	1.126	1.109
Ramachandran plot		
Favored (%)	96.24	96.59
Outliers (%)	0.38	0.76

Ag85C-H260Q is the only structure among the three mutants to be isomorphous with the Ag85C-EBS and the low RMS displacement value for the C α atoms after superimposing both structures (0.4 Å) confirm their structural similarity. The Ag85C-

S124A mutant crystallized in a C2 space group while the Ag85C-E228Q crystallized in a I222 space group.

Similarly to the phenomenon observed in the Ag85C-IAA or Ag85C-C209G structures, the Ag85C-S124A mutant exhibits a slight shift of the H260 side chain position that promotes the formation of a hydrogen bond with S148 while disrupting the hydrogen bond with S124 observed in the wild-type enzyme (Figure 3-6). Additionally, the helix $\alpha 9$ has shifted 4 Å with respect to its equivalent in the native Ag85C structure (PDB 1DQZ⁷⁰), which causes the repositioning of E228 and disrupts the hydrogen-bonded network within the catalytic triad. Contrary to the Ag85C-EBS structures or many of the others structures described previously, the loop L $\beta 7$ - $\alpha 9$ is well resolved in this crystal structure. This loop adopts a conformation similar to the Ag85C-C209S (PDB 4MQL) structure but very different from the one observed in the native Ag85C structure. The structure is also very similar to the Ag85C-DEP (PDB 1DQY) with a RMS displacement value of 0.9 Å for the C α atoms⁷⁰.

The Ag85C-E228Q structure also displays the same shift of the helix $\alpha 9$ as Ag85C-S124A. However, the H260 side chain is disordered in this structure; the B-factor for C β is 33.7 Å². Indeed, it appears that H260 may take two alternative conformations in this structure but neither is well resolved (Figure 3-6). One conformation likely interacts with the serine nucleophile S124 while the other one would form a hydrogen bond with S148.

Finally, the position of Q260 in the Ag85C-H260Q structure allows the formation of a hydrogen bond between O $\epsilon 1$ of the Q260 side chain and the side chain hydroxyl of S148 (Figure 3-6). In addition, this structure exhibits the same shift of the helix $\alpha 9$ as in

the Ag85C-C209G mutant, preventing the formation of any hydrogen bond between Q260 and E228.

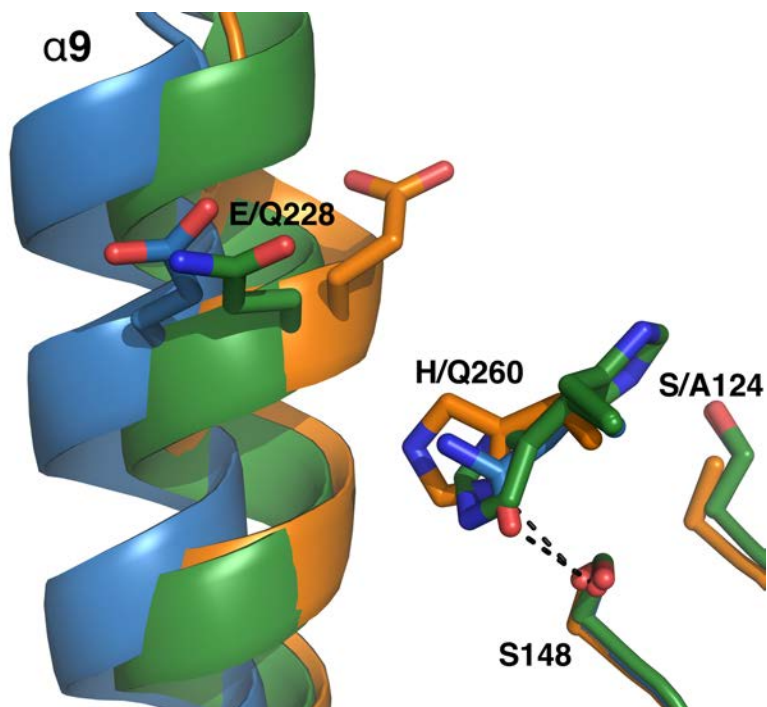


Figure 3-6: Superimposition of Ag85C-S124A (orange), Ag85C-E228Q (green) and Ag85C-H260Q (blue) structures. The three mutants exhibit a relaxation of helix $\alpha 9$, accounting for the loss of enzymatic activity.

Clearly the lack of a nucleophile in the S124A mutant will eliminate activity and the loss of the general base in the H260Q mutant will significantly decrease the activity. Similar to that observed for serine proteases, conversion of the third residue of the catalytic triad, in this case E228, to the corresponding amide-containing side chain causes a decrease in activity greater than what would be expected if the role of E228 is only to stabilize the imidazolium ion formed on H260 during catalysis^{125, 126}. The decrease in enzymatic activity of each of the Ag85C active site mutants can also be attributed to active site structural changes, because all three of the mutants exhibit the same

conformational change observed in the previously described structures where C209 was covalently modified. However, slight differences are apparent in the hydrogen-bonding pattern within the active sites of the three mutants. In both the Ag85C-S124A and Ag85C-H260Q, the residue 260 side chain interacts with S148 and the hydrogen bond between residues E228 and H260 is disrupted. However, in the Ag85C-E228Q structure, the H260 side chain is not well ordered and might be shifting between two different conformations. The conformation in which H260 hydrogen bonds with the serine nucleophile would explain the residual activity observed for Ag85C-E228Q (Figure 3-5).

The propensity of helix $\alpha 9$ to transition from the kinked to the relaxed state is highlighted by the comparison between the native form of Ag85C and the Ag85C-S124A structures. In the S124A mutant, the loss of a single hydrogen bond between H260 and the residue at position 124 is sufficient to promote helix $\alpha 9$ relaxation. This suggests that the enzyme has evolved to undergo this structural change following the formation of the acyl-enzyme intermediate and the likely disruption of the hydrogen bond between H260 and S124. Furthermore, the rearrangement of L $\beta 7$ - $\alpha 9$ that is concomitant with helix $\alpha 9$ relaxation can be hypothesized to play a role in substrate binding during the second half-reaction of the enzymatic mechanism⁷⁰. Based on published data, the enzymes of the Ag85 complex appear to have redundant activity *in vivo* based on the proposed ability to use TMM as a mycolyl-donor and subsequent transfer to a variety of substrates^{66, 117}. Additionally, Barry *et al.* have shown that trehalose-based compounds can be amended at various positions and still function as acyl donors¹²⁷. Both of these results suggest that the enzyme active site is structurally dynamic. The structures described here suggest that helix $\alpha 9$ relaxation maybe particularly important for selecting the mycolyl-donor during

catalysis. The Ag85B-trehalose crystal structure shows that the N-terminus of helix $\alpha 9$ forms a portion of the trehalose-binding site using residues P223 and A224, which are conserved in the *M. tb* Ag85 enzymes. However, upon relaxation of helix $\alpha 9$, P223 and A224 move and that portion of the active site is formed by L β 7- $\alpha 9$ in those structures where the loop is resolved. It is possible that the reshaping of the carbohydrate-binding site upon formation of the acyl-enzyme intermediate promotes binding of the arabinan within the Ag85C active site.

3.3.4 Further work with Ag85A and Ag85B-S126A

To determine whether the same conformational change was observed in each of the Ag85 enzymes, crystallization experiments were attempted with Ag85A-S126A and Ag85B-S126A. First, index screens (Hampton Research) were set up using the hanging-drop vapor diffusion technique for both mutants. The crystallization buffer for each enzyme was similar to the one previously used for Ag85C (20 mM Tris pH 7.5, 2 mM EDTA), omitting DTT to preserve a disulfide bridge in each structure. Both constructs, pET28-*fbpA-S126A* and pET28-*fbpB-S126A*, possess an N-terminal poly-histidine tag that is cleavable by a PreScissionTM protease. The index screenings were set up using the enzymes with or without a poly-histidine tag. As no crystals were obtained at first, Classics L Suite screenings (Qiagen) were also set using the hanging-drop vapor diffusion technique. Needle-type crystals were obtained for Ag85B-S126A at a concentration of 11.8 mg/mL (Figure 3-7-A). The mutant was crystallized in three different conditions, each containing (+/-)-2-methyl-2,4-pentanediol (MPD), a cryoprotectant present in the crystallization condition of the native Ag85B⁷¹. The

conditions were as follows: condition 50 (0.2 M ammonium acetate, 0.1 M bis-tris pH 5.5, 45 % w/v MPD), condition 51 (0.2 M ammonium acetate, 0.1 M bis-tris pH 6.5, 45 % w/v MPD) and condition 52 (0.2 M ammonium acetate, 0.1 M HEPES pH 7.5, 45 % w/v MPD). The crystals were analyzed at the APS but diffracted poorly. Optimization of these crystals was attempted using additive and detergent screens (Hampton Research). Addition of N,N-dimethyldodecylamine N-oxide (DDAO) allowed the growth of rod shaped crystals (Figure 3-7-B). These optimized crystals have not been yet tested for diffraction.

Additionally, Ag85A-S126A and Ag85B-S126A were co-crystallized in presence of a variety of carbohydrate-based detergents. Indeed, the presence of detergent could help in stabilizing the dynamic active site and may provide more insight in regards to the acyl-enzyme intermediate form of the Ag85A or Ag85B. The different detergents were the following: n-octanoylsucrose (NOS), n-octyl- β -D-thioglucoside (OTG), n-heptyl- β -D-thioglucopyranoside (HTG), n-octyl- β -D-glucoside (OG), n-dodecanoylsucrose (NDDS) and n-decanoylsucrose (NDS). In this procedure, the enzymes were co-crystallized with a concentration of detergents corresponding to their critical micelle concentration (CMC). Phase separation and precipitation were common observations in these crystal trays, likely due to the fact that the detergents were at their CMCs. Crystals were only obtained with NOS for Ag85A-S126A (Figure 3-7-C). The well solution contained 1.0 M ammonium sulfate, 0.1 M HEPES pH 7.0 and 0.5 % w/v PEG 8000. These crystals appeared to be plates and the edges do not appear to be well defined. The two mutants were then co-crystallized with 1 to 2-fold excess of the different detergents and new index screenings were set up. Again, plate type crystals were obtained for

Ag85A-S126A with a 2-fold molar excess of NOS with condition 35 (Figure 3-7-D). These crystals were subjected to X-ray diffraction studies at the APS but only 2-dimensional diffraction was obtained. Attempts to optimize these crystals with the help of additives are on going.

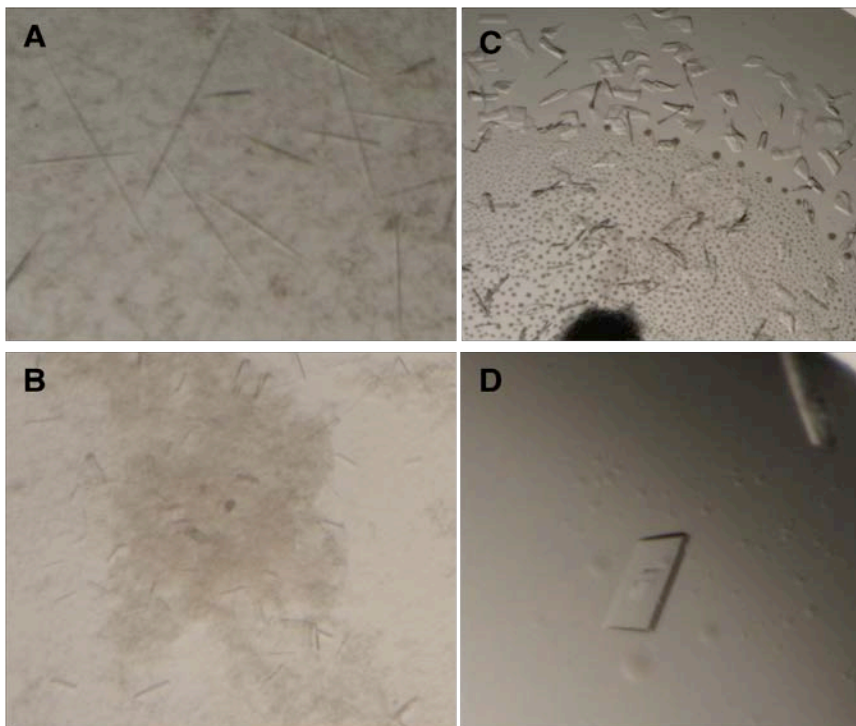


Figure 3-7: Ag85A-S126A and Ag85B-S126A crystals. A) Ag85B-S126A, cond. 51. B) Ag85B-S126A crystals in presence of DDAO, cond. 51. C) Ag85A-S126A crystals in presence of NOS (CMC), cond. 35. D) Ag85A-S126A crystals in presence of 2X NOS, cond. 35.

3.4 Conclusion and future work

In summary, all the structures described confirm the inhibition mechanism of the Ag85 complex by ebselen. The cysteine C209, in spite of not taking part in the catalytic reaction carried out by Ag85C, is of considerable structural importance. The position of

C209, as well the interactions it makes with neighbouring atoms, orders the active site structure in a conformation that allows for catalysis to take place. Any modification or mutation of C209 leads to either a dramatic decrease or complete loss of enzymatic activity, which indicates a low probability of developing drug resistance to a drug modifying the cysteine. For example, if the organism would mutate one of the Ag85 enzymes to generate resistance to a drug functioning similarly to ebselen, the mutant would likely display low level of activity while the two other enzymes would still be inhibited. The same would still be true if two enzymes would undergo mutation with the third one being inhibited.

All of the triad mutants show that disrupting a single hydrogen bond in the catalytic triad promotes relaxation of helix $\alpha 9$ and the consistent structure of the lowest energy conformation for the protein. This suggests that the dynamics exhibited by this helix maybe central to its enzymatic function. The native form allows transfer to trehalose of TMM to make TDM. The relaxed form has an altered carbohydrate-binding site that may promote mycolyl transfer to the terminal arabinosyl moieties of the mAGP.

In summary, these results support a developmental strategy for inhibiting the Ag85 complex with mechanism-based inhibitors that covalently modify the conserved cysteine of these enzymes and will minimize the probability of selecting for drug resistant mutants.

Work is on going to crystallize Ag85A and B mutants to show that similar structural changes are observed when a catalytic triad residue is mutated. Preliminary crystals have been obtained for both enzymes.

Chapter 4

Citrate synthase

4.1 Background

4.1.1 Tricarboxylic acid cycle

The tricarboxylic acid (TCA) cycle, also known as the citric acid cycle or Krebs cycle, includes a sequence of chemical reactions that converts the acetyl moiety of Acetyl-CoA (AcCoA) into carbon dioxide (CO₂) and in doing so makes nicotinamide adenine dinucleotide (NADH) that is later used in the electron transport chain to drive oxidative phosphorylation to make ATP¹²⁸. In addition to its essential role in providing cellular energy, the TCA cycle provides precursors for amino acids, lipids, and other essential macromolecules as well as other important metabolites. Hans Adolf Krebs received the Nobel Prize in Physiology or Medicine in 1953 for the discovery of this cycle¹²⁹.

The TCA cycle is composed of eight steps, and thus involves eight enzymes¹²⁸. A scheme of the TCA cycle is represented in figure 4-1. In eukaryotes, all the reactions take place in mitochondria while in bacteria, the TCA cycle occurs in the cytosol.

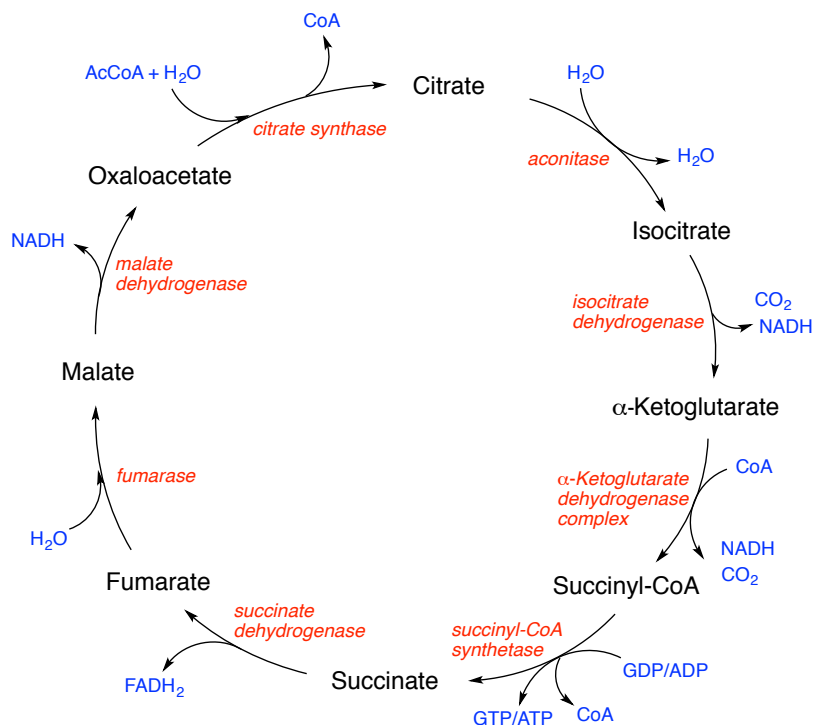


Figure 4-1: Scheme of TCA cycle. Adapted from Nelson and Cox, Lehninger Principles of Biochemistry, 6th Edition, 2013.

Briefly, AcCoA and oxaloacetate are first converted to citrate and CoA by citrate synthase¹²⁸. This step will be further described in the following section. Then, citrate is converted into isocitrate through a dehydration/rehydration reaction catalyzed by an enzyme called aconitase. Isocitrate is dehydrogenated and decarboxylated into α-ketoglutarate. This molecule is converted to succinyl-CoA - after the loss of a second carboxylic group - and then to succinate. Finally, three other enzymes intervene to convert succinate into oxaloacetate through the formation of fumarate, followed by malate. The produced oxaloacetate is ready to be utilized again in the TCA cycle to react with AcCoA.

4.1.2 Role of citrate synthase

Citrate synthase is the first enzyme involved in the TCA cycle. This enzyme catalyzes the conversion of AcCoA and oxaloacetate into citrate and free CoA (Figure 4-2). Numerous research articles have been published on the enzyme citrate synthase. Crystal structures of citrate synthase from various organisms have been solved over the years¹³⁰⁻¹⁴⁰.

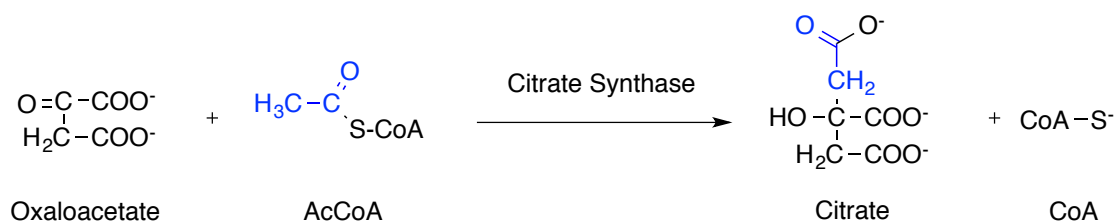


Figure 4-2: Reaction catalyzed by citrate synthase. The two carbons highlighted in blue in the citrate molecule are the ones donated by AcCoA.

The citrate synthase enzyme catalyzes an aldol-Claisen condensation (Figure 4-3)^{131, 134}. First, based on site-directed mutagenesis, an aspartate residue (375 in the crystal structure of chicken citrate synthase, PDB 1CSC¹³²) acts as a catalytic base and deprotonates the α carbon of AcCoA¹⁴¹⁻¹⁴³. The enolate intermediate is stabilized by the presence of a histidine residue (274 in the crystal structure of chicken citrate synthase, PDB 1CSC¹³²)¹⁴⁴⁻¹⁴⁶. Then, a nucleophilic attack takes place: the carbanion formed in the previous step attacks the carbonyl carbon present on oxaloacetate. Another histidine residue (320 in the crystal structure of chicken citrate synthase, PDB 1CSC¹³²) also acts as a catalytic acid and donates its proton to the carbonyl¹³¹. Finally, the citroyl-CoA intermediate is hydrolyzed, leading to the formation of citrate and free CoA^{131, 147}.

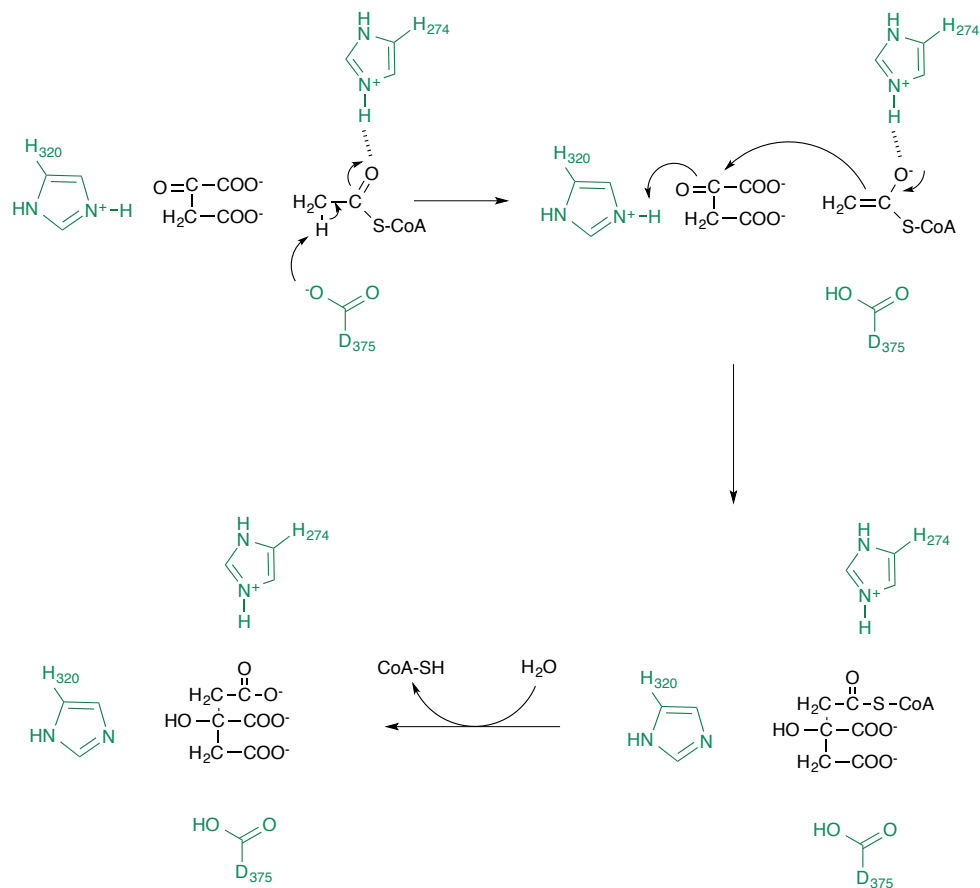


Figure 4-3: Citrate synthase mechanism. Residues participating in the mechanism are highlighted in green.

Kinetic studies are consistent with an ordered bisubstrate mechanism¹⁴⁸. Typically, citrate synthase binds oxaloacetate first and undergoes a conformational change that allows the creation of a binding pocket for the second substrate AcCoA^{130, 149, 150}.

Two different types of citrate synthase have been identified¹³⁸. Type I citrate synthases can be found in most organisms, such as eukaryotes and gram-positive bacteria. The type I enzymes form a dimer and possess a shorter sequence compared to the type II enzymes. Type II citrate synthase are commonly found in Gram-negative bacteria and exhibits an extra N-terminal beta-sheet domain^{136, 138, 151}. The type II enzymes usually

form a hexameric structure. In some cases, the type II enzymes are allosterically inhibited by NADH, allowing regulation of the TCA cycle¹⁵². *E. coli* citrate synthase is an example of the type II group.

4.1.3 Tricarboxylic cycle and citrate synthase in *M. tb*

Many bacteria possess variations in the TCA cycle that respond to their specific needs and metabolic requirements¹⁵³. Indeed, some bacteria utilize variants of the TCA cycle that include oxidative and reductive pathways to favour the formation of biosynthetic precursors. For instance, *E. coli* usually features a traditional TCA cycle. However, under anaerobic conditions, the bacterium utilized a variation that lacks the α -ketoglutarate dehydrogenase^{154, 155}. Thus, the cycle splits into two branches; one is oxidative and terminates with α -ketoglutarate while the second is reductive and generates the formation of succinate. Another example is *Helicobacter pylori*, which uses a variant TCA cycle in an anaerobic environment. Both oxidative and reductive branches are connected by α -ketoglutarate ferredoxin oxidoreductase¹⁵⁶.

Under environmental stresses such as acidic pH or low oxygen availability, many bacteria choose to adopt a latent state in which they stop their growth but maintain metabolic activity¹⁵⁷. *M. tb* reacts to environmental stresses in this way and alters its metabolism^{158, 159}. This phenomenon raises a challenge for treating TB. In fact, most of the TB drugs in clinical use target replicating bacteria¹⁶⁰. In latency, the bacteria become tolerant to those antibiotics that target replicating bacteria making it more difficult to treat TB. Thus, it is critical to gain knowledge about *M. tb* primary metabolism and how the

organism is able to alter its metabolism in order to enter a latent stage and resist antibiotic action. The TCA cycle is an essential part of this metabolism.

Based on the genome sequence, *M. tb* encodes all of the enzymes from the TCA cycle, as well as α -ketoglutarate ferredoxin¹⁶¹. However, until recently, it was believed that *M. tb* lacks α -ketoglutarate dehydrogenase activity^{162, 163}. Instead, α -ketoglutarate is converted to succinic semialdehyde via decarboxylation (α -ketoglutarate decarboxylase); then, succinic semialdehyde is oxidized to produce succinate. Recent studies proved the contrary: the α -ketoglutarate decarboxylase identified by Tian *et al.* also possesses α -ketoglutarate dehydrogenase activities¹⁶⁴. Alternative enzymes that perform this step have also been identified¹⁶⁵⁻¹⁶⁷. Other *M. tb* enzymes involved in the TCA cycle, as well as enzymes bypassing some steps in the cycle, have been characterized. Isocitrate dehydrogenase^{168, 169}, isocitrate lyase^{170, 171}, α -ketoglutarate decarboxylase¹⁶⁴ and malate dehydrogenase¹⁷² are such examples. However, based on several studies, *M. tb* does not appear to use the TCA cycle in a similar manner as other bacteria, highlighting the significance to study the different pathways *M. tb* utilizes for carbon metabolism^{167, 169, 173}. De Carvalho *et al* demonstrated that *M. tb* is able to catabolize several carbon sources simultaneously to maximize bacterial growth¹⁷³.

M. tb citrate synthase has been mentioned in one study by Sasseti and co-workers¹⁷⁴. This enzyme is a 40 kDa protein encoded by *citA* (Rv0889c). Bioinformatic analysis predicts that citrate synthase is a type II enzyme. Sasseti and co-workers demonstrated that several growth-limiting stresses cause the bacteria to favor the carbon fluxes toward triglyceride synthesis (storage) instead of the TCA cycle¹⁷⁴. Additionally, overexpression of the *citA* gene increased the sensitivity of *M. tb* to antibiotics.

Nonetheless, little is known about *M. tb* citrate synthase. The aim of this research was to gain more knowledge about this enzyme. To do so, the crystal structure of *M. tb* citrate synthase in complex with oxaloacetate was solved to 2.1 Å resolution. Additionally, an absorbance-based assay was developed to kinetically characterize the enzyme. This assay could be used to identify potential inhibitors of *M. tb* citrate synthase. Since it is necessary to extend our knowledge about the *M. tb* primary metabolism and the importance of this metabolism for latency and antibiotics tolerance, inhibiting the enzyme activity could be used as a tool to study the metabolism of *M. tb*. In fact, we could inactivate the TCA cycle to study the other pathway(s) that the organism utilizes to promote carbon metabolism.

4.2 Experimental procedures

4.2.1 Cloning of *citA*

The *citA* gene was amplified from H37Rv genomic DNA by PCR using the first two primers shown in table 4-1 (Integrated DNA Technology). The gene was amplified a second time using this PCR product obtained and the second pair of primers displayed in table 4-1. The second pair of primers includes the sequences corresponding to the restriction endonucleases recognition sites. The latter primers were not used directly because of a lack of specificity; indeed, the wrong product was amplified from H37Rv genomic DNA when these primers were used.

Table 4-1: Primers used for the amplification of *citA* gene

citA-5'	GTCCCGGAGAATTTTCGTCCCGGCCTCGAC
citA-3'	TGGTGAGTACCCGCTCCCAGCCGTCGAC
citA-NdeI	CACCTTCATATGACAGTGGTCCCGGAGAATTTTCGTC
citA-BamHI	TTGGATCCTCAATGATGATGATGATGATGGGCGGTGGTGAGTACCCGCT

The gene was then ligated into a pET32-based plasmid (EMD biosciences) between the restriction sites *NdeI* and *BamHI*, including a non-cleavable C-terminal poly-histidine tag. Nucleotide sequencing was performed by Eurofins MWG Operon to confirm the gene sequence (Figure 4-4).

A

VIRT7463 sp P9WPD3 CISY2_MYCTU	<u>MTVVPENFVPLDGVVAFTEIAEPDKDGGALRYRGVDIEDLVSRQVTFG</u> <u>MTVVPENFVPLDGVVAFTEIAEPDKDGGALRYRGVDIEDLVSRQVTFG</u> *****
VIRT7463 sp P9WPD3 CISY2_MYCTU	<u>DVWALLVDGNFGSGLPPAEFFPLPIHSGDVRVDVOAGLAMLAPIWGYAPL</u> <u>DVWALLVDGNFGSGLPPAEFFPLPIHSGDVRVDVOAGLAMLAPIWGYAPL</u> *****
VIRT7463 sp P9WPD3 CISY2_MYCTU	<u>LDIDDATAROQLARASVMALSYVAQSARGIYQPAVQRIIDECSTVTARF</u> <u>LDIDDATAROQLARASVMALSYVAQSARGIYQPAVQRIIDECSTVTARF</u> *****
VIRT7463 sp P9WPD3 CISY2_MYCTU	<u>MTRWQGEPPRHIEAIDAYWVSAAEHGMNASTFTARVIASGTADVAALAS</u> <u>MTRWQGEPPRHIEAIDAYWVSAAEHGMNASTFTARVIASGTADVAALAS</u> *****
VIRT7463 sp P9WPD3 CISY2_MYCTU	<u>GAI GAMSGLHGGAPARVLPMLDEVERAGDARSVVKILDRGEKLMGF GH</u> <u>GAI GAMSGLHGGAPARVLPMLDEVERAGDARSVVKILDRGEKLMGF GH</u> *****
VIRT7463 sp P9WPD3 CISY2_MYCTU	<u>RVYRAEDPRARVLRAAAERLGAPRYEVAVAVEQAALSELRRERPDRAIET</u> <u>RVYRAEDPRARVLRAAAERLGAPRYEVAVAVEQAALSELRRERPDRAIET</u> *****
VIRT7463 sp P9WPD3 CISY2_MYCTU	<u>NVEFWAA-----</u> <u>NVEFWAAVVLDFARVPANMPAMFTCGRTAGWCAHILEOKRLGKLV RPSA</u> *****

B

VIRT874 sp P9WPD3 CISY2_MYCTU	<u>MTVVPENFVPLDGVVAFTEIAEPDKDGGALRYRGVDIEDLVSRQVTFG</u> -----
VIRT874 sp P9WPD3 CISY2_MYCTU	-----MRRC <u>DVWALLVDGNFGSGLPPAEFFPLPIHSGDVRVDVOAGLAMLAPIWGYAPL</u>
VIRT874 sp P9WPD3 CISY2_MYCTU	<u>STSTTPPAHSWARASVMALSYVAQSARGIYQPAVQRIIDECSTVTARF</u> <u>LDIDDATAROQLARASVMALSYVAQSARGIYQPAVQRIIDECSTVTARF</u> ... :. *****
VIRT874 sp P9WPD3 CISY2_MYCTU	<u>MTRWQGEPPRHIEAIDAYWVSAAEHGMNASTFTARVIASGTADVAALAS</u> <u>MTRWQGEPPRHIEAIDAYWVSAAEHGMNASTFTARVIASGTADVAALAS</u> *****
VIRT874 sp P9WPD3 CISY2_MYCTU	<u>GAI GAMSGLHGGAPARVLPMLDEVERAGDARSVVKILDRGEKLMGF GH</u> <u>GAI GAMSGLHGGAPARVLPMLDEVERAGDARSVVKILDRGEKLMGF GH</u> *****
VIRT874 sp P9WPD3 CISY2_MYCTU	<u>RVYRAEDPRARVLRAAAERLGAPRYEVAVAVEQAALSELRRERPDRAIET</u> <u>RVYRAEDPRARVLRAAAERLGAPRYEVAVAVEQAALSELRRERPDRAIET</u> *****
VIRT874 sp P9WPD3 CISY2_MYCTU	<u>NVEFWAAVVLDFARVPANMPAMFTCGRTAGWCAHILEOKRLGKLV RPSA</u> <u>NVEFWAAVVLDFARVPANMPAMFTCGRTAGWCAHILEOKRLGKLV RPSA</u> *****
VIRT874 sp P9WPD3 CISY2_MYCTU	<u>IYVGGPGRSPESVDGWERVLT T A H H H H H H H</u> <u>IYVGGPGRSPESVDGWERVLT T A -----</u> *****

Figure 4-4: Sequencing results of pET32-*citA*. A) N-terminus sequence of pET32-*citA*. B) C-terminus sequence of pET32-*citA*. The construct includes a non-cleavable C-terminal poly-histidine tag.

4.2.2 Purification of citrate synthase

The purified plasmid containing *citA* was used to transform BL21 *E. coli* cells (New England BioLabs®). Bacterial cells were cultured in Luria Broth (Research Products International) at 37 °C in presence of 100 mg/L of ampicillin (Gold Biotechnology). Once an OD_{600 nm} of 0.6 was reached, the cells were induced at 16 °C for 36 to 48 hours by the addition of 1 mM IPTG (Gold Biotechnology). The cells were then harvested by centrifugation and resuspended in a buffer containing 20 mM Tris pH 8.0, 5 mM imidazole, 0.2 M sodium chloride (NaCl) and 5 mM β-Me. The induced stock was stored at -80 °C until needed.

The induced cells were thawed at room temperature. Then, the cells were lysed using 1 mM of lysozyme (Hampton Research) and 0.1 mM of DNaseI (Roche), as well as a sonication step (Sonicator 3000, Misonix). The crude lysate was pelleted by centrifugation at 11,000 rpm (fixed-angle rotor, 5810-R Centrifuge, Eppendorf) for 30 minutes. The supernatant was filtered and then loaded onto a 5 mL HisTrap™ TALON® crude column prepacked with TALON Superflow™ (GE Healthcare). The column was washed with 15 column volumes of resuspension buffer and was eluted using a linear gradient over 15 column volumes with a concentration of imidazole from 5 mM to 150 mM (Figure 4-5).

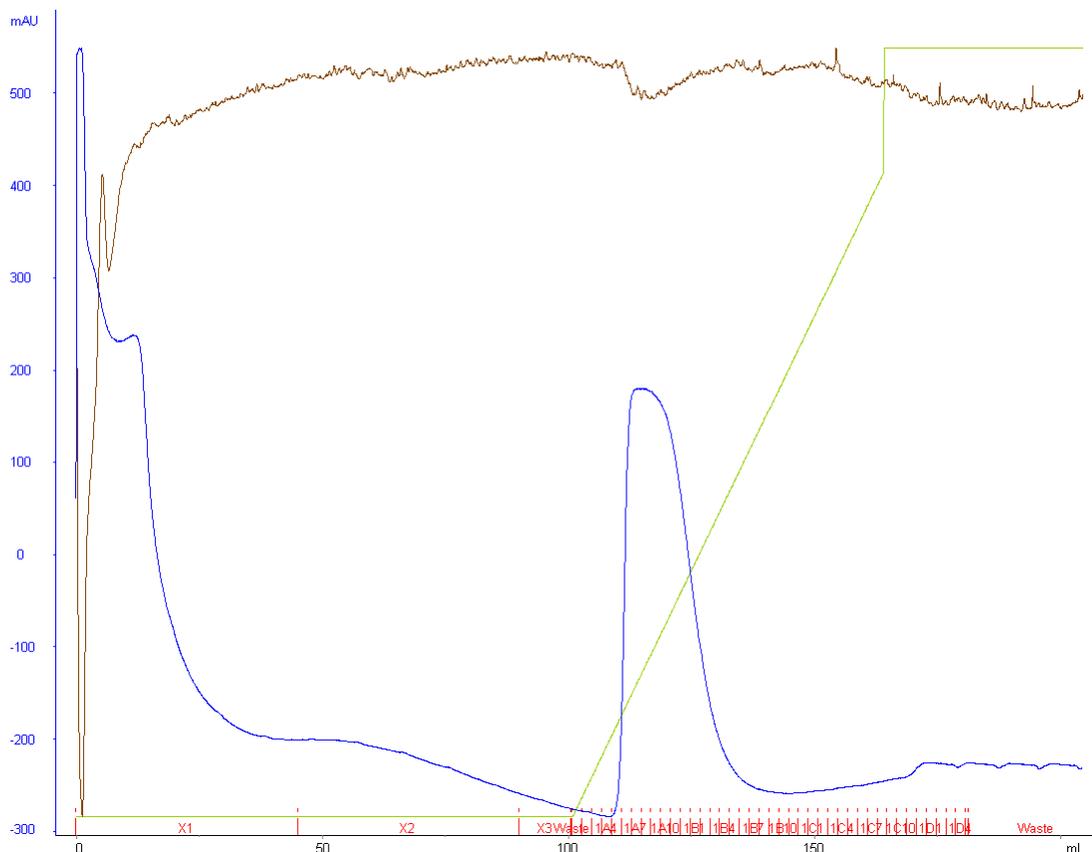


Figure 4-5: Chromatogram from cobalt affinity purification of citrate synthase. The blue line corresponds to the absorbance monitored at 280 nm while the green line represents the concentration of buffer B (higher concentration in imidazole). The brown line corresponds to the conductivity measured.

Citrate synthase was concentrated using ammonium sulfate precipitation at a final concentration of 2.8 M. The pelleted protein was resuspended in a buffer containing 50 mM Tris pH 8.0 and 0.3 mM TCEP. The sample was further purified using size exclusion chromatography (Figure 4-6). The fractions containing citrate synthase were pooled together and a new ammonium sulfate precipitation was carried out. The pelleted protein was resuspended into crystallization buffer (50 mM Tris pH 8.0, 0.3 mM TCEP) and dialyzed overnight against the same buffer.

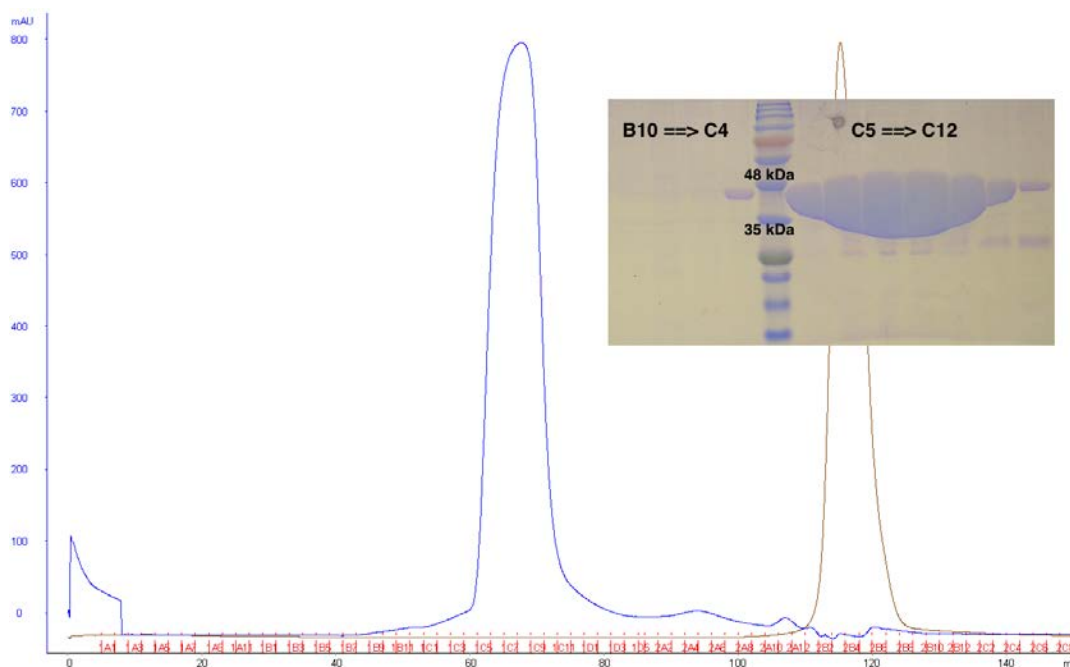


Figure 4-6: Chromatogram and SDS-PAGE gel from size exclusion chromatography of citrate synthase. The blue line corresponds to the absorbance monitored at 280 nm while the brown line corresponds to the conductivity measured. The elution volume from the S200 column suggests that citrate synthase is a tetramer or larger.

The concentration of the citrate synthase was determined using absorbance spectroscopy at a wavelength of 280 nm using the theoretical extinction coefficient ($50420 \text{ M}^{-1} \text{ cm}^{-1}$) determined by the ProtParam function from the ExPASy proteomics server⁹¹.

4.2.3 Preparation of a selenomethionine protein

The selenomethionine kit was purchased from Molecular Dimensions and the SelenoMet™ medium prepared per the kit instructions. Briefly, 10.8 g of SelenoMet™ medium was dissolved into 500 mL of deionised water. The medium was autoclaved for 20 min at 121 °C. In the mean time, 2.55 g of SelenoMet™ Nutrient Mix was dissolved into 25 mL of deionised water. The solution was filter sterilized through a 0.45 µm syringe filter. Then, the nutrient solution was added to the autoclaved SelenoMet™ medium once it was cooled down.

A 5 mL culture of BL21 *E. coli* cells containing the *citA* plasmid was grown overnight. The culture was harvested and the cell pellet was resuspended with several milliliters of the SelenoMet™ medium. The resuspended cell pellet was used to inoculate the sterile SelenoMet™ medium. Bacterial cells were grown at 37 °C in the presence of 100 mg/L of ampicillin (Gold Biotechnology) to an OD_{600nm} of 0.6. Selenomethionine solution (250 X) was added to the cells, which were then incubated for 15 min at 37 °C. The cells were then induced at 16 °C for 36 to 48 hours by addition of 1 mM IPTG (Gold Biotechnology). The cells were then harvested by centrifugation and resuspended into 20 mM Tris pH 8.0, 5 mM imidazole, and 5 mM β-Me.

The protein was purified following the same protocol as the native enzyme. A cobalt affinity purification step, followed by size exclusion chromatography, was performed. The purity was analyzed using SDS-PAGE (Figure 4-7).

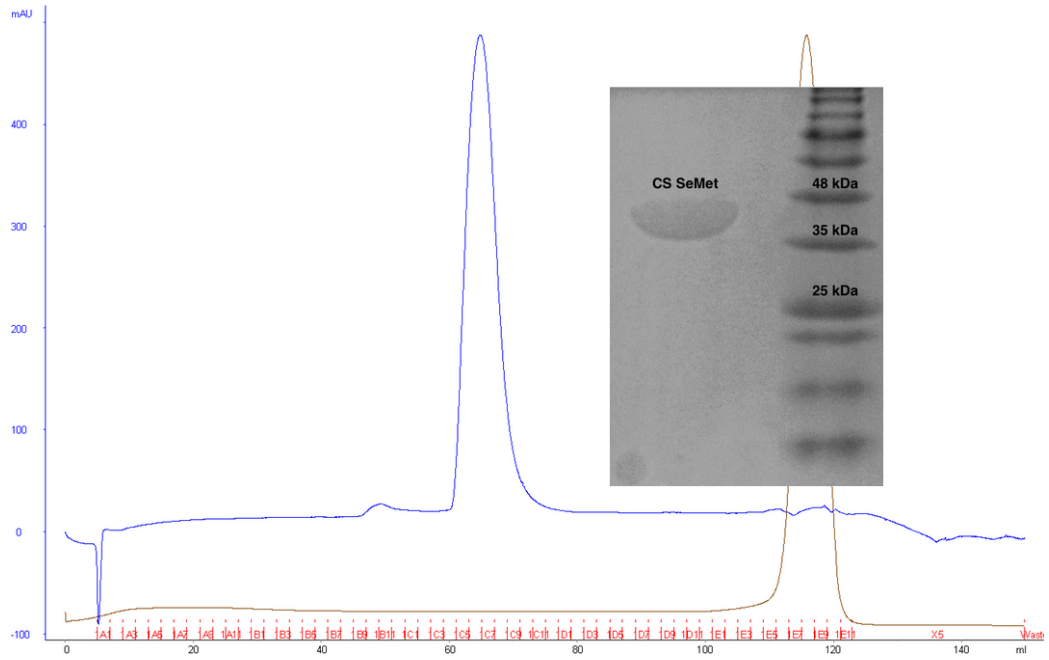


Figure 4-7: Purification of selenomethionine derivatized citrate synthase. Chromatogram and SDS-PAGE gel from size exclusion chromatography. The blue line corresponds to the absorbance monitored at 280 nm while the brown line corresponds to the conductivity measured.

4.2.4 Mass spectrometry

After running a SDS-PAGE containing a sample of purified citrate synthase, the gel slice corresponding to the contaminant band observed at around 30 kDa was excised. In-gel trypsin digestion was performed using sequencing-grade trypsin (Promega) following standard procedures. Peptide mass fingerprinting was carried out on a MALDI-TOF/TOF mass spectrometer (Bruker Daltonics). CHCA (Acros Organics) was used as a matrix. The data were analyzed using the MASCOT server.

4.2.5 Absorbance-based assay

Stock solutions of 5,5'-dithio-*bis*-(2-nitrobenzoic acid) (Sigma Aldrich) and oxaloacetic acid (Sigma Aldrich) were prepared in 50 mM Tris pH 8.0 and stored at -20 °C up to one week prior to use.

AcCoA was purchased from Roche (25 mg). The white solid was dissolved into deionised water to a concentration of 20 mM. The solution of AcCoA was transferred in several aliquots, each of them containing 50 µL of the AcCoA solution. The deionised water was then evaporated from the different aliquots using a SpeedVac™. The aliquots were stored at -20 °C and were stable for several months. Prior to using an aliquot of AcCoA, the sample was thawed at room temperature. Acetic anhydride (4.05 µL) was added to the aliquot and the sample was incubated for 10 min at room temperature. The reaction was quenched using 405 µL of 50 mM Tris pH 8.0. The final concentration of AcCoA was 2.45 mM.

The reactions were carried out at 25 °C on a Synergy H4 Hybrid Reader (BioTek) using 10 nM of citrate synthase. The enzyme was dialyzed against 20 mM Tris pH 8.0 prior to use. Each of the reactions was performed in 50 mM Tris pH 8.0. To determine the kinetic parameters, either the concentration of oxaloacetate was fixed at 250 µM while the AcCoA concentration was varied from 0 to 500 µM or the concentration of AcCoA was fixed at 200 µM whereas the oxaloacetate concentration was varied between 0 and 250 µM. The 5,5'-dithio-*bis*-(2-nitrobenzoic acid) was fixed at 300 or 600 µM and the concentration of citrate synthase was 10 nM. The reactions were performed in quadruplicate. Non-linear regression analysis was carried out using Prism 5 software.

The Z' value was determined by performing 48 reactions, 24 positive controls containing citrate synthase and 24 negative controls lacking enzyme. Each of the reactions contained 100 μM of oxaloacetate, 100 μM AcCoA, 10 nM citrate synthase and 300 μM 5,5'-dithio-*bis*-(2-nitrobenzoic acid).

NADH was purchased from Research Products International Corp. The inhibition of citrate synthase by NADH was tested using similar conditions to the ones used for Z' determination. NADH concentration was varied from 0 to 10 mM.

4.2.6 Crystallization studies

Each of the crystals was grown using the hanging-drop vapor diffusion method. Index screens (Hampton Research) were set up using different concentrations of citrate synthase, as well as different ligands (products, substrates or substrate/product). Once a preliminary hit was obtained, further optimization was attempted using either 1 or 2-dimensional screens, or detergent /additive screens (Hampton Research).

Preliminary crystals were obtained for a complex including 9.5 mg/mL citrate synthase, 5 mM oxaloacetate and 5 mM CoA (Chem-Impex International Inc). The complex was crystallized in 0.1 M Tris pH 8.5, 0.5 M NaCl and 22 % w/v PEG 3350.

The selenomethionine derivatized citrate synthase (14.4 mg/mL) was incubated with 5 mM oxaloacetate and 5 mM CoA for 30 min on ice. The complex crystallized against a well solution containing 0.1 M Tris pH 8.5, 0.5 M NaCl and 19 % w/v PEG 3350 in the presence of 5.6 mM of a detergent, CYMAL-6 (6-cyclohexyl- β -D-maltoside). PEG 3350 was added prior to mounting the crystal for data collection.

Citrate synthase (30.8 mg/mL) was also crystallized in presence of 6.5 mM NADH. The well solution contained 0.02 M magnesium chloride (MgCl₂), 0.1 M HEPES pH 7.5, and 22 % w/v poly(acrylic acid sodium salt) 5100 and the crystals were grown in presence 0.1 M barium chloride, as part of the additive screen (Hampton Research).

All crystals were flash-cooled in liquid nitrogen before data collection. Diffraction data were collected at the LS-CAT beamline at the Advance Photon Source Argonne National Laboratory (APS-ANL, IL).

4.2.7 Single-wavelength anomalous dispersion experiment

A single diffraction data set was collected at a wavelength of 0.97856 Å for a crystal of selenomethionine derivatized citrate synthase crystallized in presence of oxaloacetate and CoA. HKL2000 was utilized to index, integrate and scaled as an anomalous data⁹². The Autosol and Autobuild tools from PHENIX were used to build a model for the citrate synthase⁹⁵. Forty-four selenium sites were identified, leading to the determination of 4 copies of citrate synthase in one asymmetric unit since *M. tb* citrate synthase possesses eleven methionine residues. The solution obtained provided a figure of merit of 0.347; the model correlation coefficient was 0.87. Then, the PHENIX refine tool was used to carry out rigid body refinement, simulated annealing, positional and B-factor refinements⁹⁵ while manual corrections of the model were performed using COOT⁹⁶.

4.3 Results and Discussion

4.3.1 Identification of a contaminant using mass spectrometry

During the purification of citrate synthase, a contaminant band at around 30 kDa was always observed on SDS-PAGE gel (Figure 4-8). Diverse purifications were attempted in order to remove this impurity: longer wash with binding buffer during cobalt affinity chromatography, anion exchange, ammonium sulfate precipitation with different concentrations of salt and size exclusion chromatography are examples of such attempts. The contaminant was still present. However, the contaminant was partially removed by using size exclusion chromatography.

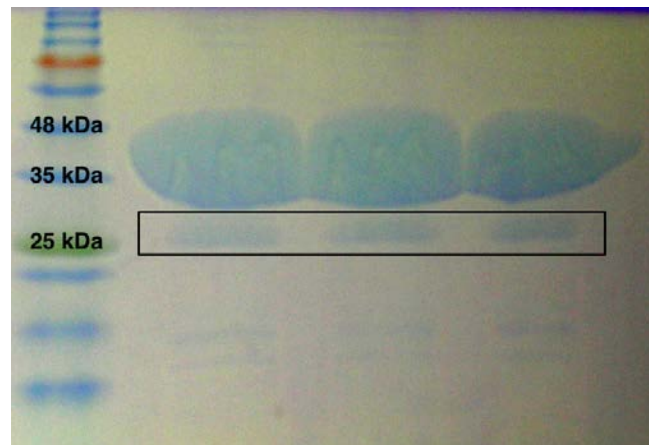


Figure 4-8: SDS-PAGE gel of citrate synthase (41 kDa, poly-histidine tag included) after purification. The black box highlights the contaminant band observed at 30 kDa which was excised from the gel and subjected to mass peptide fingerprinting.

Mass spectrometry was utilized in order to identify the contaminant. The corresponding gel slice was excised and in-gel trypsin digestion was carried out. A MASCOT search provided a score of 68 (significant score was 49) and identified *M. tb*

citrate synthase as the contaminant. 48 % of the protein sequence was covered. However, in observing the different peptides, it appears that a portion of the N-terminus of the protein is absent (Figure 4-9). Thus, the band observed at around 30 kDa corresponds to a truncation of *M. tb* citrate synthase that is lacking its N-terminus. As the poly-histidine tag is located at the C-terminus of the protein, it explains why the truncated protein is still able to bind to a cobalt affinity column.

```

1 - MTVVPENFVP GLDGVVAFTT EIAEPDKDGG ALRYRGVDIE DLVSQRVTFG DVWALLVDGN
61 - FGSLPPAEP FPLPIHSGDV RVDVQAGLAM LAPIWGYAPL LDIDDATARQ QLARASVMAL
121 - SYVAQSARGI YQPAVPQRII DECSTVTARF MTRWQGEPPD RHIEAIDAYW VSAAEHGMNA
181 - STFTARVIAS TGADVAAALS GAIGAMSGPL HGGAPARVLP MLDEVERAGD ARSVVKGILD
241 - RGEKLMGFH RVYRAEDPRA RVLRAAAERL GAPRYEVAVA VEQAALSELR ERRPDRAIET
301 - NVEFWAAVVL DFARVPANMM PAMFTCGRTA GWCAHILEQK RLGKLVPSA IYVGPGRSP
361 - ESVDGWERVL TTAHHHHHH

```

Figure 4-9: Amino acids sequence of *M. tb* citrate synthase. The peptides highlighted in blue are the ones that were observed when the peptide mass fingerprinting was carried out on the contaminant band. The protein sequence coverage was 48%.

Since the protein undergoes proteolysis, we attempted to induce bacterial cells containing the *citA* plasmid for only one 16 hours instead of 36 hours to avoid proteolysis. Nonetheless, the truncated protein was still observed. We hypothesized that the citrate synthase forms an oligomer (tetramer or hexamer based on the size exclusion chromatogram, Figure 4-6) and that one/several of the monomers is/are truncated.

4.3.2 Development of an absorbance-based assay

4.3.2.1 Kinetic parameters determination

An absorbance-based assay was developed using 5,5'-dithio-*bis*-(2-nitrobenzoic acid), abbreviated as DTNB, which is commonly used to assess the amount of thiol groups in a sample¹⁷⁵. A thiol group acts as a nucleophile and attacks the DTNB compound, cleaving the disulfide bond present in DTNB and generating 3-thio-6-nitrobenzoate (TNB). In an alkaline solution, this leaving group possesses a yellow color and absorbs with a λ_{max} at 412 nm.

The absorbance-based assay utilizes oxaloacetate and AcCoA. In the presence of citrate synthase, the substrates are converted to citrate and CoA. The latter possesses a free thiol group, which can react with DTNB. The release of one CoA molecule corresponds to the formation of one TNB molecule. The absorbance can be monitored at 412 nm. The scheme of this absorbance-based assay is presented in figure 4-10.

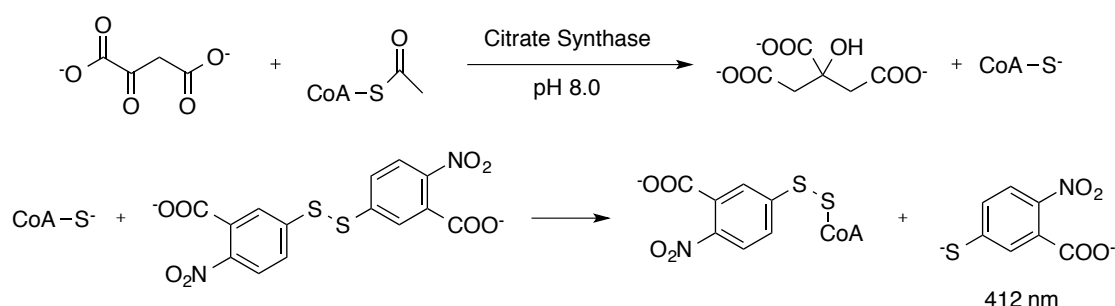


Figure 4-10: Scheme of *M. tb* citrate synthase absorbance-based assay.

The activity of *M. tb* citrate synthase was tested using 160 μM oxaloacetate and 200 μM AcCoA in the presence of 300 μM of DTNB and 10 nM enzyme. The assay was

carried out at pH 8.0 at 25 °C. A control reaction omitting the enzyme was performed in parallel. Because of how AcCoA solutions were stored, the compound is contaminated with a significant amount of CoA. Thus, an aliquot of AcCoA was “recovered” prior to be utilized as described in section 4.2.5. The procedure used was described by Trievel and co-workers¹⁷⁶.

In the presence of citrate synthase, an increase of the absorbance increase at 412 nm is readily observed, indicating that the enzyme is active and converts the substrates to citrate and free CoA (Figure 4-11). Additionally, the background for this assay is very low; no reaction is observed when only AcCoA and oxaloacetate are present.

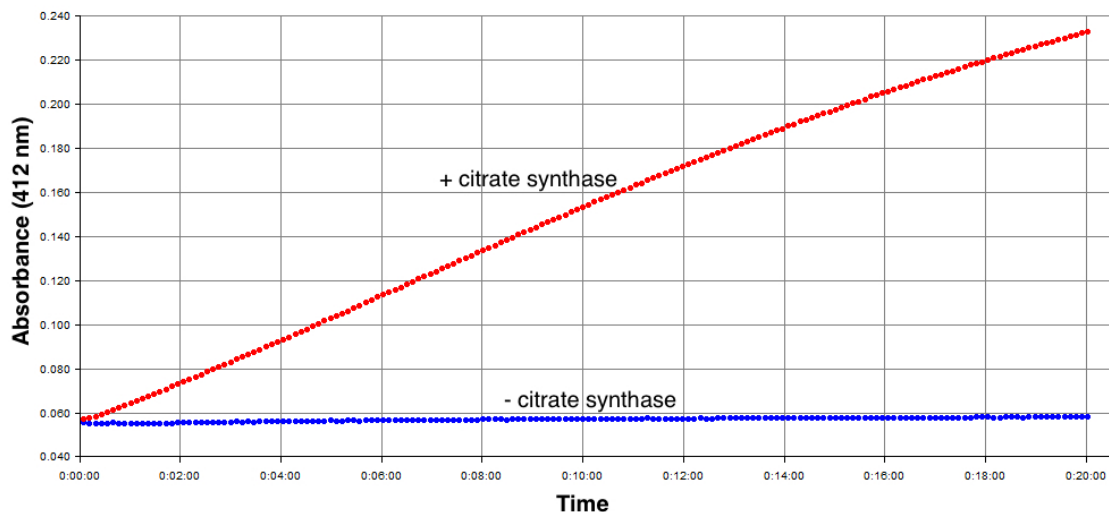


Figure 4-11: Enzymatic activity test of *M. tb* citrate synthase. The absorbance was monitored at 412 nm. Both reactions contain oxaloacetate and AcCoA. The reaction colored in blue is a control lacking citrate synthase while the reaction represented in red contains citrate synthase.

Since the enzymatic activity of citrate synthase was confirmed, the next step was to determine the steady-state kinetic parameters. To do so, either the concentration of AcCoA was fixed and the oxaloacetate concentrations were varied or the contrary was performed. The slopes (Abs/min) corresponding to the different concentrations of substrate allow the determination of the initial velocities when using the Beer-Lambert law and the molar extinction coefficient of TNB ($14,150 \text{ M}^{-1} \text{ cm}^{-1}$)^{177, 178}.

First, a two-dimensional grid was attempted. A range of oxaloacetate concentrations from 0 μM to 250 μM was used while AcCoA was varied from 25 μM to 200 μM . DTNB was used at a concentration of 300 μM . Lineweaver-Burk plots were represented graphically to determine the kinetic parameters K_m and V_{\max} . However, the double-reciprocal plot was inconclusive; intersecting lines should represent the formation of a ternary complex, but the lines were not all intersecting in our assay. The different K_m values were calculated using non-linear regression analysis on Prism 5 software (equation 4-1). The initial velocity ($\mu\text{M}/\text{min}$) was plotted versus the concentration of oxaloacetate (Figure 4-12).

$$V = \frac{V_{\max} \times [S]}{K_m + [S]} \quad (\text{Equation 4-1})$$

V represents the initial velocity while V_{\max} corresponds to the maximal velocity theoretically reached by the enzyme. $[S]$ is the concentration of the substrate. K_m is the Michaelis-Menten constant.

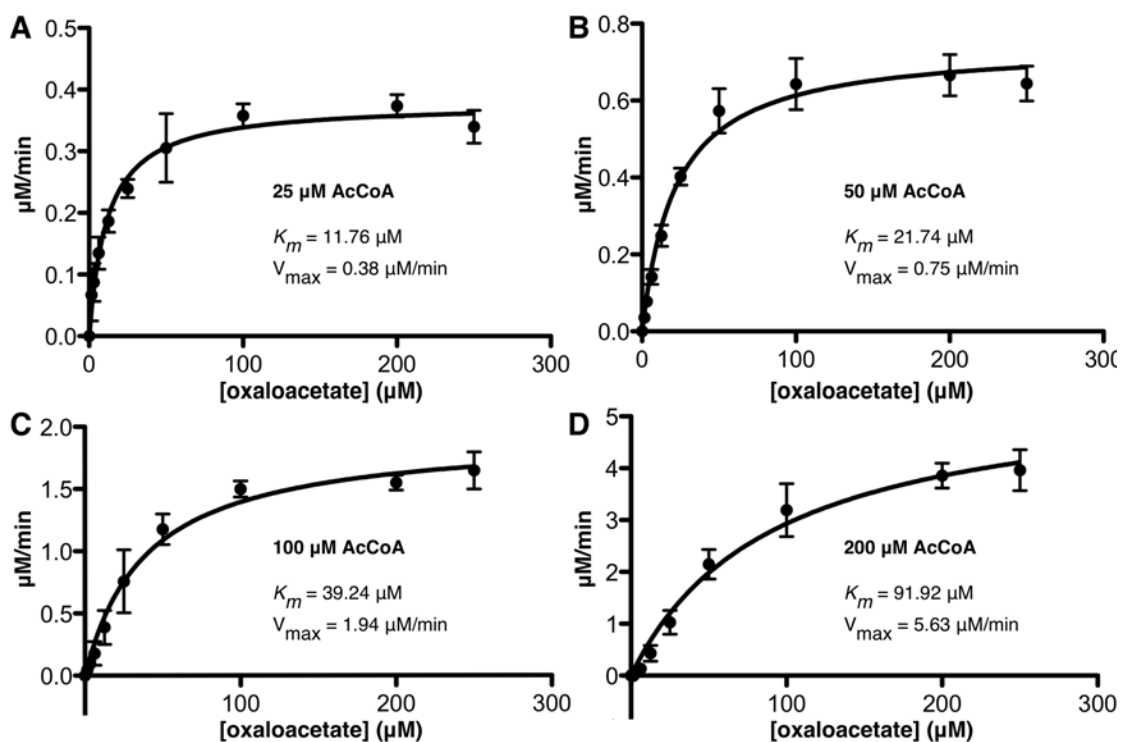


Figure 4-12: Michaelis-Menten curves for oxaloacetate. The oxaloacetate concentration was varied from 0 to 250 μM while the concentration of AcCoA was fixed at 25 μM (A), 50 μM (B), 100 μM (C) or 200 μM (D). The error bars (standard deviations) were calculated from triplicate reactions.

At a saturating concentration of 200 μM of AcCoA, the apparent Michaelis-Menten K_m value for oxaloacetate was found to be 91.92 μM . The K_m value for AcCoA was then determined using a fixed concentration of oxaloacetate (200 μM) and a range of AcCoA concentrations from 0 to 500 μM . DTNB was used at a concentration of 600 μM .

When performing this experiment, substrate inhibition was observed. Indeed, it is documented in literature that citrate synthase can be inhibited by its own substrate AcCoA^{179, 180}. In this case, the substrate binds as a competitive inhibitor in the active site to promote inhibition. When plotting a Michaelis-Menten curve for AcCoA, the initial

velocity rises to a maximum, and then suddenly decreases as the AcCoA concentration is increased (Figure 4-13).

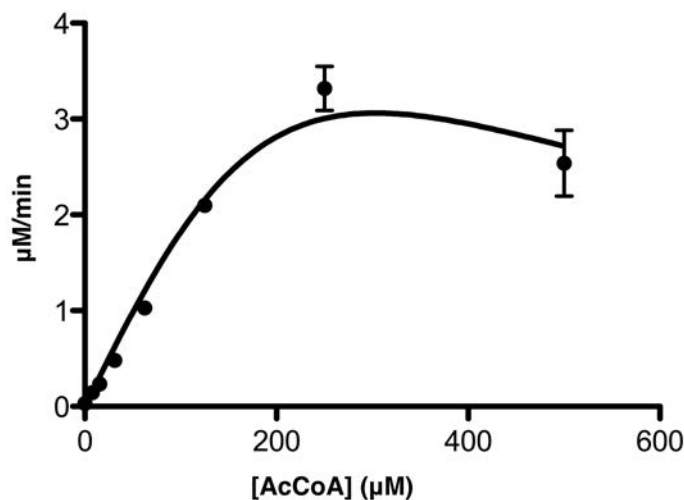


Figure 4-13: Michaelis-Menten curve for AcCoA. AcCoA concentration was varied from 0 to 500 μM . The error bars (standard deviations) were calculated from triplicate reactions.

In order to calculate the K_m and the K_i (inhibition constant) values, the software Prism 5 uses the same equation that can be used for a competitive inhibition. The equation is displayed as equation 4-2. V , V_{max} , $[S]$, K_m and K_i values correspond to the values previously described.

$$V = \frac{V_{\max} \times [S]}{K_m + [S] \times \left(1 + \frac{[S]}{K_i}\right)} \quad (\text{Equation 4-2})$$

However, when this equation was applied in Prism 5, the K_m and K_i values could not be accurately determined. The reason is likely that we do not have sufficient data points above 200 μM ; thus the program is unable to fit the data to the substrate inhibition equation. Experiments are ongoing to determine accurate K_m and the K_i values for the substrate AcCoA.

4.3.2.2 Z' value determination

Upon the determination of reasonable values for the kinetic parameters, experiments were performed to determine a Z' value for this assay. A Z'-factor is a statistical parameter used in the validation of assays for high-throughput screening purposes; it describes the signal-to-background ratio⁸⁹. This factor is calculated using equation 4-3 giving a value between 0 and 1; a value closer to 1 indicates an assay with higher signal-to-noise and better precision. If the value is below 0.5, it indicates that optimization of the assay is required before pursuing screening. An assay is usually considered suitable for high-throughput screening when the Z' value is above 0.5.

$$Z' = 1 - \frac{3\sigma_{c+} + 3\sigma_{c-}}{|\mu_{c+} - \mu_{c-}|} \quad (\text{Equation 4-3})$$

The terms σ_{c+} and σ_{c-} correspond to the standard deviation values of positive controls and negative controls, respectively; while the terms μ_{c+} and μ_{c-} represent the mean of positive controls and negative controls, respectively.

A set of 48 reactions was performed using the absorbance-based assay described in section 4.3.2.1. The experiment includes 24 negative controls that lack citrate synthase and 24 positive controls that contain enzyme. Each of the reactions were carried out using near K_m values for both substrates; oxaloacetate was used at 100 μM while the apparent K_m value for AcCoA was estimated to be 100 μM based on the Michaelis-Menten curve described in section 4.3.2.1. DTNB was used at a concentration of 300 μM and the citrate synthase concentration was 10 nM. The Z' -factor was calculated to be 0.72.

Work continues to determine again the Z' -factor using 1 % DMSO in the reaction, because the drugs from the NIH Clinical Collection and other compound libraries are stored in DMSO. Thus, it is necessary to determine whether or not the enzyme activity is affected by the presence of DMSO prior to screening any library for potential inhibitors.

4.3.2.3 Test inhibition of citrate synthase by NADH

Based on bioinformatic analysis, *M. tb* citrate synthase is hypothesized to be a type II enzyme. Since NADH is a known allosteric inhibitor for some type II enzymes, we tested whether or not NADH exhibits such an effect on the activity of citrate synthase. The absorbance-based assay was used. Each of the reactions contained 100 μM oxaloacetate, 100 μM AcCoA, 300 μM DTNB and 10 nM citrate synthase. The concentration of NADH was varied between 0 and 10 mM; however, no inhibition was observed. This result is in agreement with the study by Viollier *et al.*¹⁸¹. They demonstrated that NADH does not inhibit the *Streptomyces coelicolor* citrate synthase enzyme encoded by *citA*, which is another Gram-positive bacteria related to mycobacteria. Indeed, citrate synthase of Gram-negative bacteria such as *E. coli* are the

species typically affected by this allosteric inhibitor¹⁸². Other known allosteric inhibitors of citrate synthase such as ATP/ADP, NAD⁺, isocitrate or α -ketoglutarate will be tested in order to ascertain whether or not they affect the *M. tb* citrate synthase activity.

4.3.3 Determination of citrate synthase structure

4.3.3.1 Citrate synthase in complex with oxaloacetate

To gain more insight about *M. tb* citrate synthase, we crystallized the enzyme to solve its structure. Preliminary crystals of the enzyme were obtained with oxaloacetate and CoA (Figure 4-14). The rod shape crystals were analyzed at the APS and diffraction data was obtained to 2.9 Å resolution. The protein crystallized in a primitive hexagonal space group (unit cells: $a = b = 150.3$ Å, $c = 200.1$ Å, $\alpha = \beta = 90^\circ$, $\gamma = 120^\circ$). Molecular replacement was attempted using various models of type II citrate synthases available in the RCSB Protein Data Bank. Based on sequence alignment, *M. tb* citrate synthase shares approximately 30 % sequence similarity with *Thermus thermophilus* (*T. thermophilus*) citrate synthase (PDB accession code 1IXE). The structure 1IXE was one of the main templates used for molecular replacement but no solution was obtained in any of the related space groups among the primitive hexagonal family. We attempted to index the diffraction data as a lower symmetry space group but once again, no molecular replacement solution was obtained.

Crystals of citrate synthase were obtained with NADH in the crystallization solution (Figure 4-14). These crystals were subjected to X-ray diffraction experiments at the APS before the absorbance-based assay was developed; the lack of inhibition of *M. tb* citrate synthase by NADH was not yet characterized. The enzyme crystallized in a P2₁

space group (unit cell: $a = 75.6 \text{ \AA}$, $b = 121.3 \text{ \AA}$, $c = 100.1 \text{ \AA}$, $\alpha = \gamma = 90^\circ$, $\beta = 95.0^\circ$) to 2.4 \AA . Once again, molecular replacement was inconclusive.

Thus, a selenomethionine derivatized protein was prepared. *M. tb* citrate synthase possesses eleven methionine residues. Crystals of selenomethionine derivatized protein co-crystallized with CoA and oxaloacetate were optimized primarily through utilizing the detergent screen. Most of the crystals analyzed at the APS diffracted poorly. However, one crystal of the complex grown in presence of CYMAL-6 provided data to 2.1 \AA (Figure 4-14). Data were collected at the peak of the selenium K-edge to carry out a SAD experiment. Information about data collection and refinement statistics is displayed in table 4-2.

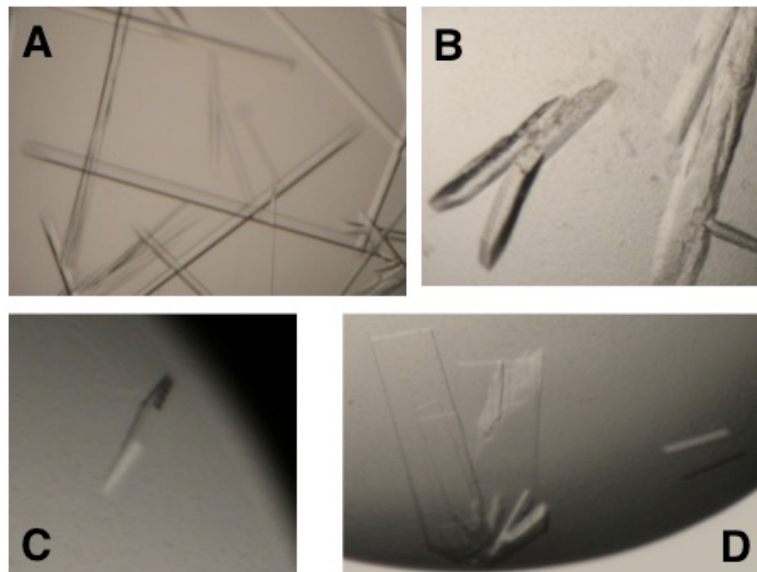


Figure 4-14: Crystals of *M. tb* citrate synthase. A) Citrate synthase in complex with CoA and oxaloacetate. B) Citrate synthase in presence of NADH. C/D) Selenomethionine derivatized citrate synthase in complex with oxaloacetate and CoA.

Table 4-2: Data collection and refinement statistics for selenomethionine derivatized citrate synthase in complex with oxaloacetate and CoA. Refinement of the model is still ongoing.

Data Collection	Citrate SeMet in complex with oxaloacetate and CoA
Space Group	P2 ₁
Unit Cell Dimensions	
<i>a, b, c</i> (Å)	75.7, 130.0, 92.4
α, β, γ (°)	90.0, 107.1, 90.0
Resolution Range (Å)	50.0-2.1
Wavelength (Å)	0.97856
R _{sym} (Highest shell)	12.0 (82.0)
I/σI	21.4 (2.3)
Completeness (%) (Highest shell)	100.0 (100.0)
Redundancy (Highest shell)	7.6 (7.7)
Refinement	
Total Reflections (Unique)	758160 (99459)
R _{work} / R _{free}	20.4/23.7
Wilson B factor	31.7
R.m.s. deviations	
Bond lengths (Å)	0.009
Bond angles (°)	1.132
Ramachandran plot	
Favored (%)	97.07
Outliers (%)	0.34

The final refined crystal structure contains four molecules in the asymmetric unit. Based on the results from size exclusion chromatography and the X-ray crystallographic model, it is clear that the functional biological unit of *M. tb* citrate synthase is a tetramer. Each monomer possesses 15 α -helices and 4 β -sheets (Figure 4-15). Contrary to what was expected from the mass spectrometry data, electron density was observed for the N-terminus of each monomer, except for a few residues in two of them.

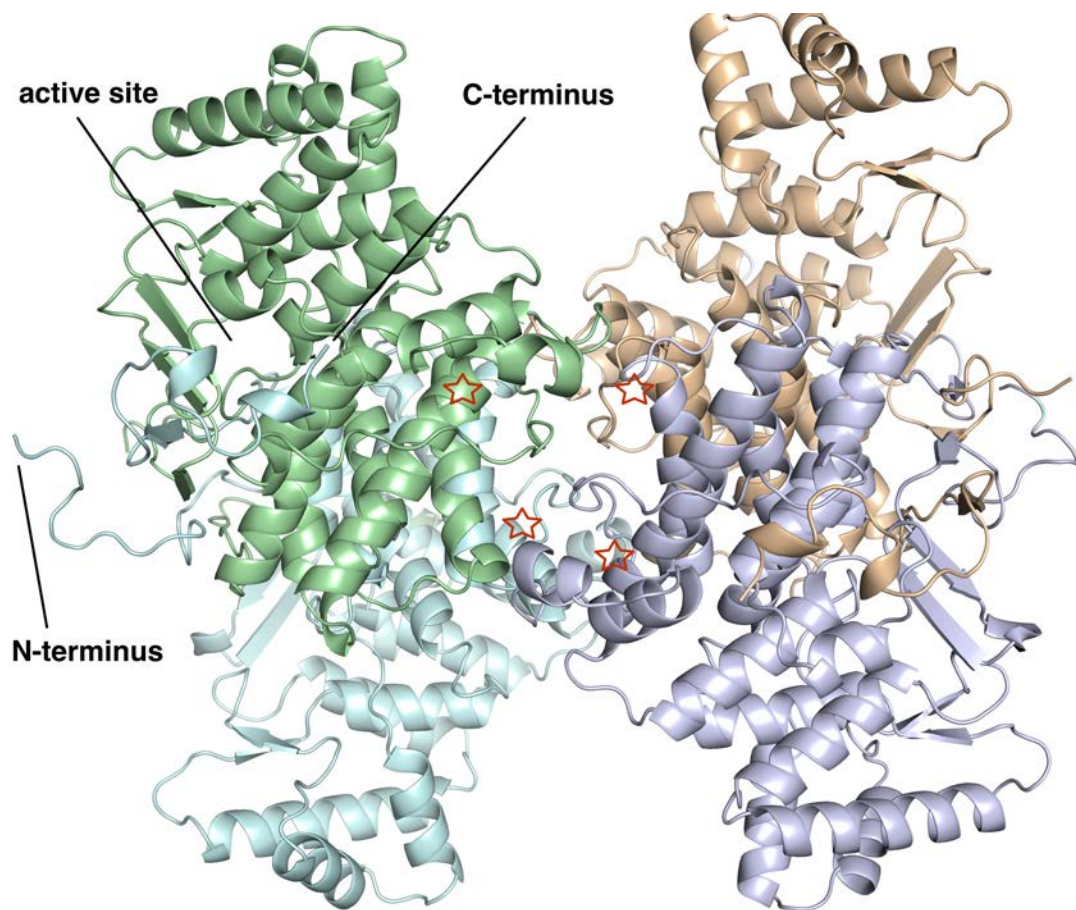


Figure 4-15: Overall structure of selenomethionine derivatized citrate synthase. The enzyme forms a tetramer. The positions of the N-terminus and C-terminus are indicated, as well as the location of the active site. The red star highlights the position of an unknown electron density that will be discussed further in this section.

The fold is similar to that of *T. thermophilus* citrate synthase (low RMS displacement of 4.02 Å when superimposing the C α atoms) but differences between the two structures illustrate why the attempted molecular replacement failed. Specifically, the interface between two molecules of *T. thermophilus* citrate synthase involves 4 α -helices while only 3 α -helices are interacting between 2 molecules of *M. tb* citrate synthase (Figure 4-16). The fourth α -helix in the *T. thermophilus* citrate synthase structure forms a random coil in the *M. tb* citrate synthase that consists of several proline residues, phenylalanine residues or other hydrophobic residues (Figure 4-17). These four interfacial helices are found in all citrate synthase structures from diverse organisms that are available in the RCSB Protein Data Bank.

No electron density was observed in the active site that can account for oxaloacetate or CoA. However, an unknown electron density is observed in each monomer structure and is located in the center of the tetramer (Figure 4-15). The pocket in which this electron density is found contains two arginine residues (R149 and R153) and a glutamine residue (Q137) that might stabilize a negatively charged molecule. We first hypothesized that the density corresponded to oxaloacetate. However, the electron density does not match perfectly the structure of oxaloacetate. The crystallization condition does not contain any component that could account for this density. We then hypothesized that a component from *E. coli* might have been purified along with the protein. We hypothesized that the density corresponds to pyruvate, a compound typically converted to AcCoA prior entering the TCA cycle. Pyruvate could act as an allosteric regulator of *M. tb* citrate synthase as the location is close to that one where NADH binds in other citrate synthase structure in complex with NADH^{137, 139, 183}. The improvement of

this model of *M. tb* citrate synthase is ongoing, as well as the identification of the unknown electron density.

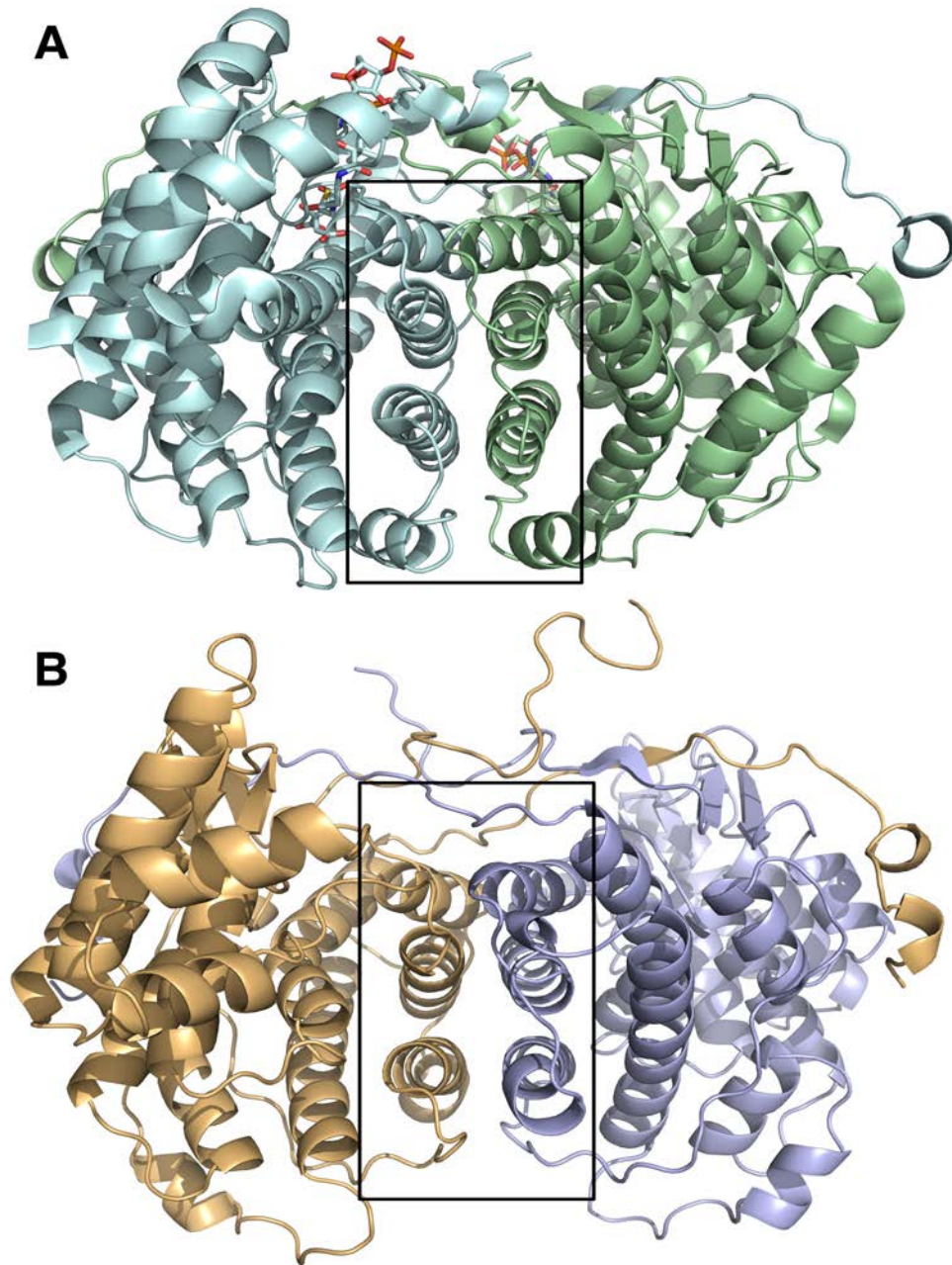


Figure 4-16: Comparison of *T. thermophilus* citrate synthase structure (A) and *M. tb* citrate synthase structure (B). CoA and citrate are represented as sticks in the *T. thermophilus* citrate synthase active site. The black boxes indicate the 4 helices at the interface between two *T. thermophilus* citrate synthase monomers (A) or the 3 helices at the interface between two *M. tb* citrate synthase monomers (B).

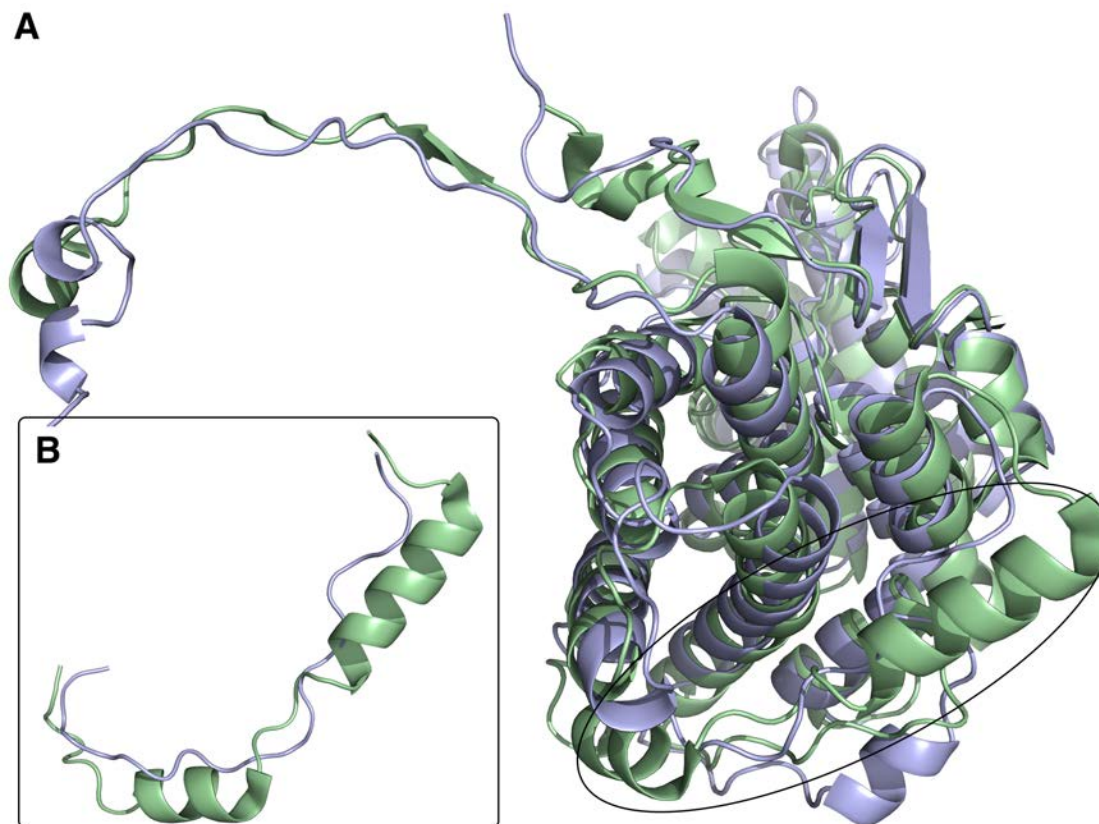


Figure 4-17: Superimposition of *T. thermophilus* citrate synthase monomer (green) and *M. tb* citrate synthase monomer (blue). The black circle highlights the major difference in secondary structures between both structures (A). A close up view of this region is displayed in B (Residues N60-V80 in *M. tb* citrate synthase; residues R54-H90 in *T. thermophilus* citrate synthase).

The structure of *M. tb* citrate synthase crystallized in presence of NADH was solved using the model of the selenomethionine derivatized protein. As it was expected based on the data obtained with the absorbance-based assay, NADH was not present in the structure. NADH is an allosteric inhibitor of citrate synthase type II that generally promotes a conformational change to inactivate the enzyme. Since the structure does not show any evidence of bound NADH, nor does it display any conformational change when compared to the complex with oxaloacetate, this structure suggests that the *M. tb* citrate

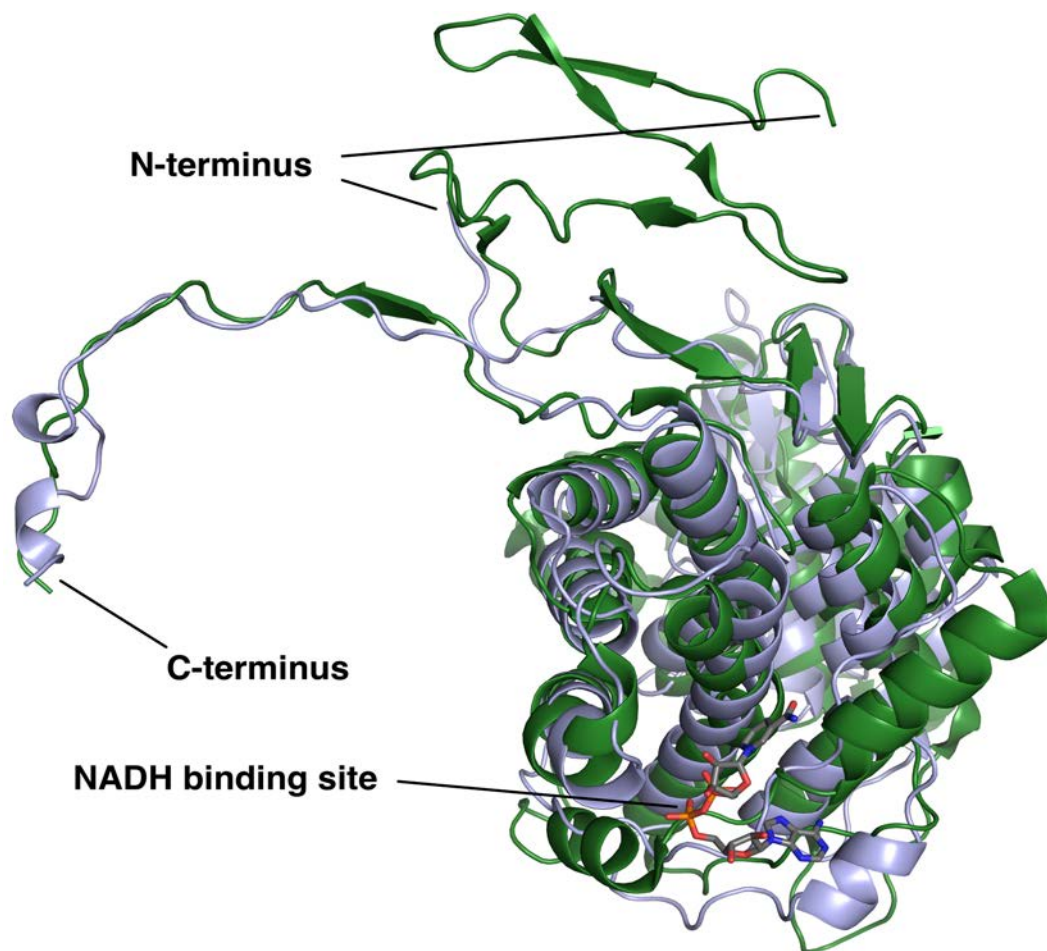


Figure 4-19: Superimposition of *E. coli* citrate synthase monomer (green) and *M. tb* cytrate synthase monomer (blue). The binding site for NADH, as well as the N-terminal and C-terminal regions, are highlighted.

4.3.3.2 Crystallization attempts with CoA and citrate

Since we were not able to observe any density for CoA in our previous structure of citrate synthase co-crystallized in presence of oxaloacetate and CoA, we attempted to crystallize citrate synthase in the presence of CoA and citrate. Both molecules are products of the reaction catalyzed by citrate synthase. This strategy has been successful for both the chicken and pig citrate synthases (PDB accession codes 2CTS and 3CTS) as well as the for *T. thermophilus* citrate synthase (PDB accession code 1IXE).

To accomplish this, the protein was dialyzed against a buffer containing 50 mM Tris pH 8.0, 10 mM sodium citrate and 0.3 mM TCEP. The protein appears less stable in this buffer since some precipitation was typically observed after dialysis. The enzyme (16.5 mg/mL) was incubated with 5 mM CoA for 2 hours. An index screen (Hampton Research) was set up with this complex using the hanging-drop vapor diffusion technique. Excessive precipitation was observed in the drops. Crystals were produced; however, mainly clusters of needle type crystals were obtained. Condition 76, composed of 0.2 M lithium sulfate, 0.1 M HEPES pH 7.5 and 25 % w/v PEG 3350, appeared promising, producing single needle/plate type crystals. These crystals are displayed in figure 4-20. Optimization of these crystals was attempted using detergent and additive screens (Hampton Research), while the well solution corresponded to condition 76. Several additives or detergents provided rod shape crystals, as well as triangular crystals (Figure 4-20). The most promising crystals were obtained with the following additives or detergents: deoxycholic acid (detergent 5), ANAPOE-X-305 (detergent 9), betaine hydrochloride (additive 37), sarcosine (additive 41) and EDTA (additive 49). Although the rod shaped crystals form between 1 and 4 days and appeared single, however,

satellites form off the main crystal after a few days. Several of these rod shaped crystals, as well as the crystals obtained with deoxycholic acid, were analyzed at the APS. Unfortunately, they diffracted poorly. Optimization of these crystals is on going.

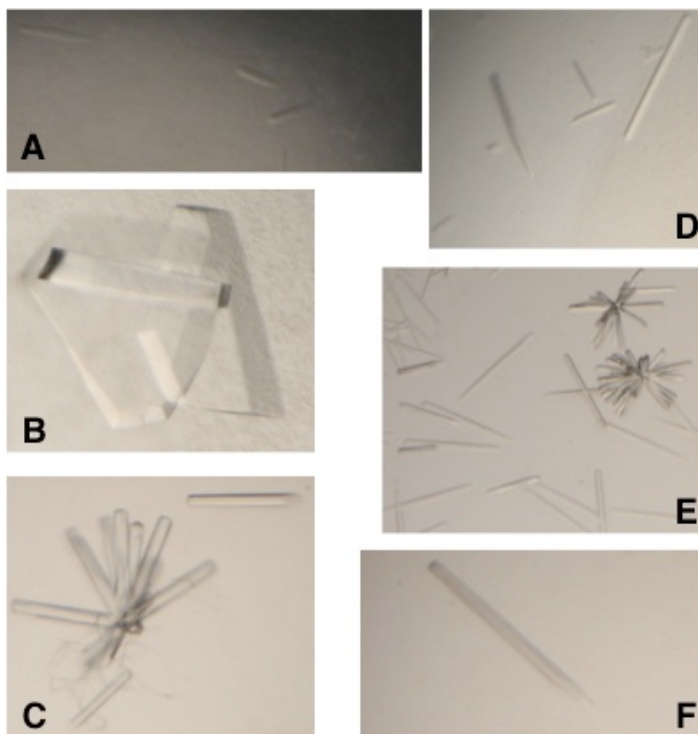


Figure 4-20: Crystals of citrate synthase with citrate and CoA. A) Cond. 76. B) Det. 5. C) Det. 9. D) Add 37. E) Add 41. F) Add. 49.

Since the citrate synthase does not appear to be stable in a buffer containing sodium citrate, we attempted to crystallize citrate synthase with only CoA. Citrate synthase was concentrated to 24 mg/mL and incubated for two hours with 20 mM CoA on ice. An index screen was set up using the hanging-drop vapor diffusion technique. Interestingly, only few crystals were obtained with the index screening and each of them grew in conditions containing organic acids similar to citrate (Figure 4-21). The

conditions were as followed: condition 63 (5 % Tacsimate™ pH 7.0, 0.1 M HEPES pH 7.0 and 10 % w/v PEG MME 5000), condition 87 (0.2 M sodium malonate pH 7.0 and 20 % w/v PEG 3350), condition 88 (0.2 M ammonium citrate tribasic pH 7.0 and 20 % w/v PEG 3350) and condition 91 (0.15 M DL-malic acid pH 7.0 and 20 % w/v PEG 3350). Tacsimate™ (Hampton Research) consists of different organic salts that include malonic acid, ammonium citrate tribasic, succinic acid, DL-malic acid, sodium acetate trihydrate, sodium formate and ammonium tartrate dibasic. Optimization of these different crystallization conditions to obtain larger single crystals and to minimize nucleation continues. To this purpose, a microbatch crystallization technique (crystallization under mineral oil) was used. This crystal tray was stored at 4 °C to minimize nucleation and minimize protein precipitation during crystallization. Thus far, no crystals have been obtained for the crystallization under oil.

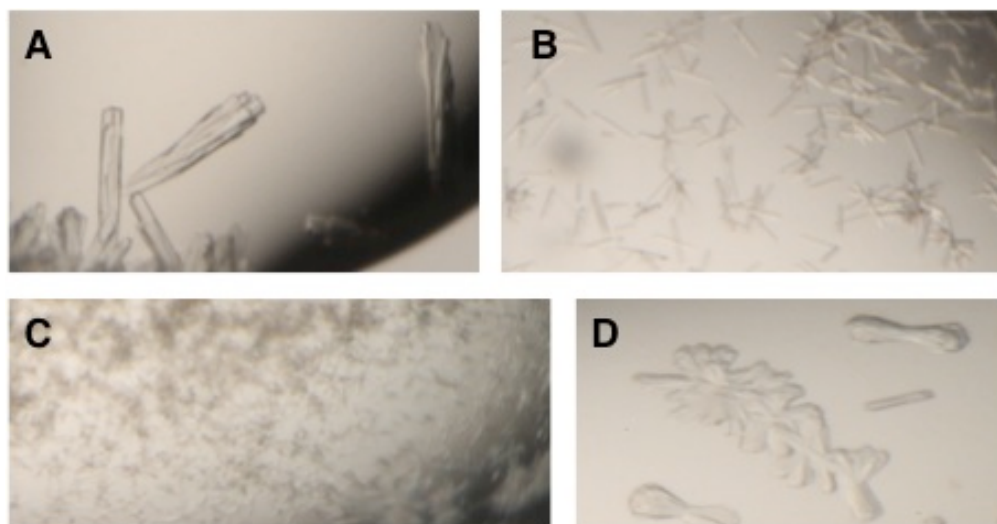


Figure 4-21: Crystals of citrate synthase with CoA. A) Cond. 63. B) Cond. 87. C) Cond. 88. D) Cond. 91.

4.4 Conclusion and future work

M. tb citrate synthase was purified and crystallized for the first time. In order to solve the crystal structure, a selenomethionine derivatized protein was prepared. The crystal structure of citrate synthase in complex with oxaloacetate, one of its substrate, provides insight about the enzyme. Unfortunately, the product CoA was not observed in this model; thus, we cannot conclude which residues are involved in the catalytic reaction performed by the enzyme. Further work is necessary to obtain crystal structures of *M. tb* citrate synthase in complex with CoA alone or with both products, CoA and citrate.

An absorbance-based assay using DTNB was developed. This assay allowed us to kinetically characterize the *M. tb* citrate synthase. The assay confirmed the role of this enzyme in the TCA cycle of *M. tb*. Although this protein is predicted to be a type II enzyme, we demonstrated that NADH does not inhibit *M. tb* citrate synthase. Experiments continue to improve this assay. Upon optimization, the assay will be used to screen the chemical libraries with the goal of discovering potential inhibitors of this enzyme. Inhibiting the enzyme's activity could be used as a tool to study the metabolism of *M. tb*, as we could inactivate the TCA cycle to study the carbon sources. Additionally, virtual screening will be performed using the GLIDE program (Schrodinger) to identify commercially available compounds that could inhibit the *M. tb* citrate synthase.

Chapter 5

Enhanced intracellular survival protein as a potential therapeutic target

5.1 Background

A characteristic difference between non-pathogenic mycobacterial species, such as *M. smegmatis*, and pathogenic mycobacteria (*M.tb*) is the ability to thrive following phagocytosis by human macrophages. However, the mechanism by which the mycobacterium is able to survive macrophage killing is yet unknown. Several mechanisms have been hypothesized such as the inhibition of phagosome-lysosome fusion or the acidification of phagosome^{29, 30}. Another hypothesis is the resistance against reactive oxygen and nitrogen intermediates. In the past ten years, studies have shown that the Enhanced Intracellular Survival (Eis) protein possesses the ability to regulate the immune response¹⁸⁴. However, the mechanism of action in pathogenesis as well as the identity of its substrates is still unknown.

In 2000, Friedman *et al.* infected the human macrophage-like cell line U-937 with *M. smegmatis* transformants containing a genomic plasmid library from *M.tb* H37Rv DNA. The experiment led to the identification of a gene (Rv2416c) with an enhanced intracellular phenotype^{184, 185}. The presence of the *eis* gene only in pathogenic strains

(*M.tb* H37Rv, H37Ra, *M. bovis* BCG) suggests that the *eis* gene product, Eis, a 42 kDa protein, contributes to the survival of mycobacteria to macrophage killing. Furthermore, fractionation of *M.tb* by differential centrifugation revealed the subcellular localization of Eis in the cytoplasm. Nevertheless, reduced levels of Eis were also localized in the cell envelope and the culture supernatant¹⁸⁵. Examination of blood serum from patients with TB showed that Eis is released across the mycobacterial cell wall as 40 % of the cases generated antibodies to the protein. Data suggest that Eis is a non-glycosylated protein¹⁸⁵. Mariani *et al.* showed evidence in 2001 that activation of infected human macrophages causes an increase in Eis expression¹⁸⁶.

Work in 2006 by Friedman *et al.* and Sharma demonstrated that Eis regulates the immune response^{187, 188}. Indeed, it modulates the secretion of cytokines produced by T-cells, particularly tumor necrosis factor α (TNF- α) and interleukin-10 (IL-10). The presence of Eis inhibits the production of TNF- α (promotes inflammation) and increases the levels of IL-10 (anti-inflammatory cytokine, inhibits the production of TNF- α) 20-fold. Not surprising, the Δeis deletion mutant showed the opposite trend. Also, levels of interferon γ (IFN- γ) in the Δeis deletion mutant were also enhanced¹⁸⁷. This event affects the cross regulation of T-cells, hence inhibiting macrophage activation and apoptosis. In addition, Friedman and co-workers confirmed that Eis was released in the macrophages less than 4 hours after infection of the patient, implying that Eis plays a role in the virulence of *M.tb*¹⁸⁸. Some new evidence suggests that Eis can inhibit the production of reactive oxygen species (ROS) to suppress the host innate immune response (i.e. macrophage autophagy, inflammation, and cell death)¹⁸⁹.

Bioinformatic analysis revealed that Eis is a member of the GCN5 superfamily of N-acetyltransferases (GNAT)¹⁸⁸. The structure of Eis solved in our lab shows that the protein presents similar fold and similar domain organization to *Anabaena variabilis* GNAT family, an uncharacterized protein; a sequence alignment confirms the similarities between the two proteins (Figure 5-1).

```

sp|P71727|EIS_MYCTU      MPOSDSVTVTLCSPTEDDWPGMFLLLAAASFTDFIGPESATAWRTLVPTDG 50
tr|Q3M362|Q3M362_ANAVT MVEPMTPRFKYTKASQENIQQLGNILEOCFVMSFGDSEIYVKGIGLENER 50
* . : . . . : : . * . : * . . . : .

sp|P71727|EIS_MYCTU      AVVVRDGAGPGSEVGMALYMDLRLTVPGEVVLPTAGLSFVAVAPTHRRR 100
tr|Q3M362|Q3M362_ANAVT VIYREQKVAGGLAILPMQWGGQR-----VMAGIAAVGIAPEYRGD 93
.: . : . . * : : * . : . : : * * : : * . : * : *

sp|P71727|EIS_MYCTU      GLLRAMCAELHRRADSGYPVAALHASEGGIYGRFGYGPATTLHELTVD 150
tr|Q3M362|Q3M362_ANAVT GAAIALIQHTLQEISEQDIPISVLYPATQRLYRKAGYEQAGSSCVWEIPT 143
* * : . : * : : * : : * : : * : * : * :

sp|P71727|EIS_MYCTU      RFARFHADAPGGGLGSSVRLVRPTEHRGEFEAIYERWRQVPGGLLRPQ 200
tr|Q3M362|Q3M362_ANAVT DSIQIQHAS----LPLEPVVLK---NNPIFHELHYQQQAQLTHGYLDRHP 185
: : : * . * * : . * . : : * . * * *

sp|P71727|EIS_MYCTU      VLWDELLAECKAAPGGDRESFALLHPDGYALYRVDRT-DLKLARVSELRA 249
tr|Q3M362|Q3M362_ANAVT AIWOGLNRTLDTETLYSYLIGDKDKPOGYIIFTOERTRDGSILRIRDWVT 235
.: * : * . : . . : * : * : : * * * : : * : :

sp|P71727|EIS_MYCTU      VTADAHCALWRALIG-LDSMERISIITHPQDPLPHLLTDTRLARTTWRQD 298
tr|Q3M362|Q3M362_ANAVT LSNPAVQSFWTFIANHRSQIDKVTWKSSVIDALTLLLPEQ--SATIRSQD 283
: : * : * : . . : : : : : * . * . * : : * * *

sp|P71727|EIS_MYCTU      GLWLRIMNVPAALEARGYAHEVG----EFSTVLEVSDGGRFALKIGDGR 343
tr|Q3M362|Q3M362_ANAVT RNMLRIVNVCKALEARGYPLGVEAELHLEVQDDLLATNOGKFILSVANGK 333
* * : * * * * * . * * . * : : * : * . : : * :

sp|P71727|EIS_MYCTU      ARCTPTDAAAEIEMDRDVLGSLYLGAHRASTLAAANRLRTKDSQLLRRLD 393
tr|Q3M362|Q3M362_ANAVT SEVT-KGGKGELQLDIKGLASLYTSLFTPRQLQLTGKLQATETALK-AT 381
: . * . . . * : : * . * . * * . . . * : : : : : : * :

sp|P71727|EIS_MYCTU      AAFASDVVPVQTAFEF 408
tr|Q3M362|Q3M362_ANAVT QIFAGESPWMIDFF- 395
* * : * *

```

Figure 5-1: Sequence alignment of Eis with AvGNAT. The top sequence represents Eis from *M.tb* while the bottom sequence represents AvGNAT, a member of the GCN5 superfamily of N-acetyltransferases. * represents identical residues. The regions in red indicate those of highest conservations while the blue ones are the most variables.

Hence, the acetyl moiety from AcCoA is transferred to an amine of an acetyl acceptor using the proposed mechanism below (Figure 5-2)¹⁹⁰. The mechanism undergoes the formation of a ternary complex with the addition of AcCoA and the co-substrate; then a general base deprotonates the amine of the acetyl acceptor, allowing a nucleophilic attack of the thioester on AcCoA and releasing a free thiol (CoA). Posey *et al.* have shown that Eis is able to transfer an acetyl group from AcCoA to kanamycin (KAN) and amikacin (AMK), two aminoglycosides used as second-line TB drugs¹⁹¹.

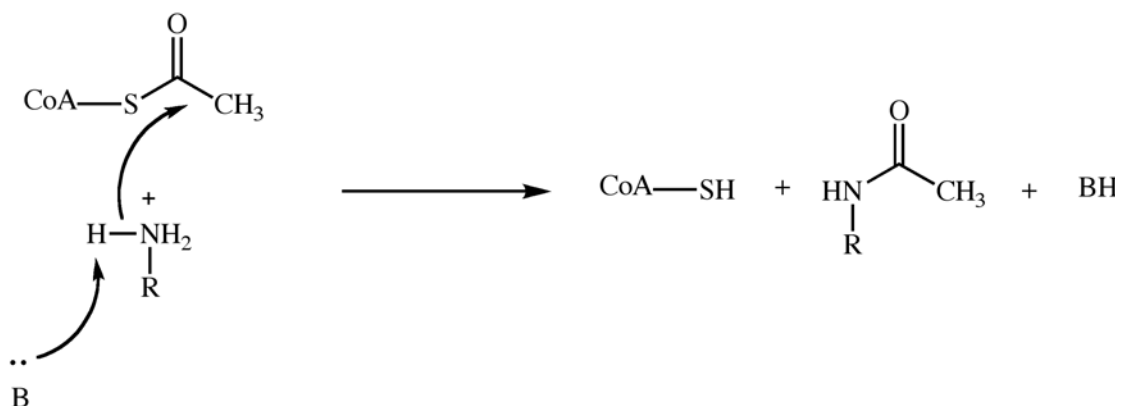


Figure 5-2: Proposed N-acetyltransferase mechanism

The aim of this research was to understand the mechanism by which Eis allows *M.tb* to survive within the macrophage. To this purpose, our laboratory crystallized Eis and solved its structure. Tsodikova and co-workers solved the Eis structure with CoA bound¹⁹², confirming our proposed structure and the similarities with other N-acetyltransferases. The second goal for this project was to determine the co-substrate(s) of Eis, i.e. the acetyl acceptor(s) in macrophage, and to characterize the interactions

between Eis and its co-substrates using diverse tools such as binding studies, steady-state kinetics and X-ray crystallography.

5.2 Experimental procedures

5.2.1 Purification of Eis

The *eis* gene was amplified from H37Rv genomic DNA and ligated into pET28 plasmid (EMD biosciences) between the restriction sites *NdeI* and *BamHI* by a former student in the laboratory⁹⁰. The construct contains an N-terminal poly-histidine tag that is potentially cleavable by a PreScissionTM protease. The purified plasmid containing *eis* was used to transform T7 express cells (New England BioLabs[®]). Cultures were grown in Luria Broth (Research Products International) at 37 °C in presence of 50 mg/L of kanamycin (Gold Biotechnology) and 30 mg/L of chloramphenicol (Alfa Aesar). Once an OD_{600 nm} of 0.6 was reached, the cells were induced at 16 °C between 16 and 36 hours by addition of 1 mM IPTG (Gold Biotechnology). The cells were then harvested by centrifugation and resuspended into 20 mM Tris pH 7.5, 25 mM imidazole, 0.3 M NaCl, 5 mM β-Me. The cells were lysed using 1 mM of lysozyme and 0.1 mM of DNase, as well as a sonication step. The crude lysate was pelleted by centrifugation at 11,000 rpm (fixed-angle rotor, 5810-R Centrifuge, Eppendorf). The filtered supernatant was loaded onto a 5 mL HisTrapTM HP column packed with Ni SepharoseTM (GE Healthcare) and washed with 15 column volumes of resuspension buffer. The protein was eluted from the column using a linear gradient of imidazole from 25 to 250 mM over 20 column volumes (Figure 5-3).

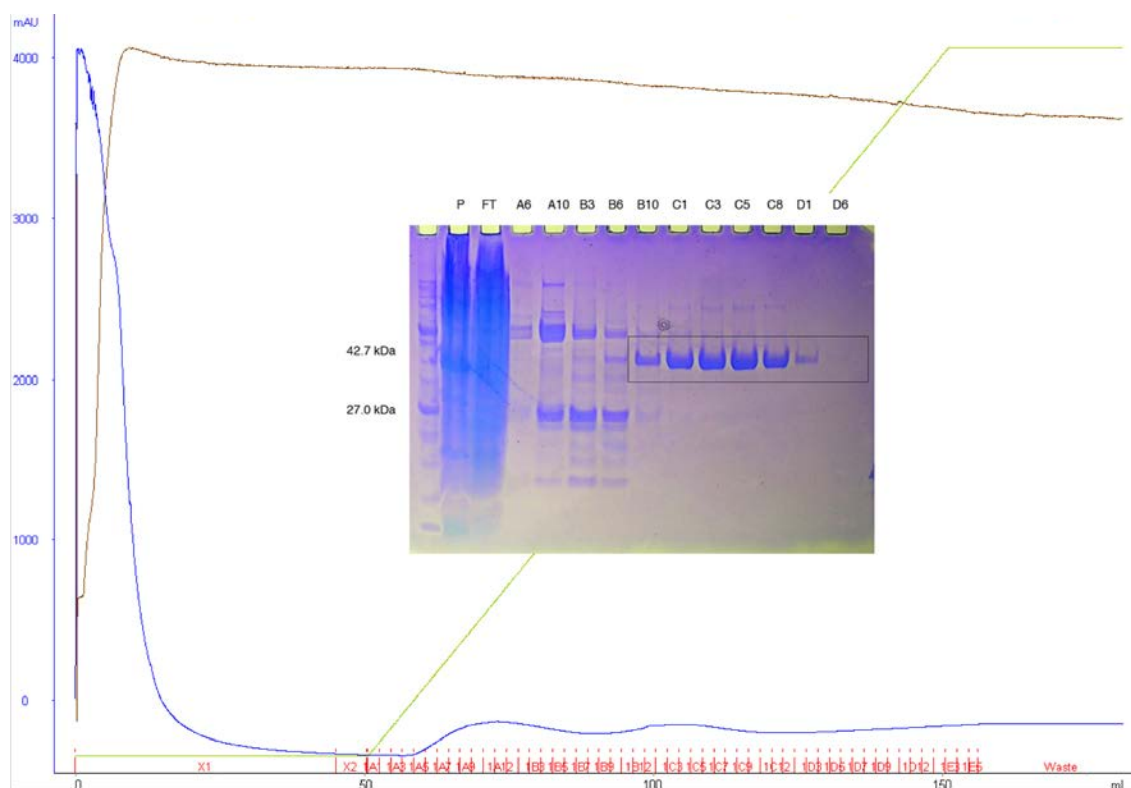


Figure 5-3: Chromatogram and SDS-PAGE gel from nickel affinity purification of Eis. The blue line corresponds to the absorbance monitored at 280 nm while the green line represents the concentration of buffer B (higher concentration in imidazole). The brown line corresponds to the conductivity measured.

The fractions containing Eis were pooled and dialyzed overnight against the binding buffer. PreScissionTM protease was added to cleave the polyhistidine tag. The dialyzed protein was again subjected to nickel affinity chromatography to eliminate the poly-histidine tag, as well as the protease. Anion exchange chromatography using a HiTrapTM Q FF column was necessary to further purify Eis; the elution was carried out using a linear gradient of NaCl from 0 to 1 M (Figure 5-4). If necessary, size exclusion steric was performed as a polishing step.

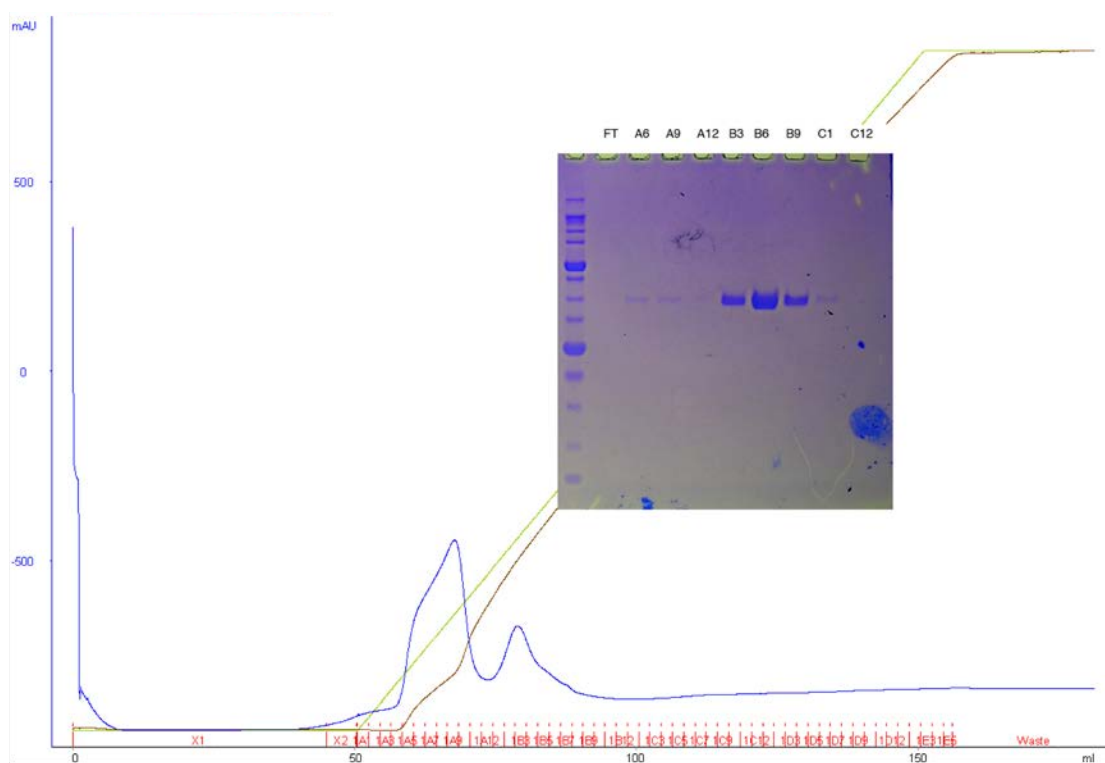


Figure 5-4: Chromatogram and SDS-PAGE gel from anion exchange purification of Eis. The blue line corresponds to the absorbance monitored at 280 nm while the green line represents the concentration of buffer B (higher concentration in imidazole). The brown line corresponds to the conductivity measured.

A selenomethionine derivatized Eis protein was also prepared in order to obtain phasing information on Eis and to create a model. This protein was purified using the same protocol.

5.2.2 Crystallization studies of Eis

The protein was concentrated by ammonium sulfate precipitation (2.6 M). The pellet obtained was resuspended in crystallization buffer (10 mM Tris pH 8.5, 2 mM EDTA, and 1 mM DTT or TCEP). The purified protein was then dialyzed against the same buffer. Between 1 and 5 mg/mL of Eis were obtained, depending on the duration of the induction. Eis was co-crystallized with CoA and KAN as following: 1 mg/mL of recombinant protein was allowed to incubate on ice for 30 minutes in presence of 25 mM KAN and different concentrations of CoA; then, 1 μ L of the mixture was added to 1 μ L of the crystallization condition determined from an index screening HR2-144 commercialized by Hampton Research (0.1 M Tris pH 8.5, 0.2 M MgCl₂, 14 % w/v PEG 3350). The process was enhanced by the addition of 1 % glycerol. Further, the recombinant protein was co-crystallized with CoA alone. The crystals obtained (rhombohedral form) took about 2 weeks to grow under mineral oil. The selenomethionine derivatized protein was crystallized using the same crystallization condition.

The crystals were flash-frozen using liquid nitrogen prior to data collection. All the diffraction data were collected at the LS-CAT beamline at the APS-ANL.

5.2.3 Structure determination of Eis

X-ray data were indexed, integrated and scaled using HKL2000⁹². A multiwavelength anomalous dispersion (MAD) experiment was also carried out in the case of the selenomethionine derivatized Eis.

Using the model built from the MAD experiment as a template, rigid body refinement, simulated annealing, positional and B-factor refinement were carried out using the refine tool in PHENIX⁹⁵. COOT was used to manually correct the model⁹⁶.

5.2.4 Identification of Eis co-substrate *in vivo*: first approach

5.2.4.1 Analogs of myristoyl-CoA and AcCoA: synthesis

The synthesis was carried out using the procedure of Darley and co-workers¹⁹³ (Figure 5-5).

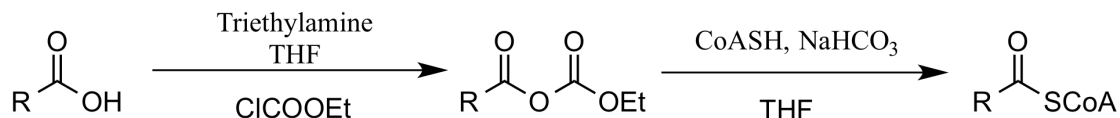


Figure 5-5: General scheme for the synthesis of AcCoA and myristoyl-CoA analogs

In a 10 mL flask, 10 mg of the starting material in dry tetrahydrofuran (THF) was stirred with triethylamine (12 μL) and ethylchloroformate (12 μL) for 30 minutes. A white residue appeared. The solvent was then evaporated. The residue was resuspended in THF (1.4 mL) and centrifuged for 2 minutes at 13000 rpm. The supernatant solution was added to Coenzyme A trilithium salt dihydrate purchased from MP Biomedical (16 mg) in 1 mL aqueous sodium bicarbonate (100 mM). The mixture was stirred for 40 minutes then extracted with ethyl acetate (3x1 mL). Aqueous layers were acidified to pH 3 by small addition of Dowex x50 (H^+ form) and washed with ethyl acetate (3x1 mL). The water was removed by evaporation. The white residue was resuspended into 10 mM

Tris pH 8.5, 2 mM EDTA, 1 mM TCEP and stored at -70°C. Products were characterized by ESI using a Hewlett-Packard Esquire Ion Trap LC-MS.

The compounds are presented in a later section (Figure 5-11-A). The starting materials were chloroacetic acid to synthesize chloroacetyl-CoA (abbreviated as ClAcCoA in following sections), and tetradec-13-ynoic acid for tetradec-13-ynoyl-CoA (abbreviated as Alk-CoA in following sections). To synthesize ClAcCoA, chloroacetic acid was directly reacted with CoA.

5.2.4.2 Cloning of *gfp*, expression and purification of Green Fluorescent Protein

The gene encoding Green Fluorescent Protein (GFP) was amplified by PCR using the primers described in table 5-1 (Integrated DNA Technology). The 3' primer was designed to encode a 6X-Histidine tag at the C-terminus of the protein, followed by a serine, an alanine and a cysteine residue. The thiol moiety on the cysteine will be used to react with the ClAcCoA compound. The gene was ligated into a pET28-based vector (EMD biosciences) between the restriction sites *NcoI* and *BamHI* (New England BioLabs). The sequence was confirmed using nucleotide sequencing conducted at the DNA Sequencing Core (University of Michigan, MI).

Table 5-1: Primers used for the amplification of *gfp* gene

GFP-NcoI	AAGGAGATATACCATGGTGAGCAAGGGCGAGGAGC
GFP-BamHI	TCGAATTCGGATCCTCAGCACGCGCTATGATGATGATGATGGTG

The plasmid containing the gene encoding GFP was used to transform *E. coli* T7 express cells (New England BioLabs). Bacterial cells were cultured in Luria Broth (Research Products International) at 37 °C in presence of kanamycin (Gold Biotechnology) and chloramphenicol (Alfa Aesar). At an OD_{600 nm} 0.6, 1 mM of IPTG was added to induce protein expression at 16 °C for 16 hours. The cells were harvested by centrifugation and resuspended in the same resuspension buffer as Eis. Lysis and nickel affinity were carried out using the same protocol as Eis. Finally, GFP was dialyzed against 20 mM Tris pH 7.5, 0.3 M NaCl, 5mM β-Me (Figure 5-6).

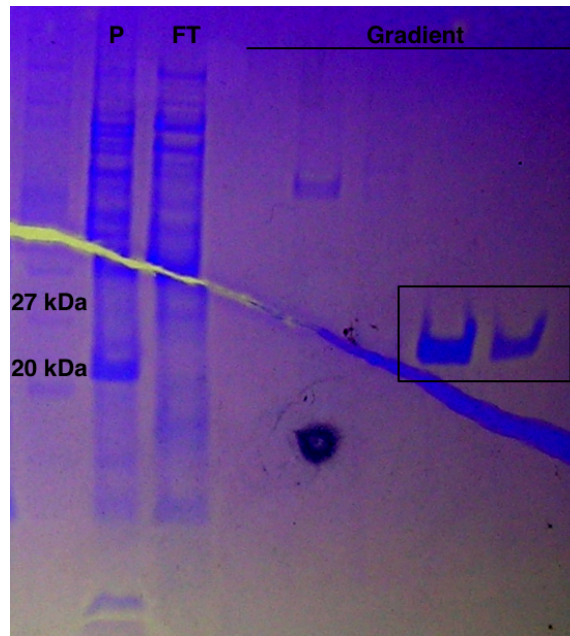


Figure 5-6: SDS-PAGE gel showing purity of GFP after nickel affinity purification

5.2.4.3 Proteomic experiment using CoA analogs and GFP

BCG and H37Ra strains were used. The cells were grown to an $OD_{600\text{ nm}}$ 0.2, and then harvested. The cell pellets were resuspended into 1 mL of phosphate buffered saline (10 mM sodium phosphate pH 7.5, 150 mM sodium chloride). The cells were lysed, split in 5 aliquots for each strain and stored at -70°C . This procedure was performed by Dr. Liem Nguyen's laboratory (Case Western University, Cleveland, OH).

Only ClAcCoA and Alk-CoA were used. For each strain, 5 reactions were performed:

1- Control A: only Eis

2- Control B: Alk-CoA

3- Control C: ClCoA

4- Reaction A: Eis + Alk-CoA

5- Reaction B: EIS + ClCoA

First, 5 μM of EIS and 100 μM of the modified CoA compounds were added to the lysates and allowed to sit for two hours at room temperature. Then, 0.2 mM TCEP, 0.2 mM copper sulfate and 100 μM biotin dPEG azide were added to the control B and the reaction A whereas 200 mM Tris buffer solution pH 8.5, 100 μM GFP labelling protein and 0.2 mM TCEP were added to the control C and the reaction B. The reactions were incubated for 2 hours at room temperature. The first reaction (A) was purified using Streptavidin MagneSphere® Paramagnetic Particles (Promega) while the second (B) was purified using nickel affinity chromatography. A native PAGE gel was run to visualize

the GFP protein using a blue-light transilluminator in the case of the first reaction. The second reaction used a SDS-PAGE.

5.2.5 Identification of Eis co-substrate *in vivo*: second approach

Dr. Choong-min Kang (Wayne State University, Detroit, MI) provided cell pellets from monocyte-derived human macrophages that were used in the bisubstrate inhibitor approach, as well as the substrate profiling experiment. The cell pellets were resuspended in 5 mM sodium phosphate pH 7.5 and 0.3 mM TCEP. The macrophages were lysed using liquid nitrogen and sonication (30 seconds).

5.2.5.1 Bisubstrate inhibitor approach

The bisubstrate inhibitor approach was carried out using the protocol developed by Xu *et al*¹⁹⁴. Briefly, ClAcCoA was incubated in presence of Eis in a macrophage lysate for an hour at room temperature. An excess of CoA was then added and the reaction was allowed to process for 5 hours at room temperature. The lysate was subjected to nickel affinity purification using a batch method and the different fractions obtained during the purification were analyzed by SDS-PAGE.

5.2.5.2 Substrate profiling experiment

The procedure was described by Blanchard and co-workers in 2006¹⁹⁵. First, ClAcCoA was incubated in presence of Eis in a macrophage lysate for an hour at room temperature. A peptide containing a poly-histidine tag, an N-terminal fluorescein label

and a terminal cysteine (Peptide 2.0) was incubated with the lysate for 5 hours at room temperature. A nickel affinity step was carried out to purify the lysate and isolate the acetylated co-substrate(s) of Eis. The eluted product(s) were analyzed by SDS-PAGE. The fluorescent band(s) were subjected to trypsin digestion and analyzed on MALDI-MS.

5.3 Results and Discussion

5.3.1 Solving Eis structure

The first aim of this project was to optimize the crystallization of Eis in order to improve the diffraction quality of the crystals. To do so, different screens in which the percentage of PEG 3350 was varied were attempted. The addition of glycerol was used to enhance the process. The crystals obtained have a rhombohedral shape (Figure 5-7). Diffraction data to 2.2 Å were obtained at the APS.

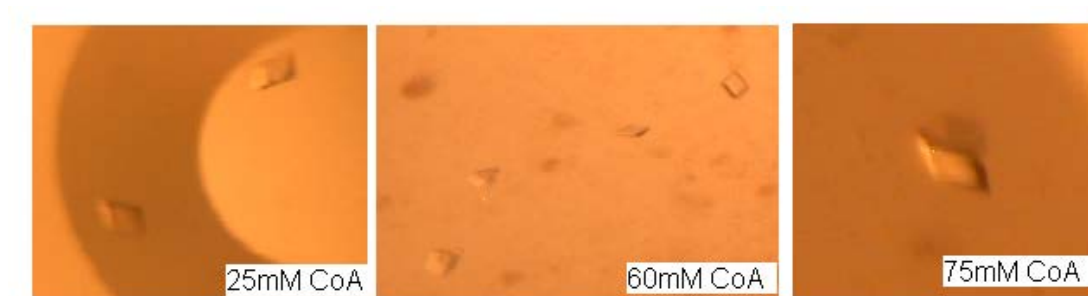


Figure 5-7: Crystals of Eis co-crystallized in presence of different concentrations of CoA

Dr. Julie Boucau and Dr. Donald Ronning performed a MAD experiment to create the original model of Eis; however, the data only extended to 3.0 Å. For this reason, the experiment was repeated to improve the resolution of the data. A new crystal of selenomethionine derivatized Eis (Eis SeMet) was obtained and diffraction data was extended to 2.6 Å. Table 5-2 summarizes the data collected, as well as the refinement and phasing statistics.

Table 5-2: Data collection, phasing and refinement statistics.

Data Collection	Eis SeMet	Eis
Space Group	R32	R32
Unit Cell Dimensions		
<i>a, b, c</i> (Å)	161.7, 161.7, 172.9	162.9, 162.9, 176.2
α, β, γ (°)	90.0, 90.0, 120.0	90.0, 90.0, 120.0
Resolution (Å)	50.0-2.60	50.0-2.20
Completeness (%)	96.9	99.9
Refinement		
Resolution (Å)	50.0-2.60	50.0-2.20
Unique Reflections	26705	45682
$R_{\text{work}}/R_{\text{free}}$	20.9/30.0	21.0/26.1
<i>B</i> -factors (Å ²)	46.2	33.6
R.m.s. deviations		
Bond lengths (Å)	0.009	0.008
Bond angles (°)	1.293	1.176

The Eis structure was refined to 2.20 Å with a R_{work} of 21.0 % and a R_{free} of 26.1 %. Data show that Eis forms a hexamer as does the *Anabaena variabilis* GNAT (AvGNAT) protein (PDB: 2OZG) (Figure 5-8-A). As expected, Eis presents a similar fold to other N-acetyltransferase. Figure 5-8-B highlights the similarities between the monomer AvGNAT and our structure. In addition to the similarities in the fold of the

monomer, the rather unique domain organization and oligomeric structure observed in the AvGNAT protein is mirrored in the Eis structure.

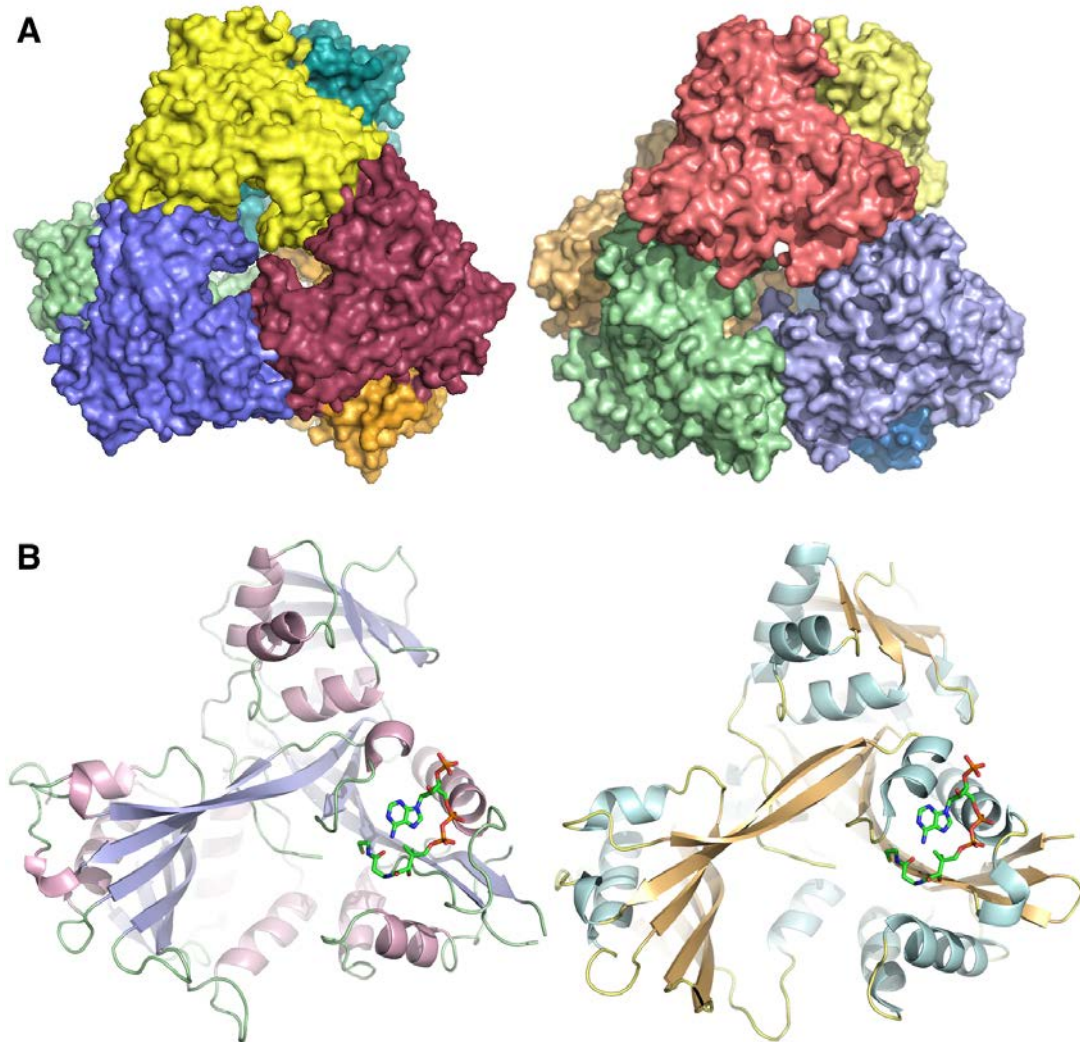


Figure 5-8: Comparison of Eis and AvGNAT (PDB: 2OZG). A) Eis (left) shows a similar hexamer form as AvGNAT (right). B) The model of Eis with CoA bound (left) exhibits the same fold and the same domain organisation as AvGNAT (right).

Although the active site is well resolved, almost no density is visible for CoA, except a small region of density that could potentially correspond to one of the phosphates or more likely the diphosphate moiety of CoA based on the position of CoA in other N-acetyltransferase structures (Figure 5-9). Higher concentrations of CoA (5-75 mM CoA) were used for both co-crystallization and soaking immediately prior to X-ray diffraction studies, but a structure of an Eis-CoA complex eludes us.

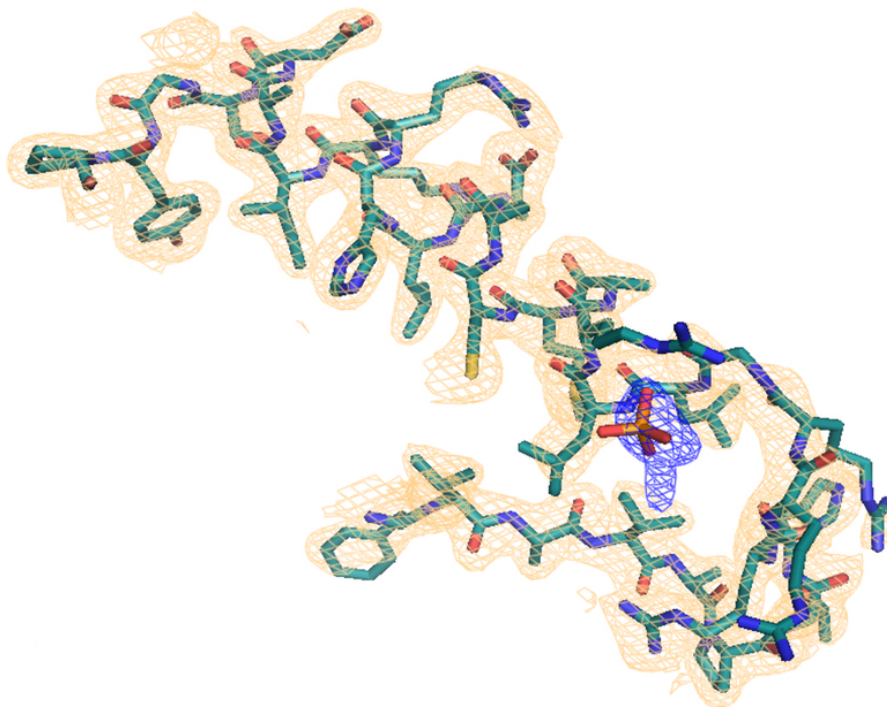


Figure 5-9: Active site of Eis. The active site of Eis is well resolved as displayed with this 2FoFc map (orange); however, no density is observed for CoA, except for a density that possibly corresponds to one of the phosphates or the diphosphate moiety of CoA (blue).

In 2011, Tsodikova *et al.* published the structure of Eis with CoA and acetylated hygromycin (HYG), an aminoglycoside, bound¹⁹². The complex crystallized in a different condition than ours (0.1 M Tris pH 8.5, 8-12 % w/v PEG 8000) for the native Eis in

complex with CoA and acetylated HYG. The purification protocol used was also different. The amount of protein used for crystallization was 3.5 mg/mL while our lab was using 1 to 2 mg/mL. We attempted to reproduce the conditions indicated in the article but only small and multiple crystals were obtained. Optimization of the conditions using additive screen (HR2-428, Hampton Research) and detergent screen (HR2-408, Hampton Research) were attempted. Two detergents (Det. 50: n-octyl-b-D-thioglucoside; Det. 60: n-heptyl-b-D-thioglucopyranoside) allowed us to obtain larger crystals. In addition, the crystal obtained in the detergent 60 was single (Figure 5-10). The crystals took approximately 3 weeks to a month to grow. Attempts to reproduce these crystals were unsuccessful. Using a higher concentration solution of Eis in complex with CoA (8.8 mM) and KAN (10 mM), a new index screening (Hampton Research) was set up using hanging-drop vapor diffusion. Diverse conditions led to single large crystals (Figure 5-10), in particular conditions 56 (0.2 M KCl, 0.05 M HEPES pH 7.5, 35 % v/v pentaerythritol propoxylate (5/4 PO/OH)), 62 (0.2 M Trimethylamine N-oxide dihydrate, 0.1 M Tris pH 8.5, 20 % w/v PEG MME 2000) and 63 (5 % w/v Tacsimate pH 7.0, 0.1 M HEPES pH 7.0, 10 % w/v PEG MME 5000). These crystals took approximately 3 weeks to grow. Diffraction data for some of these crystals were obtained, but again no density for CoA was observed.

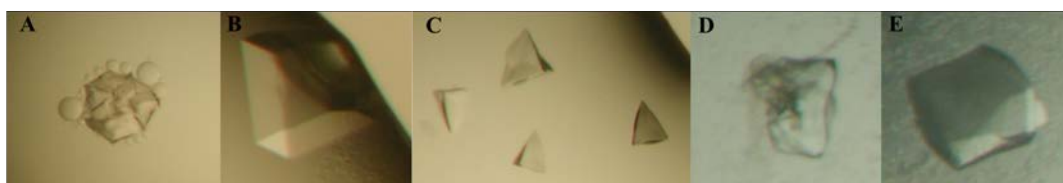


Figure 5-10: New crystals of Eis co-crystallized with CoA and KAN. Detergent Screen: A) Det. 50; B) Det. 60. Index Screening: C) Cond. 56; D) Cond. 62; D) Cond. 63.

5.3.2 Identification of Eis co-substrate *in vivo*: first approach

The second aim of this project was to identify the acetyl acceptor of Eis *in vivo*. One noticeable difference between the structures of AvGNAT and Eis is that the active site of AvGNAT is narrower in comparison to Eis. Bioinformatic analysis of the preliminary structure using the Dali server indicates that Eis has a fold and organization similar to N-acetyltransferases as expected¹⁹⁶. Nevertheless, this analysis also reveals that the structure is comparable to N-myristoyltransferases (Table 5-3). As the Eis active site in our structure is larger than typical N-acetyltransferase active sites, we hypothesized that the active site could accommodate the 14-carbon chain of myristoyl-CoA.

Table 5-3: Bioinformatic analysis of the preliminary structure indicates that Eis has a fold and organization similar to N-acetyltransferases and N-myristoyltransferases.

Access code	Z score	rmsd	Description
2OZG	37.7	2.7	Hypothetical N-acetyltransferase
2I00	37.4	2.4	N-acetyltransferase
1NMT	16.8	5.5	N-myristoyltransferase
2P6F	15.6	5.7	Glycylpeptide N-tetradecanoyltransferase
2WUU	15.0	4.9	N-myristoyltransferase

In order to determine the co-substrate of Eis *in vivo*, two compounds were synthesized, an analog of Ac-CoA and an analog of myristoyl-CoA. The compound structures are presented in figure 5-11-A. Both molecules were synthesized using the synthesis developed by Darley *et al.*¹⁹³. Then, two strategies were attempted to identify the acetyl or myristoyl acceptor(s) of Eis. With the collaboration of Dr. Liem Nguyen's laboratory (Case Western University, Cleveland, OH), cell lysates from BCG and H37Ra strains were used to perform the following experiments.

First, Eis and either ClAcCoA or Alk-CoA were allowed to incubate in a mycobacterial cell lysate, leading to the formation of an acetylated or myristoylated protein, i.e. the co-substrate of Eis. Then the lysate containing the myristoylated protein was reacted with biotin dPEG azide through click chemistry, leading to the formation of a 1,2,3-triazole product (Figure 5-11-B). The biotin moiety can then be used to bind to Streptavidin MagneSphere® Paramagnetic Particles to isolate the protein that was originally myristoylated. In a second reaction, the chloroacetylated protein is incubated with GFP (Figure 5-11-C). When primers were design to amplify the gene encoded GFP, the GFP-BamHI primer was designed to provide a 6X-Histidine tag at the C-terminus of the protein, followed by a serine, an alanine and a cysteine residue. The thiol moiety on the cysteine was used to promote a nucleophilic attack on the carbon possessing the chloride in ClAcCoA. Since GFP has a poly histidine tag, nickel affinity purification can be carried out to isolate the acetylated protein. Appropriate controls in which only the compounds were added to the lysate without Eis were run in parallel to these reactions. The samples for the myristoylation were analyzed by SDS-PAGE while the acetylation reaction was analyzed using a native gel. The native gel was used to maintain GFP folded

correctly, so that the gel could be visualized with a blue light and a fluorescent band corresponding to the modified protein would be observed.

Nonetheless, no result was obtained from these experiments. No fluorescence was observed for the second experiment. In addition, the click chemistry was attempted in a control reaction with different experimental conditions (different types of reductants for instance). However, based on ESI-MS data, the expected 1,2,3-triazole product was never observed. Degradation of the Alk-CoA was hypothesized to be the cause. To replace this compound, a bromoundecanoylCoA (BrCoA) was synthesized using the same protocol as the other analogs. This new compound was used to run an experiment similar to the one using ClAcCoA, but again, the results were inconclusive.

While optimizing these two proteomic experiments, the structure of Eis was solved by Tsodikova and co-workers as mentioned in the previous section¹⁹². Based on their structure, and knowing exactly how CoA was bound in the active site, we attempted to model myristoyl-CoA in their structure. However, the 14-carbon chain did not appear to fit. Thus, we concluded that Eis is likely an acetyltransferase, and not a myristoyltransferase. For this reason, the myristoyl-CoA analogs were not pursued in future proteomic experiments carried out for Eis.

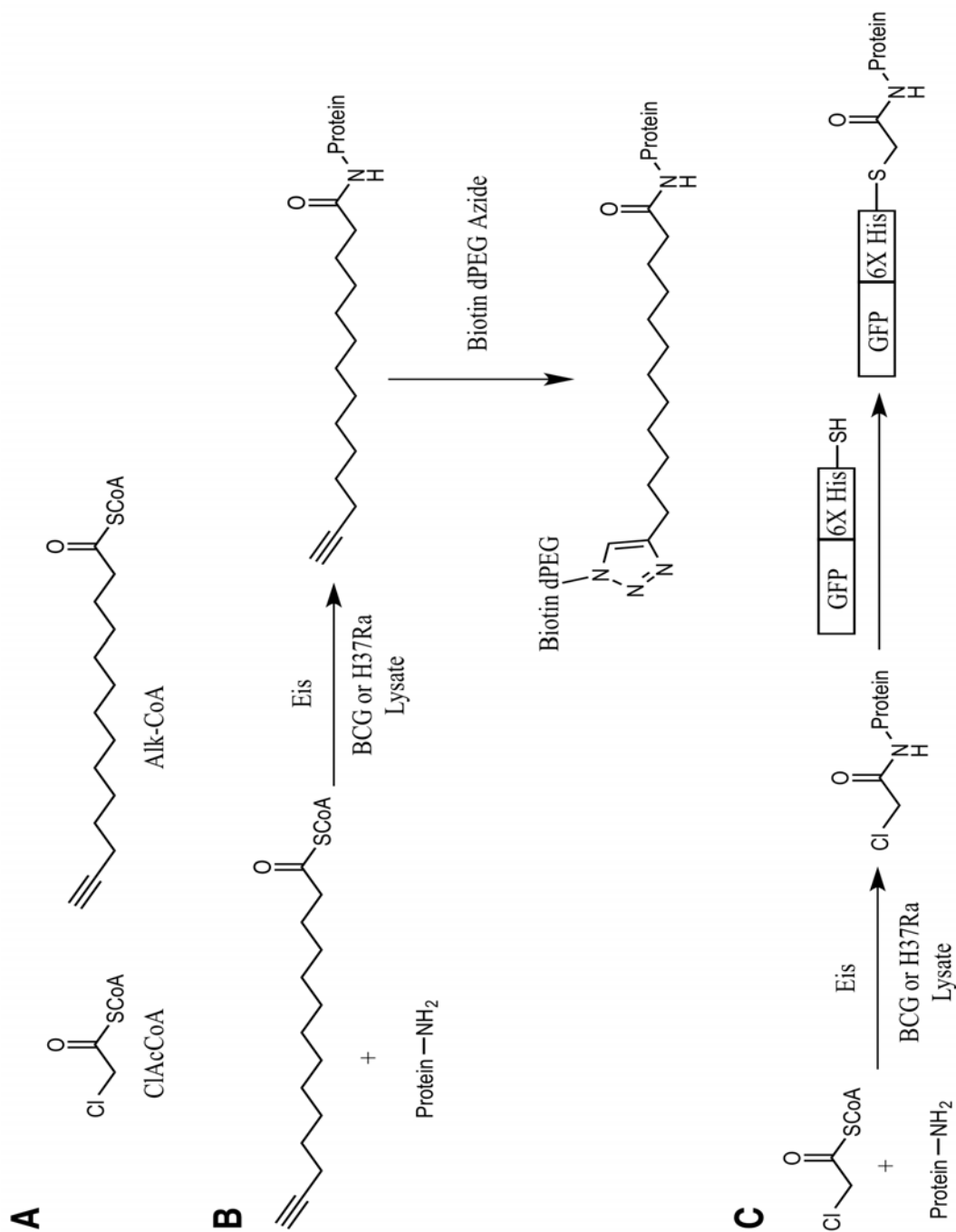


Figure 5-11: First approach to identify Eis co-substrate *in vivo*. A) Myristoyl and AcCoA analogs synthesized. B) First reaction using Alk-CoA, biotin dPEG azide and click chemistry to isolate the target protein of Eis. C) Second approach using ClAcCoA and GFP.

5.3.3 Identification of Eis co-substrate *in vivo*: second approach

5.3.3.1 Preliminary results

To confirm that Eis acetylates a target in the macrophages, a preliminary experiment was carried out with the collaboration of Dr. Kang at Wayne-State University (Detroit, MI). AcCoA was incubated in the macrophage lysate in presence of Eis. Then a Western Blot with specific antibodies for acetylated proteins was performed to identify potential target(s) of Eis. A control reaction in macrophage lysate without Eis was also carried out. As shown in Figure 5-12 (red box), a small molecular weight protein (estimated to approximately 15 kDa after performing the substrate profiling experiment) was acetylated in presence of Eis. Attempts to identify the protein by mass peptide fingerprinting were unsuccessful due to the low concentration of the samples.

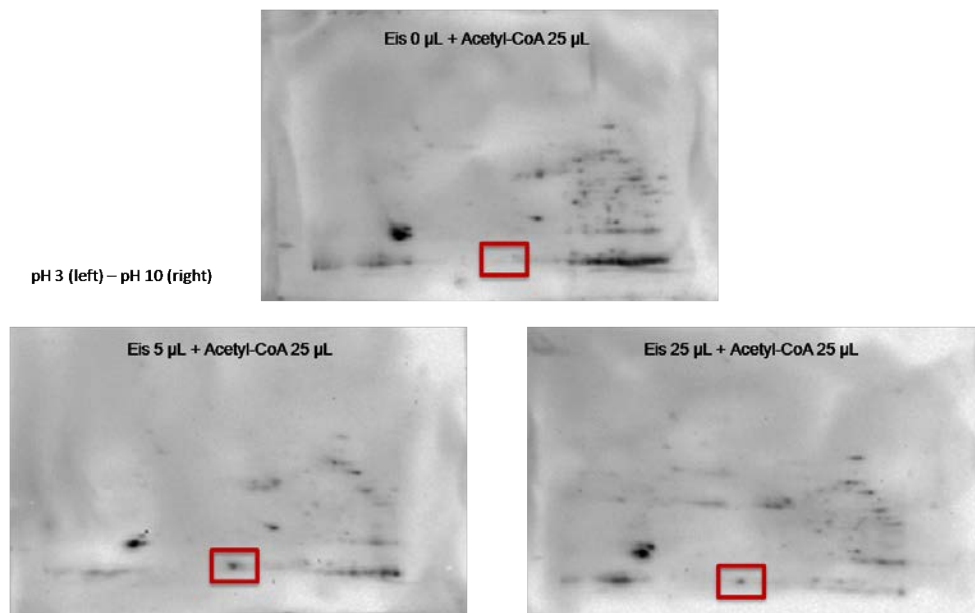


Figure 5-12: 2D Western Blot gels. The experiment shows that a protein, not present in the control (top gel), was acetylated in presence of Eis. The red boxes highlight the location of this protein. (Courtesy of Dr. Kang)

The two following approaches also use a macrophage lysate. A scheme is summarized in figure 5-13.

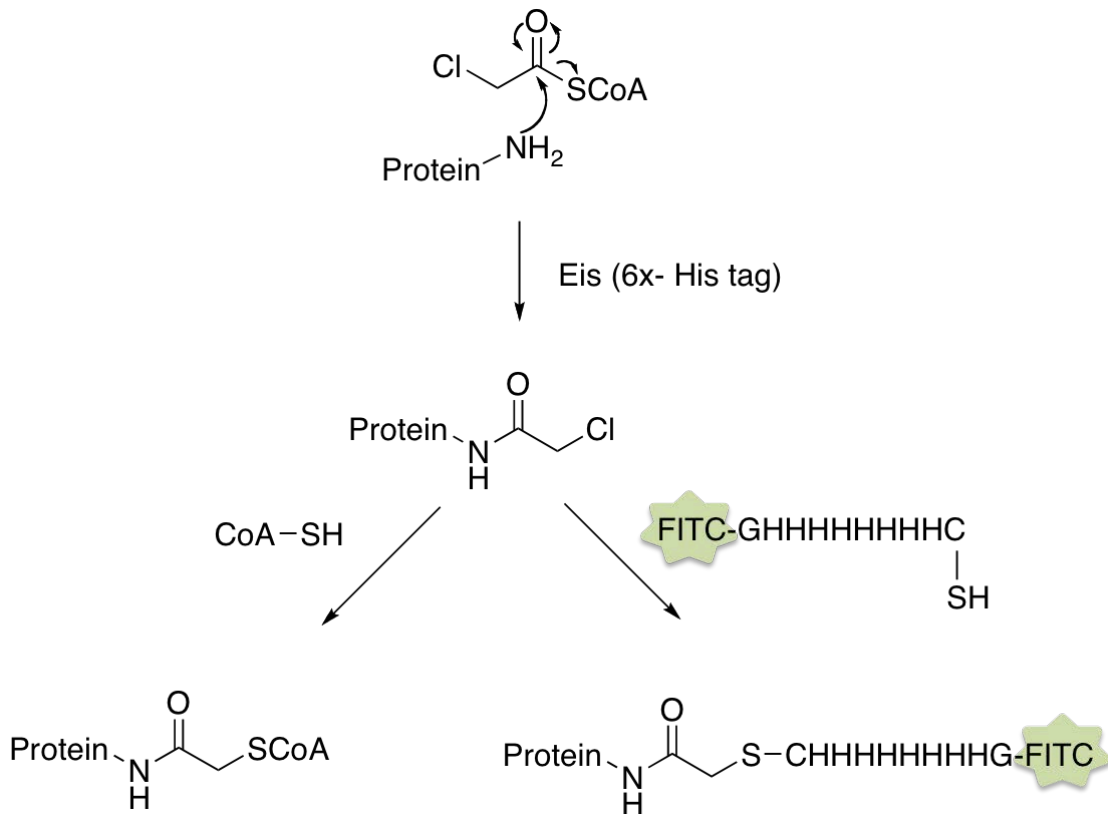


Figure 5-13: Proposed experimental scheme for the identification of the acetyl acceptor. The pathway on the left uses the bisubstrate inhibitor approach while the one on the right shows the substrate profiling experiment that uses a poly-histidine peptide containing FITC and a C-terminal cysteine.

5.3.3.2 Bisubstrate inhibitor approach

A bisubstrate inhibitor approach developed by Xu *et al* was successfully used to determine the substrate of another acetyltransferase from *M. tb*, *MsPat*¹⁹⁴. The experiment was carried out using the ClAcCoA compound.

The ClAcCoA compound used in section 5-3-2 was allowed to react with the co-substrate in presence of Eis in a macrophage lysate. Subsequently, an excess of CoA was added to promote a substitution reaction with ClAcCoA to allow the formation of a ternary complex trapped within the active site of Eis. The lysate was then subjected to nickel affinity purification; the non-acetylated proteins should be washed away while the acetyl acceptor, trapped within the active site of Eis that contains a poly-histidine tag, should bind to the resin. The products were then eluted from the column and analyzed by SDS-PAGE. The aim was to analyze the band corresponding to the co-substrate by mass peptide fingerprinting on MALDI and identify the co-substrate. However, we were unable to isolate the ternary complex trapped within the active site of Eis.

5.3.3.3 Substrate profiling experiment

A substrate profiling experiment was developed by Blanchard and co-workers and allowed the determination of substrates of GCN5-related N-acetyltransferase¹⁹⁵.

In a second aliquot of human macrophage lysate containing the reaction between ClAcCoA and the unknown co-substrate in presence of Eis, a peptide that contains a poly-histidine tag, an N-terminal fluorescein label and a C-terminal cysteine, was added to the lysate. A nucleophilic attack by the C-terminal cysteine present on the peptide should occur on the chloride of ClAcCoA. A nickel affinity purification was performed in order to isolate the acetylated co-substrate(s) of Eis. Consequently, several fluorescent band(s) were observed on a SDS-PAGE. However, the bands corresponded to the flowthrough and the wash, meaning that the peptide did not bind to the nickel resin. The bands were subjected to trypsin digestion and analyzed by MALDI in order to identify

the chloroacetylated protein(s). Nonetheless, the mass peptide fingerprinting was inconclusive due again to low concentration of the samples. In order to increase the concentration of the samples, an acetone precipitation was carried out on the fraction and a new SDS-PAGE was run (Figure 5-14). The observed bands were more intense and mass peptide fingerprinting was again attempted. The software MASCOT provided Histone H2A as a solution for the band observed at around 15 kDa (score = 60), but MS/MS on the different peaks observed were inconclusive and we were unable to reproduce that result.

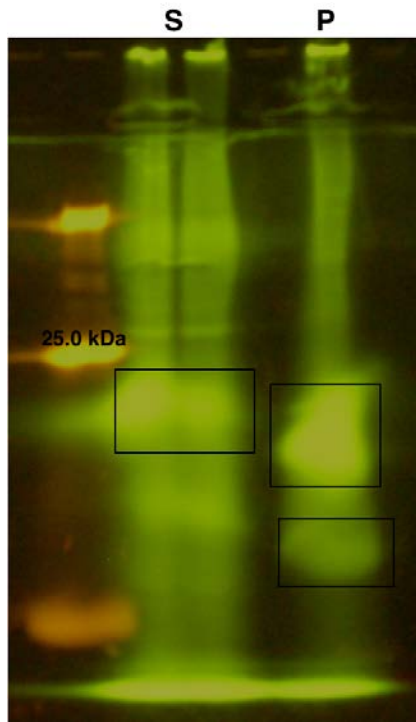


Figure 5-14: SDS-PAGE corresponding to substrate profiling experiment. The samples were run after acetone precipitation, P corresponds to the pellet and S the supernatant. The black boxes indicate the bands analyzed by mass fingerprinting.

5.4 Conclusion

The crystal structure of Eis was successfully solved. This structure confirmed the previous hypothesis that Eis is a member of the GCN5 superfamily of N-acetyltransferases (GNAT): the acetyl moiety from AcCoA is transferred to an amine of an acetyl acceptor. Although the protein was co-crystallized in presence of CoA and an acetyl acceptor, we were unable to resolve any density for CoA. Tsodikova and co-workers published the structure of Eis with CoA resolved in 2011¹⁹². They hypothesized that Eis plays a role in the aminoglycoside resistance in TB and acetylates one or several amine(s) of common aminoglycosides¹⁹⁷⁻²⁰³. However, this hypothesis does not explain how Eis promotes the intracellular survival of *M.tb* within the macrophages or how it regulates the immune response in all *M. tb* strains.

In order to identify the molecular function of Eis in TB pathogenesis and its co-substrate(s), potentially a peptide or a protein present in human macrophages, several experiments were attempted. A bisubstrate inhibitor approach, as well as a substrate profiling experiment, was carried out in human macrophage lysates. The latter experiment led to the identification of human Histone H2A as a potential acetyl acceptor of Eis. However, attempts to reproduce this result or further characterize the reaction between AcCoA and human histone(s) in presence of Eis were inconclusive.

More recently, Kim *et al.* published a study that demonstrates Eis acetylates a lysine (K55) of dual-specificity protein phosphatase 16 (DUSP-16)/mitogen-activated protein kinase phosphatase-7 (MKP-7), a JNK-specific phosphatase²⁰⁴. They showed that the acetylation of K55 by Eis leads to the suppression of LPS-induced JNK

phosphorylation. The inactivation of JNK phosphorylation results in a reduced production of TNF- α and IL-6, two cytokines that promote inflammation. Thus, they hypothesized that the acetylation of K55 by Eis causes the inhibition of the host innate immune response (macrophage autophagy, phagosome maturation, inflammation, ROS generation).

References

1. Zumla, A., Nahid, P., Cole, S. T. Advances in the development of new tuberculosis drugs and treatment regimens. *Nat Rev Drug Discov* 2013, **12**(5): 388-404.
2. Banerjee, A., Dubnau, E., Quemard, A., Balasubramanian, V., Um, K. S., Wilson, T., Collins, D., de Lisle, G., Jacobs, W. R., Jr. *inhA*, a gene encoding a target for isoniazid and ethionamide in *Mycobacterium tuberculosis*. *Science* 1994, **263**(5144): 227-230.
3. Hazbon, M. H., Brimacombe, M., Bobadilla del Valle, M., Cavatore, M., Guerrero, M. I., Varma-Basil, M., Billman-Jacobe, H., Lavender, C., Fyfe, J., Garcia-Garcia, L., Leon, C. I., Bose, M., Chaves, F., Murray, M., Eisenach, K. D., Sifuentes-Osornio, J., Cave, M. D., Ponce de Leon, A., Alland, D. Population genetics study of isoniazid resistance mutations and evolution of multidrug-resistant *Mycobacterium tuberculosis*. *Antimicrob Agents Chemother* 2006, **50**(8): 2640-2649.
4. Calvori, C., Frontali, L., Leoni, L., Tecce, G. Effect of rifamycin on protein synthesis. *Nature* 1965, **207**(995): 417-418.
5. Burman, W. J., Gallicano, K., Peloquin, C. Comparative pharmacokinetics and pharmacodynamics of the rifamycin antibacterials. *Clin Pharmacokinet* 2001, **40**(5): 327-341.
6. Gillespie, S. H. Evolution of drug resistance in *Mycobacterium tuberculosis*: clinical and molecular perspective. *Antimicrob Agents Chemother* 2002, **46**(2): 267-274.

7. Scorpio, A., Zhang, Y. Mutations in *pncA*, a gene encoding pyrazinamidase/nicotinamidase, cause resistance to the antituberculous drug pyrazinamide in tubercle bacillus. *Nat Med* 1996, **2**(6): 662-667.
8. Zhang, Y., Wade, M. M., Scorpio, A., Zhang, H., Sun, Z. Mode of action of pyrazinamide: disruption of Mycobacterium tuberculosis membrane transport and energetics by pyrazinoic acid. *J Antimicrob Chemother* 2003, **52**(5): 790-795.
9. Wolucka, B. A., McNeil, M. R., de Hoffmann, E., Chojnacki, T., Brennan, P. J. Recognition of the lipid intermediate for arabinogalactan/arabinomannan biosynthesis and its relation to the mode of action of ethambutol on mycobacteria. *J Biol Chem* 1994, **269**(37): 23328-23335.
10. Mikusova, K., Slayden, R. A., Besra, G. S., Brennan, P. J. Biogenesis of the mycobacterial cell wall and the site of action of ethambutol. *Antimicrob Agents Chemother* 1995, **39**(11): 2484-2489.
11. Telenti, A., Philipp, W. J., Sreevatsan, S., Bernasconi, C., Stockbauer, K. E., Wieles, B., Musser, J. M., Jacobs, W. R., Jr. The *emb* operon, a gene cluster of Mycobacterium tuberculosis involved in resistance to ethambutol. *Nat Med* 1997, **3**(5): 567-570.
12. Belanger, A. E., Besra, G. S., Ford, M. E., Mikusova, K., Belisle, J. T., Brennan, P. J., Inamine, J. M. The *embAB* genes of Mycobacterium avium encode an arabinosyl transferase involved in cell wall arabinan biosynthesis that is the target for the antimycobacterial drug ethambutol. *Proc Natl Acad Sci U S A* 1996, **93**(21): 11919-11924.
13. Bogen, E., Loomis, R. N., Will, D. W. Para-aminosalicylic acid treatment of tuberculosis; a review. *Am Rev Tuberc* 1950, **61**(2): 226-246.

14. Rengarajan, J., Sasseti, C. M., Naroditskaya, V., Sloutsky, A., Bloom, B. R., Rubin, E. J. The folate pathway is a target for resistance to the drug para-aminosalicylic acid (PAS) in mycobacteria. *Mol Microbiol* 2004, **53**(1): 275-282.
15. Chakraborty, S., Gruber, T., Barry, C. E., 3rd, Boshoff, H. I., Rhee, K. Y. Para-aminosalicylic acid acts as an alternative substrate of folate metabolism in *Mycobacterium tuberculosis*. *Science* 2013, **339**(6115): 88-91.
16. Schatz, A., Bugie, E., Waksman, S. A. Streptomycin, a substance exhibiting antibiotic activity against gram-positive and gram-negative bacteria. 1944. *Clin Orthop Relat Res* 2005(437): 3-6.
17. Marshall, G. Streptomycin in the treatment of pulmonary tuberculosis. . *BMJ* 1948, **2**(4582): 769-782.
18. Finken, M., Kirschner, P., Meier, A., Wrede, A., Bottger, E. C. Molecular basis of streptomycin resistance in *Mycobacterium tuberculosis*: alterations of the ribosomal protein S12 gene and point mutations within a functional 16S ribosomal RNA pseudoknot. *Mol Microbiol* 1993, **9**(6): 1239-1246.
19. Baulard, A. R., Betts, J. C., Engohang-Ndong, J., Quan, S., McAdam, R. A., Brennan, P. J., Locht, C., Besra, G. S. Activation of the pro-drug ethionamide is regulated in mycobacteria. *J Biol Chem* 2000, **275**(36): 28326-28331.
20. DeBarber, A. E., Mdluli, K., Bosman, M., Bekker, L. G., Barry, C. E., 3rd. Ethionamide activation and sensitivity in multidrug-resistant *Mycobacterium tuberculosis*. *Proc Natl Acad Sci U S A* 2000, **97**(17): 9677-9682.
21. Sirgel, F. A., Warren, R. M., Streicher, E. M., Victor, T. C., van Helden, P. D., Bottger, E. C. gyrA mutations and phenotypic susceptibility levels to ofloxacin and moxifloxacin in clinical isolates of *Mycobacterium tuberculosis*. *J Antimicrob Chemother* 2012, **67**(5): 1088-1093.

22. Sirgel, F. A., Tait, M., Warren, R. M., Streicher, E. M., Bottger, E. C., van Helden, P. D., Gey van Pittius, N. C., Coetzee, G., Hoosain, E. Y., Chabula-Nxiweni, M., Hayes, C., Victor, T. C., Trollip, A. Mutations in the rrs A1401G gene and phenotypic resistance to amikacin and capreomycin in *Mycobacterium tuberculosis*. *Microb Drug Resist* 2012, **18**(2): 193-197.
23. Favrot, L., Ronning, D. R. Targeting the mycobacterial envelope for tuberculosis drug development. *Expert Rev Anti Infect Ther* 2012, **10**(9): 1023-1036.
24. Salian, S., Matt, T., Akbergenov, R., Harish, S., Meyer, M., Duscha, S., Shcherbakov, D., Bernet, B. B., Vasella, A., Westhof, E., Bottger, E. C. Structure-activity relationships among the kanamycin aminoglycosides: role of ring I hydroxyl and amino groups. *Antimicrob Agents Chemother* 2012, **56**(12): 6104-6108.
25. Bruning, J. B., Murillo, A. C., Chacon, O., Barletta, R. G., Sacchettini, J. C. Structure of the *Mycobacterium tuberculosis* D-alanine:D-alanine ligase, a target of the antituberculosis drug D-cycloserine. *Antimicrob Agents Chemother* 2011, **55**(1): 291-301.
26. WHO. Global Tuberculosis report 2013. Geneva, Switzerland; 2013.
27. Kaufmann, S. H. How can immunology contribute to the control of tuberculosis? *Nat Rev Immunol* 2001, **1**(1): 20-30.
28. Aderem, A., Underhill, D. M. Mechanisms of phagocytosis in macrophages. *Annu Rev Immunol* 1999, **17**: 593-623.
29. Meena, L. S., Rajni. Survival mechanisms of pathogenic *Mycobacterium tuberculosis* H37Rv. *FEBS J* 2010, **277**(11): 2416-2427.
30. Ehrt, S., Schnappinger, D. Mycobacterial survival strategies in the phagosome: defence against host stresses. *Cell Microbiol* 2009, **11**(8): 1170-1178.

31. Pieters, J. Mycobacterium tuberculosis and the macrophage: maintaining a balance. *Cell Host Microbe* 2008, **3**(6): 399-407.
32. Fine, P. E. M., Carneiro, I. A. M., Milstien, J. B., Clements, C. J. Issues relating to the use of BCG in immunization programmes. Geneva, Switzerland: World Health Organisation; 1999.
33. Iseman, M. D. Treatment of multidrug-resistant tuberculosis. *N Engl J Med* 1993, **329**(11): 784-791.
34. van den Boogaard, J., Kibiki, G. S., Kisanga, E. R., Boeree, M. J., Aarnoutse, R. E. New drugs against tuberculosis: problems, progress, and evaluation of agents in clinical development. *Antimicrob Agents Chemother* 2009, **53**(3): 849-862.
35. Loewenberg, S. India reports cases of totally drug-resistant tuberculosis. *Lancet* 2012, **379**(9812): 205.
36. Shankar, E. M., Vignesh, R., Ellegard, R., Barathan, M., Chong, Y. K., Bador, M. K., Rukumani, D. V., Sabet, N. S., Kamarulzaman, A., Velu, V., Larsson, M. HIV-Mycobacterium tuberculosis co-infection: a 'danger-couple model' of disease pathogenesis. *Pathog Dis* 2014, **70**(2): 110-118.
37. Vernon, A., Burman, W., Benator, D., Khan, A., Bozeman, L. Acquired rifamycin monoresistance in patients with HIV-related tuberculosis treated with once-weekly rifapentine and isoniazid. Tuberculosis Trials Consortium. *Lancet* 1999, **353**(9167): 1843-1847.
38. Weiner, M., Benator, D., Burman, W., Peloquin, C. A., Khan, A., Vernon, A., Jones, B., Silva-Trigo, C., Zhao, Z., Hodge, T. Association between acquired rifamycin resistance and the pharmacokinetics of rifabutin and isoniazid among patients with HIV and tuberculosis. *Clin Infect Dis* 2005, **40**(10): 1481-1491.

39. Boule, A., Van Cutsem, G., Cohen, K., Hilderbrand, K., Mathee, S., Abrahams, M., Goemaere, E., Coetzee, D., Maartens, G. Outcomes of nevirapine- and efavirenz-based antiretroviral therapy when coadministered with rifampicin-based antitubercular therapy. *JAMA* 2008, **300**(5): 530-539.
40. Herzog, H. History of tuberculosis. *Respiration* 1998, **65**(1): 5-15.
41. Sakamoto, K. The pathology of Mycobacterium tuberculosis infection. *Vet Pathol* 2012, **49**(3): 423-439.
42. Ventura, M., Canchaya, C., Tauch, A., Chandra, G., Fitzgerald, G. F., Chater, K. F., van Sinderen, D. Genomics of Actinobacteria: tracing the evolutionary history of an ancient phylum. *Microbiol Mol Biol Rev* 2007, **71**(3): 495-548.
43. Brosch, R., Gordon, S. V., Marmiesse, M., Brodin, P., Buchrieser, C., Eiglmeier, K., Garnier, T., Gutierrez, C., Hewinson, G., Kremer, K., Parsons, L. M., Pym, A. S., Samper, S., van Soolingen, D., Cole, S. T. A new evolutionary scenario for the Mycobacterium tuberculosis complex. *Proc Natl Acad Sci U S A* 2002, **99**(6): 3684-3689.
44. Gutierrez, M. C., Brisse, S., Brosch, R., Fabre, M., Omais, B., Marmiesse, M., Supply, P., Vincent, V. Ancient origin and gene mosaicism of the progenitor of Mycobacterium tuberculosis. *PLoS Pathog* 2005, **1**(1): e5.
45. Daffe, M., Draper, P. The Envelope Layers of Mycobacteria with Reference to their Pathogenicity. *Advances in Microbial Physiology* 1997, **39**: 131.
46. Ernst, J. D. Macrophage receptors for Mycobacterium tuberculosis. *Infect Immun* 1998, **66**(4): 1277-1281.
47. Killick, K. E., Ni Cheallaigh, C., O'Farrelly, C., Hokamp, K., MacHugh, D. E., Harris, J. Receptor-mediated recognition of mycobacterial pathogens. *Cell Microbiol* 2013, **15**(9): 1484-1495.

48. Brennan, P. J. Structure, function, and biogenesis of the cell wall of *Mycobacterium tuberculosis*. *Tuberculosis (Edinb)* 2003, **83**(1-3): 91-97.
49. Lowary, T. L. Recent progress towards the identification of inhibitors of mycobacterial cell wall polysaccharide biosynthesis. *Mini Rev Med Chem* 2003, **3**(7): 689-702.
50. Schroeder, E. K., de Souza, N., Santos, D. S., Blanchard, J. S., Basso, L. A. Drugs that inhibit mycolic acid biosynthesis in *Mycobacterium tuberculosis*. *Curr Pharm Biotechnol* 2002, **3**(3): 197-225.
51. Crick, D. C., Brennan, P. J. *Biosynthesis of the arabinogalactan-peptidoglycan complex of Mycobacterium tuberculosis*. Amer Soc Microbiology, 1752 N Street Nw, Washington, Dc 20036-2904 USA, 2008.
52. Dover, L. G., Alderwick, L. J., Brown, A. K., Futterer, K., Besra, G. S. Regulation of cell wall synthesis and growth. *Curr Mol Med* 2007, **7**(3): 247-276.
53. Kaur, D., Guerin, M. E., Skovierova, H., Brennan, P. J., Jackson, M. Chapter 2: Biogenesis of the cell wall and other glycoconjugates of *Mycobacterium tuberculosis*. *Adv Appl Microbiol* 2009, **69**: 23-78.
54. Gilleron, M., Jackson, M., Nigou, J., Puzo, G. *Structure, biosynthesis, and activities of the phosphatidyl-myo-inositol-based lipoglycans*. Amer Soc Microbiology, 1752 N Street Nw, Washington, Dc 20036-2904 USA, 2008.
55. Song, H., Sandie, R., Wang, Y., Andrade-Navarro, M. A., Niederweis, M. Identification of outer membrane proteins of *Mycobacterium tuberculosis*. *Tuberculosis (Edinb)* 2008, **88**(6): 526-544.

56. Jarlier, V., Nikaido, H. Mycobacterial cell wall: structure and role in natural resistance to antibiotics. *FEMS Microbiol Lett* 1994, **123**(1-2): 11-18.
57. Brennan, P. J., Crick, D. C. The cell-wall core of *Mycobacterium tuberculosis* in the context of drug discovery. *Curr Top Med Chem* 2007, **7**(5): 475-488.
58. Jackson, M., McNeil, M. R., Brennan, P. J. Progress in targeting cell envelope biogenesis in *Mycobacterium tuberculosis*. *Future Microbiol* 2013, **8**(7): 855-875.
59. Tahlan, K., Wilson, R., Kastrinsky, D. B., Arora, K., Nair, V., Fischer, E., Barnes, S. W., Walker, J. R., Alland, D., Barry, C. E., 3rd, Boshoff, H. I. SQ109 Targets MmpL3, a Membrane Transporter of Trehalose Monomycolate Involved in Mycolic Acid Donation to the Cell Wall Core of *Mycobacterium tuberculosis*. *Antimicrob Agents Chemother* 2012, **56**(4): 1797-1809.
60. Matsumoto, M., Hashizume, H., Tomishige, T., Kawasaki, M., Tsubouchi, H., Sasaki, H., Shimokawa, Y., Komatsu, M. OPC-67683, a nitro-dihydroimidazooxazole derivative with promising action against tuberculosis in vitro and in mice. *PLoS Med* 2006, **3**(11): e466.
61. Stover, C. K., Warrener, P., VanDevanter, D. R., Sherman, D. R., Arain, T. M., Langhorne, M. H., Anderson, S. W., Towell, J. A., Yuan, Y., McMurray, D. N., Kreiswirth, B. N., Barry, C. E., Baker, W. R. A small-molecule nitroimidazopyran drug candidate for the treatment of tuberculosis. *Nature* 2000, **405**(6789): 962-966.
62. Makarov, V., Manina, G., Mikusova, K., Mollmann, U., Ryabova, O., Saint-Joanis, B., Dhar, N., Pasca, M. R., Buroni, S., Lucarelli, A. P., Milano, A., De Rossi, E., Belanova, M., Bobovska, A., Dianiskova, P., Kordulakova, J., Sala, C., Fullam, E., Schneider, P., McKinney, J. D., Brodin, P., Christophe, T., Waddell, S., Butcher, P., Albrethsen, J., Rosenkrands, I., Brosch, R., Nandi, V., Bharath, S., Gaonkar, S., Shandil, R. K., Balasubramanian, V., Balganes, T., Tyagi, S., Grosset, J., Riccardi, G., Cole, S. T. Benzothiazinones kill *Mycobacterium tuberculosis* by blocking arabinan synthesis. *Science* 2009, **324**(5928): 801-804.

63. Harth, G., Lee, B. Y., Wang, J., Clemens, D. L., Horwitz, M. A. Novel insights into the genetics, biochemistry, and immunocytochemistry of the 30-kilodalton major extracellular protein of *Mycobacterium tuberculosis*. *Infect Immun* 1996, **64**(8): 3038-3047.
64. Belisle, J. T., Vissa, V. D., Sievert, T., Takayama, K., Brennan, P. J., Besra, G. S. Role of the major antigen of *Mycobacterium tuberculosis* in cell wall biogenesis. *Science* 1997, **276**(5317): 1420-1422.
65. Jackson, M., Raynaud, C., Laneelle, M. A., Guilhot, C., Laurent-Winter, C., Ensergueix, D., Gicquel, B., Daffe, M. Inactivation of the antigen 85C gene profoundly affects the mycolate content and alters the permeability of the *Mycobacterium tuberculosis* cell envelope. *Mol Microbiol* 1999, **31**(5): 1573-1587.
66. Sanki, A. K., Boucau, J., Ronning, D. R., Sucheck, S. J. Antigen 85C-mediated acyl-transfer between synthetic acyl donors and fragments of the arabinan. *Glycoconj J* 2009, **26**(5): 589-596.
67. Nguyen, L., Chinnapapagari, S., Thompson, C. J. FbpA-Dependent biosynthesis of trehalose dimycolate is required for the intrinsic multidrug resistance, cell wall structure, and colonial morphology of *Mycobacterium smegmatis*. *J Bacteriol* 2005, **187**(19): 6603-6611.
68. Matsunaga, I., Naka, T., Talekar, R. S., McConnell, M. J., Katoh, K., Nakao, H., Otsuka, A., Behar, S. M., Yano, I., Moody, D. B., Sugita, M. Mycolyltransferase-mediated glycolipid exchange in *Mycobacteria*. *J Biol Chem* 2008, **283**(43): 28835-28841.
69. Armitige, L. Y., Jagannath, C., Wanger, A. R., Norris, S. J. Disruption of the genes encoding antigen 85A and antigen 85B of *Mycobacterium tuberculosis* H37Rv: effect on growth in culture and in macrophages. *Infect Immun* 2000, **68**(2): 767-778.

70. Ronning, D. R., Klabunde, T., Besra, G. S., Vissa, V. D., Belisle, J. T., Sacchettini, J. C. Crystal structure of the secreted form of antigen 85C reveals potential targets for mycobacterial drugs and vaccines. *Nat Struct Biol* 2000, **7**(2): 141-146.
71. Anderson, D. H., Harth, G., Horwitz, M. A., Eisenberg, D. An interfacial mechanism and a class of inhibitors inferred from two crystal structures of the *Mycobacterium tuberculosis* 30 kDa major secretory protein (Antigen 85B), a mycolyl transferase. *J Mol Biol* 2001, **307**(2): 671-681.
72. Ronning, D. R., Vissa, V., Besra, G. S., Belisle, J. T., Sacchettini, J. C. *Mycobacterium tuberculosis* antigen 85A and 85C structures confirm binding orientation and conserved substrate specificity. *J Biol Chem* 2004, **279**(35): 36771-36777.
73. da Silva, P. E., Von Groll, A., Martin, A., Palomino, J. C. Efflux as a mechanism for drug resistance in *Mycobacterium tuberculosis*. *FEMS Immunol Med Microbiol* 2011, **63**(1): 1-9.
74. Harth, G., Zamecnik, P. C., Tabatadze, D., Pierson, K., Horwitz, M. A. Hairpin extensions enhance the efficacy of mycolyl transferase-specific antisense oligonucleotides targeting *Mycobacterium tuberculosis*. *Proc Natl Acad Sci U S A* 2007, **104**(17): 7199-7204.
75. Rose, J. D., Maddry, J. A., Comber, R. N., Suling, W. J., Wilson, L. N., Reynolds, R. C. Synthesis and biological evaluation of trehalose analogs as potential inhibitors of mycobacterial cell wall biosynthesis. *Carbohydr Res* 2002, **337**(2): 105-120.
76. Wang, J., Elchert, B., Hui, Y., Takemoto, J. Y., Bensaci, M., Wennergren, J., Chang, H., Rai, R., Chang, C. W. Synthesis of trehalose-based compounds and their inhibitory activities against *Mycobacterium smegmatis*. *Bioorg Med Chem* 2004, **12**(24): 6397-6413.

77. Sanki, A. K., Boucau, J., Umesiri, F. E., Ronning, D. R., Sucheck, S. J. Design, synthesis and biological evaluation of sugar-derived esters, alpha-ketoesters and alpha-ketoamides as inhibitors for Mycobacterium tuberculosis antigen 85C. *Mol Biosyst* 2009, **5**(9): 945-956.
78. Ibrahim, D. A., Boucau, J., Lajiness, D. H., Veleti, S. K., Trabbic, K. R., Adams, S. S., Ronning, D. R., Sucheck, S. J. Design, Synthesis, and X-ray Analysis of a Glycoconjugate Bound to Mycobacterium tuberculosis Antigen 85C. *Bioconjug Chem* 2012.
79. Gobec, S., Plantan, I., Mravljak, J., Wilson, R. A., Besra, G. S., Kikelj, D. Phosphonate inhibitors of antigen 85C, a crucial enzyme involved in the biosynthesis of the Mycobacterium tuberculosis cell wall. *Bioorg Med Chem Lett* 2004, **14**(13): 3559-3562.
80. Kovac, A., Wilson, R. A., Besra, G. S., Filipic, M., Kikelj, D., Gobec, S. New lipophilic phthalimido- and 3-phenoxybenzyl sulfonates: inhibition of antigen 85C mycolyltransferase activity and cytotoxicity. *J Enzyme Inhib Med Chem* 2006, **21**(4): 391-397.
81. Gobec, S., Plantan, I., Mravljak, J., Svajger, U., Wilson, R. A., Besra, G. S., Soares, S. L., Appelberg, R., Kikelj, D. Design, synthesis, biochemical evaluation and antimycobacterial action of phosphonate inhibitors of antigen 85C, a crucial enzyme involved in biosynthesis of the mycobacterial cell wall. *Eur J Med Chem* 2007, **42**(1): 54-63.
82. Elamin, A. A., Stehr, M., Oehlmann, W., Singh, M. The mycolyltransferase 85A, a putative drug target of Mycobacterium tuberculosis: development of a novel assay and quantification of glycolipid-status of the mycobacterial cell wall. *J Microbiol Methods* 2009, **79**(3): 358-363.
83. Boucau, J., Sanki, A. K., Voss, B. J., Sucheck, S. J., Ronning, D. R. A coupled assay measuring Mycobacterium tuberculosis antigen 85C enzymatic activity. *Anal Biochem* 2009, **385**(1): 120-127.

84. Sanki, A. K., Boucau, J., Srivastava, P., Adams, S. S., Ronning, D. R., Sucheck, S. J. Synthesis of methyl 5-S-alkyl-5-thio-D-arabinofuranosides and evaluation of their antimycobacterial activity. *Bioorg Med Chem* 2008, **16**(10): 5672-5682.
85. Barry, C. S., Backus, K. M., Barry, C. E., 3rd, Davis, B. G. ESI-MS assay of M. tuberculosis cell wall antigen 85 enzymes permits substrate profiling and design of a mechanism-based inhibitor. *J Am Chem Soc* 2011, **133**(34): 13232-13235.
86. Warriar, T., Tropis, M., Werngren, J., Diehl, A., Gengenbacher, M., Schlegel, B., Schade, M., Oschkinat, H., Daffe, M., Hoffner, S., Eddine, A. N., Kaufmann, S. H. Antigen 85C Inhibition Restricts Mycobacterium tuberculosis Growth through Disruption of Cord Factor Biosynthesis. *Antimicrob Agents Chemother* 2012, **56**(4): 1735-1743.
87. Lajiness, D. H. Trehalose Monomycolate Biosynthesis and Utilization in *Mycobacterium tuberculosis*. University of Toledo, 2011.
88. Favrot, L., Grzegorzewicz, A. E., Lajiness, D. H., Marvin, R. K., Boucau, J., Isailovic, D., Jackson, M., Ronning, D. R. Mechanism of inhibition of Mycobacterium tuberculosis antigen 85 by ebselen. *Nat Commun* 2013, **4**: 2748.
89. Zhang, J., Chung, T. D. Y., Oldenburg, K. R. A simple statistical parameter for use in evaluation and validation of high throughput screening assays. *Journal of Biomolecular Screening* 1999, **4**(2): 67-73.
90. Boucau, J. Enzymatic and Structural Characterization of Proteins Linked to *Mycobacterium tuberculosis* Pathogenicity. University of Toledo, 2008.
91. Gasteiger E, H. C., Gattiker A, Duvaud S, Wilkins MR, Appel RD, Bairoch A. Protein identification and analysis tools on the ExPASy server. In: Walker, J. M. (ed). *The proteomics protocols handbook*. Humana Press Inc: Totowa, NJ, 2005, pp 571-607.

92. Otwinowski, Z., Minor, W. Processing of X-ray diffraction data collected in oscillation mode. *Methods Enzymology* 1997, **27**: 307-326.
93. Kissinger, C. R., Gehlhaar, D. K., Fogel, D. B. Rapid automated molecular replacement by evolutionary search. *Acta Crystallogr D Biol Crystallogr* 1999, **55**(Pt 2): 484-491.
94. Kissinger, C. R., Gehlhaar, D. K., Smith, B. A., Bouzida, D. Molecular replacement by evolutionary search. *Acta Crystallogr D Biol Crystallogr* 2001, **57**(Pt 10): 1474-1479.
95. Adams, P. D., Afonine, P. V., Bunkoczi, G., Chen, V. B., Davis, I. W., Echols, N., Headd, J. J., Hung, L. W., Kapral, G. J., Grosse-Kunstleve, R. W., McCoy, A. J., Moriarty, N. W., Oeffner, R., Read, R. J., Richardson, D. C., Richardson, J. S., Terwilliger, T. C., Zwart, P. H. PHENIX: a comprehensive Python-based system for macromolecular structure solution. *Acta Crystallogr D Biol Crystallogr* 2010, **66**(Pt 2): 213-221.
96. Emsley, P., Lohkamp, B., Scott, W. G., Cowtan, K. Features and development of Coot. *Acta Crystallogr D Biol Crystallogr* 2010, **66**(Pt 4): 486-501.
97. Lu, J., Vlamis-Gardikas, A., Kandasamy, K., Zhao, R., Gustafsson, T. N., Engstrand, L., Hoffner, S., Engman, L., Holmgren, A. Inhibition of bacterial thioredoxin reductase: an antibiotic mechanism targeting bacteria lacking glutathione. *FASEB J* 2013, **27**(4): 1394-1403.
98. Holmgren, A., Masayasu, H., Zhao, R. Ebselen: A drug targeting thioredoxin and thioredoxin reductase. *Free Radical Biology and Medicine* 2002, **33**: S93-S93.
99. Zhao, R., Holmgren, A. A novel antioxidant mechanism of ebselen involving ebselen diselenide, a substrate of mammalian thioredoxin and thioredoxin reductase. *Journal of Biological Chemistry* 2002, **277**(42): 39456-39462.

100. Nakamura, Y., Feng, Q., Kumagai, T., Torikai, K., Ohigashi, H., Osawa, T., Noguchi, N., Niki, E., Uchida, K. Ebselen, a glutathione peroxidase mimetic seleno-organic compound, as a multifunctional antioxidant. Implication for inflammation-associated carcinogenesis. *J Biol Chem* 2002, **277**(4): 2687-2694.
101. Zhao, R., Masayasu, H., Holmgren, A. Ebselen: A substrate for human thioredoxin reductase strongly stimulating its hydroperoxide reductase activity and a superfast thioredoxin oxidant. *Proc Natl Acad Sci U S A* 2002, **99**(13): 8579-8584.
102. Sarma, B. K., Mugesh, G. Glutathione peroxidase (GPx)-like antioxidant activity of the organoselenium drug ebselen: Unexpected complications with thiol exchange reactions. *J Am Chem Soc* 2005, **127**(32): 11477-11485.
103. Hattori, R., Yui, Y., Shinoda, E., Inoue, R., Aoyama, T., Masayasu, H., Kawai, C., Sasayama, S. Effect of ebselen on bovine and rat nitric oxide synthase activity is modified by thiols. *The Japanese Journal of Pharmacology* 1996, **72**(2): 191-193.
104. Linsky, T., Wang, Y., Fast, W. Screening for Dimethylarginine Dimethylaminohydrolase Inhibitors Reveals Ebselen as a Bioavailable Inactivator. *Acs Medicinal Chemistry Letters* 2011, **2**(8): 592-596.
105. Lieberman, O. J., Orr, M. W., Wang, Y., Lee, V. T. High-Throughput Screening Using the Differential Radial Capillary Action of Ligand Assay Identifies Ebselen As an Inhibitor of Diguanylate Cyclases. *ACS Chem Biol* 2014, **9**(1): 183-192.
106. Singh, N., Halliday, A. C., Thomas, J. M., Kuznetsova, O. V., Baldwin, R., Woon, E. C., Aley, P. K., Antoniadou, I., Sharp, T., Vasudevan, S. R., Churchill, G. C. A safe lithium mimetic for bipolar disorder. *Nat Commun* 2013, **4**: 1332.
107. Terentis, A. C., Freewan, M., Plaza, T. S. S., Raftery, M. J., Stocker, R., Thomas, S. R. The Selenazal Drug Ebselen Potently Inhibits Indoleamine 2,3-Dioxygenase by Targeting Enzyme Cysteine Residues. *Biochemistry* 2010, **49**(3): 591-600.

108. Yamaguchi, T., Sano, K., Takakura, K., Saito, I., Shinohara, Y., Asano, T., Yasuhara, H., Grp, E. S. Ebselen in acute ischemic stroke - A placebo-controlled, double-blind clinical trial. *Stroke* 1998, **29**(1): 12-17.
109. Parnham, M., Sies, H. Ebselen: prospective therapy for cerebral ischaemia. *Expert Opinion on Investigational Drugs* 2000, **9**(3): 607-619.
110. Azad, G. K., Balkrishna, S. J., Sathish, N., Kumar, S., Tomar, R. S. Multifunctional Ebselen drug functions through the activation of DNA damage response and alterations in nuclear proteins. *Biochem Pharmacol* 2012, **83**(2): 296-303.
111. Azad, G. K., Singh, V., Mandal, P., Singh, P., Golla, U., Baranwal, S., Chauhan, S., Tomar, R. S. Ebselen induces reactive oxygen species (ROS)-mediated cytotoxicity in *Saccharomyces cerevisiae* with inhibition of glutamate dehydrogenase being a target. *FEBS Open Bio* 2014, **4**: 77-89.
112. Xu, K., Zhang, Y., Tang, B., Laskin, J., Roach, P. J., Chen, H. Study of highly selective and efficient thiol derivatization using selenium reagents by mass spectrometry. *Anal Chem* 2010, **82**(16): 6926-6932.
113. Trefzer, C., Rengifo-Gonzalez, M., Hinner, M. J., Schneider, P., Makarov, V., Cole, S. T., Johnsson, K. Benzothiazinones: prodrugs that covalently modify the decaprenylphosphoryl-beta-D-ribose 2'-epimerase DprE1 of *Mycobacterium tuberculosis*. *J Am Chem Soc* 2010, **132**(39): 13663-13665.
114. Trefzer, C., Skovierova, H., Buroni, S., Bobovska, A., Nenci, S., Molteni, E., Pojer, F., Pasca, M. R., Makarov, V., Cole, S. T., Riccardi, G., Mikusova, K., Johnsson, K. Benzothiazinones are suicide inhibitors of mycobacterial decaprenylphosphoryl-beta-D-ribofuranose 2'-oxidase DprE1. *J Am Chem Soc* 2012, **134**(2): 912-915.

115. Batt, S. M., Jabeen, T., Bhowruth, V., Quill, L., Lund, P. A., Eggeling, L., Alderwick, L. J., Futterer, K., Besra, G. S. Structural basis of inhibition of Mycobacterium tuberculosis DprE1 by benzothiazinone inhibitors. *Proc Natl Acad Sci U S A* 2012, **109**(28): 11354-11359.
116. Kremer, L., Maughan, W. N., Wilson, R. A., Dover, L. G., Besra, G. S. The M. tuberculosis antigen 85 complex and mycolyltransferase activity. *Lett Appl Microbiol* 2002, **34**(4): 233-237.
117. Puech, V., Guilhot, C., Perez, E., Tropis, M., Armitige, L. Y., Gicquel, B., Daffe, M. Evidence for a partial redundancy of the fibronectin-binding proteins for the transfer of mycoloyl residues onto the cell wall arabinogalactan termini of Mycobacterium tuberculosis. *Mol Microbiol* 2002, **44**(4): 1109-1122.
118. Wilson, R. A., Maughan, W. N., Kremer, L., Besra, G. S., Futterer, K. The structure of Mycobacterium tuberculosis MPT51 (FbpC1) defines a new family of non-catalytic alpha/beta hydrolases. *J Mol Biol* 2004, **335**(2): 519-530.
119. Burmeister, W. P. Structural changes in a cryo-cooled protein crystal owing to radiation damage. *Acta Crystallogr D Biol Crystallogr* 2000, **56**(Pt 3): 328-341.
120. Carugo, O., Djinovic Carugo, K. When X-rays modify the protein structure: radiation damage at work. *Trends Biochem Sci* 2005, **30**(4): 213-219.
121. Leiros, H. K., McSweeney, S. M., Smalas, A. O. Atomic resolution structures of trypsin provide insight into structural radiation damage. *Acta Crystallogr D Biol Crystallogr* 2001, **57**(Pt 4): 488-497.
122. Ravelli, R. B., McSweeney, S. M. The 'fingerprint' that X-rays can leave on structures. *Structure* 2000, **8**(3): 315-328.
123. Weik, M., Ravelli, R. B., Kryger, G., McSweeney, S., Raves, M. L., Harel, M., Gros, P., Silman, I., Kroon, J., Sussman, J. L. Specific chemical and structural

damage to proteins produced by synchrotron radiation. *Proc Natl Acad Sci U S A* 2000, **97**(2): 623-628.

124. Moriarty, N. W., Grosse-Kunstleve, R. W., Adams, P. D. electronic Ligand Builder and Optimization Workbench (eLBOW): a tool for ligand coordinate and restraint generation. *Acta Crystallogr D Biol Crystallogr* 2009, **65**(Pt 10): 1074-1080.
125. Craik, C. S., Rocznik, S., Largman, C., Rutter, W. J. The catalytic role of the active site aspartic acid in serine proteases. *Science* 1987, **237**(4817): 909-913.
126. Sprang, S., Standing, T., Fletterick, R. J., Stroud, R. M., Finer-Moore, J., Xuong, N. H., Hamlin, R., Rutter, W. J., Craik, C. S. The three-dimensional structure of Asn102 mutant of trypsin: role of Asp102 in serine protease catalysis. *Science* 1987, **237**(4817): 905-909.
127. Backus, K. M., Boshoff, H. I., Barry, C. S., Boutureira, O., Patel, M. K., D'Hooge, F., Lee, S. S., Via, L. E., Tahlan, K., Barry, C. E., 3rd, Davis, B. G. Uptake of unnatural trehalose analogs as a reporter for Mycobacterium tuberculosis. *Nat Chem Biol* 2011, **7**(4): 228-235.
128. Nelson, D. L., Cox, M. M. The Citric Cycle (Chapter 16). *Lehninger Principles of Biochemistry, Sixth Edition*. W. H. Freeman and Company: United States, 2013.
129. Nobel Lectures. *Physiology or medicine 1942-1962*. Elsevier Publishing Company: Amsterdam, 1964.
130. Remington, S., Wiegand, G., Huber, R. Crystallographic refinement and atomic models of two different forms of citrate synthase at 2.7 and 1.7 Å resolution. *J Mol Biol* 1982, **158**(1): 111-152.

131. Karpusas, M., Branchaud, B., Remington, S. J. Proposed Mechanism for the Condensation Reaction of Citrate Synthase - 1.9-Å Structure of the Ternary Complex with Oxaloacetate and Carboxymethyl Coenzyme-A. *Biochemistry* 1990, **29**(9): 2213-2219.
132. Karpusas, M., Holland, D., Remington, S. J. 1.9-Å Structures of Ternary Complexes of Citrate Synthase with D-Malate and L-Malate - Mechanistic Implications. *Biochemistry* 1991, **30**(24): 6024-6031.
133. Liao, D. I., Karpusas, M., Remington, S. J. Crystal-Structure of an Open Conformation of Citrate Synthase from Chicken Heart at 2.8-Å Resolution. *Biochemistry* 1991, **30**(24): 6031-6036.
134. Remington, S. J. Structure and mechanism of citrate synthase. *Curr Top Cell Regul* 1992, **33**: 209-229.
135. Russell, R. J., Ferguson, J. M., Hough, D. W., Danson, M. J., Taylor, G. L. The crystal structure of citrate synthase from the hyperthermophilic archaeon *pyrococcus furiosus* at 1.9 Å resolution. *Biochemistry* 1997, **36**(33): 9983-9994.
136. Francois, J. A., Starks, C. M., Sivanuntakorn, S., Jiang, H., Ransome, A. E., Nam, J. W., Constantine, C. Z., Kappock, T. J. Structure of a NADH-insensitive hexameric citrate synthase that resists acid inactivation. *Biochemistry* 2006, **45**(45): 13487-13499.
137. Maurus, R., Nguyen, N. T., Stokell, D. J., Ayed, A., Hultin, P. G., Duckworth, H. W., Brayer, G. D. Insights into the evolution of allosteric properties. The NADH binding site of hexameric type II citrate synthases. *Biochemistry* 2003, **42**(19): 5555-5565.
138. Nguyen, N. T., Maurus, R., Stokell, D. J., Ayed, A., Duckworth, H. W., Brayer, G. D. Comparative analysis of folding and substrate binding sites between regulated hexameric type II citrate synthases and unregulated dimeric type I enzymes. *Biochemistry* 2001, **40**(44): 13177-13187.

139. Stokell, D. J., Donald, L. J., Maurus, R., Nguyen, N. T., Sadler, G., Choudhary, K., Hultin, P. G., Brayer, G. D., Duckworth, H. W. Probing the roles of key residues in the unique regulatory NADH binding site of type II citrate synthase of *Escherichia coli*. *J Biol Chem* 2003, **278**(37): 35435-35443.
140. Boutz, D. R., Cascio, D., Whitelegge, J., Perry, L. J., Yeates, T. O. Discovery of a thermophilic protein complex stabilized by topologically interlinked chains. *J Mol Biol* 2007, **368**(5): 1332-1344.
141. Alter, G. M., Casazza, J. P., Zhi, W., Nemeth, P., Srere, P. A., Evans, C. T. Mutation of essential catalytic residues in pig citrate synthase. *Biochemistry* 1990, **29**(33): 7557-7563.
142. Evans, C. T., Kurz, L. C., Remington, S. J., Srere, P. A. Active site mutants of pig citrate synthase: effects of mutations on the enzyme catalytic and structural properties. *Biochemistry* 1996, **35**(33): 10661-10672.
143. Mulholland, A. J., Richards, W. G. Acetyl-CoA enolization in citrate synthase: a quantum mechanical/molecular mechanical (QM/MM) study. *Proteins* 1997, **27**(1): 9-25.
144. Donini, O., Darden, T., Kollman, P. A. QM-FE calculations of aliphatic hydrogen abstraction in citrate synthase and in solution: Reproduction of the effect of enzyme catalysis and demonstration that an enolate rather than an enol is formed. *Journal of the American Chemical Society* 2000, **122**(49): 12270-12280.
145. Mulholland, A. J., Lyne, P. D., Karplus, M. Ab initio QM/MM study of the citrate synthase mechanism. A low-barrier hydrogen bond is not involved. *Journal of the American Chemical Society* 2000, **122**(3): 534-535.

146. Anderson, D. H., Duckworth, H. W. Invitro Mutagenesis of Escherichia-Coli Citrate Synthase to Clarify the Locations of Ligand-Binding Sites. *Journal of Biological Chemistry* 1988, **263**(5): 2163-2169.
147. Kurz, L. C., Constantine, C. Z., Jiang, H., Kappock, T. J. The partial substrate dethiaacetyl-coenzyme A mimics all critical carbon acid reactions in the condensation half-reaction catalyzed by *Thermoplasma acidophilum* citrate synthase. *Biochemistry* 2009, **48**(33): 7878-7891.
148. Beard, D. A., Vinnakota, K. C., Wu, F. Detailed enzyme kinetics in terms of biochemical species: study of citrate synthase. *PLoS One* 2008, **3**(3): e1825.
149. Wiegand, G., Remington, S., Deisenhofer, J., Huber, R. Crystal structure analysis and molecular model of a complex of citrate synthase with oxaloacetate and S-acetyl-coenzyme A. *J Mol Biol* 1984, **174**(1): 205-219.
150. Wiegand, G., Remington, S. J. Citrate synthase: structure, control, and mechanism. *Annu Rev Biophys Biophys Chem* 1986, **15**: 97-117.
151. Weitzman, P. D. Regulation of citrate synthase activity in escherichia coli. *Biochim Biophys Acta* 1966, **128**(1): 213-215.
152. Weitzman, P. D. Reduced nicotinamide-adenine dinucleotide as an allosteric effector of citrate-synthase activity in Escherichia coli. *Biochem J* 1966, **101**(3): 44C-45C.
153. Guest, J. R. The Leeuwenhoek Lecture, 1995. Adaptation to life without oxygen. *Philos Trans R Soc Lond B Biol Sci* 1995, **350**(1332): 189-202.
154. Gest, H. Evolution of the Citric-Acid Cycle and Respiratory Energy-Conversion in Prokaryotes. *Fems Microbiology Letters* 1981, **12**(3): 209-215.

155. Gest, H. Evolutionary Roots of the Citric-Acid Cycle in Prokaryotes. *Biochemical Society Symposium* 1987(54): 3-16.
156. Pitson, S. M., Mendz, G. L., Srinivasan, S., Hazell, S. L. The tricarboxylic acid cycle of *Helicobacter pylori*. *Eur J Biochem* 1999, **260**(1): 258-267.
157. Hayes, C. S., Low, D. A. Signals of growth regulation in bacteria. *Curr Opin Microbiol* 2009, **12**(6): 667-673.
158. Gill, W. P., Harik, N. S., Whiddon, M. R., Liao, R. P., Mittler, J. E., Sherman, D. R. A replication clock for *Mycobacterium tuberculosis*. *Nat Med* 2009, **15**(2): 211-214.
159. Mitchison, D. A., Coates, A. R. Predictive in vitro models of the sterilizing activity of anti-tuberculosis drugs. *Curr Pharm Des* 2004, **10**(26): 3285-3295.
160. Gomez, J. E., McKinney, J. D. M. tuberculosis persistence, latency, and drug tolerance. *Tuberculosis (Edinb)* 2004, **84**(1-2): 29-44.
161. Cole, S. T., Brosch, R., Parkhill, J., Garnier, T., Churcher, C., Harris, D., Gordon, S. V., Eiglmeier, K., Gas, S., Barry, C. E., 3rd, Tekaiia, F., Badcock, K., Basham, D., Brown, D., Chillingworth, T., Connor, R., Davies, R., Devlin, K., Feltwell, T., Gentles, S., Hamlin, N., Holroyd, S., Hornsby, T., Jagels, K., Krogh, A., McLean, J., Moule, S., Murphy, L., Oliver, K., Osborne, J., Quail, M. A., Rajandream, M. A., Rogers, J., Rutter, S., Seeger, K., Skelton, J., Squares, R., Squares, S., Sulston, J. E., Taylor, K., Whitehead, S., Barrell, B. G. Deciphering the biology of *Mycobacterium tuberculosis* from the complete genome sequence. *Nature* 1998, **393**(6685): 537-544.
162. Tian, J., Bryk, R., Shi, S., Erdjument-Bromage, H., Tempst, P., Nathan, C. *Mycobacterium tuberculosis* appears to lack alpha-ketoglutarate dehydrogenase and encodes pyruvate dehydrogenase in widely separated genes. *Mol Microbiol* 2005, **57**(3): 859-868.

163. Tian, J., Bryk, R., Itoh, M., Suematsu, M., Nathan, C. Variant tricarboxylic acid cycle in *Mycobacterium tuberculosis*: identification of alpha-ketoglutarate decarboxylase. *Proc Natl Acad Sci U S A* 2005, **102**(30): 10670-10675.
164. Wagner, T., Bellinzoni, M., Wehenkel, A., O'Hare, H. M., Alzari, P. M. Functional plasticity and allosteric regulation of alpha-ketoglutarate decarboxylase in central mycobacterial metabolism. *Chem Biol* 2011, **18**(8): 1011-1020.
165. Baughn, A. D., Garforth, S. J., Vilcheze, C., Jacobs, W. R., Jr. An anaerobic-type alpha-ketoglutarate ferredoxin oxidoreductase completes the oxidative tricarboxylic acid cycle of *Mycobacterium tuberculosis*. *PLoS Pathog* 2009, **5**(11): e1000662.
166. de Carvalho, L. P., Ling, Y., Shen, C., Warren, J. D., Rhee, K. Y. On the chemical mechanism of succinic semialdehyde dehydrogenase (GabD1) from *Mycobacterium tuberculosis*. *Arch Biochem Biophys* 2011, **509**(1): 90-99.
167. Rhee, K. Y., de Carvalho, L. P., Bryk, R., Ehrt, S., Marrero, J., Park, S. W., Schnappinger, D., Venugopal, A., Nathan, C. Central carbon metabolism in *Mycobacterium tuberculosis*: an unexpected frontier. *Trends Microbiol* 2011, **19**(7): 307-314.
168. Banerjee, S., Nandyala, A., Podili, R., Katoch, V. M., Hasnain, S. E. Comparison of *Mycobacterium tuberculosis* isocitrate dehydrogenases (ICD-1 and ICD-2) reveals differences in coenzyme affinity, oligomeric state, pH tolerance and phylogenetic affiliation. *BMC Biochem* 2005, **6**: 20.
169. Quartararo, C. E., Hazra, S., Hadi, T., Blanchard, J. S. Structural, kinetic and chemical mechanism of isocitrate dehydrogenase-1 from *Mycobacterium tuberculosis*. *Biochemistry* 2013, **52**(10): 1765-1775.

170. Kumar, R., Bhakuni, V. Mycobacterium tuberculosis isocitrate lyase (MtbIcl): role of divalent cations in modulation of functional and structural properties. *Proteins* 2008, **72**(3): 892-900.
171. Moynihan, M. M., Murkin, A. S. Cysteine is the general base that serves in catalysis by isocitrate lyase and in mechanism-based inhibition by 3-nitropropionate. *Biochemistry* 2014, **53**(1): 178-187.
172. Ohman, R., Ridell, M. Purification and characterisation of isocitrate dehydrogenase and malate dehydrogenase from Mycobacterium tuberculosis and evaluation of their potential as suitable antigens for the serodiagnosis of tuberculosis. *Tuber Lung Dis* 1996, **77**(5): 454-461.
173. de Carvalho, L. P., Fischer, S. M., Marrero, J., Nathan, C., Ehrt, S., Rhee, K. Y. Metabolomics of Mycobacterium tuberculosis reveals compartmentalized co-catabolism of carbon substrates. *Chem Biol* 2010, **17**(10): 1122-1131.
174. Baek, S. H., Li, A. H., Sasseti, C. M. Metabolic regulation of mycobacterial growth and antibiotic sensitivity. *PLoS Biol* 2011, **9**(5): e1001065.
175. Ellman, G. L. Tissue sulfhydryl groups. *Arch Biochem Biophys* 1959, **82**(1): 70-77.
176. Trievel, R. C., Li, F. Y., Marmorstein, R. Application of a fluorescent histone acetyltransferase assay to probe the substrate specificity of the human p300/CBP-associated factor. *Anal Biochem* 2000, **287**(2): 319-328.
177. Riddles, P. W., Blakeley, R. L., Zerner, B. Ellman's reagent: 5,5'-dithiobis(2-nitrobenzoic acid)--a reexamination. *Anal Biochem* 1979, **94**(1): 75-81.
178. Riddles, P. W., Blakeley, R. L., Zerner, B. Reassessment of Ellman's reagent. *Methods Enzymol* 1983, **91**: 49-60.

179. Duckworth, H. W., Tong, E. K. The binding of reduced nicotinamide adenine dinucleotide to citrate synthase of *Escherichia coli* K12. *Biochemistry* 1976, **15**(1): 108-114.
180. Reed, M. C., Lieb, A., Nijhout, H. F. The biological significance of substrate inhibition: a mechanism with diverse functions. *Bioessays* 2010, **32**(5): 422-429.
181. Viollier, P. H., Minas, W., Dale, G. E., Folcher, M., Thompson, C. J. Role of acid metabolism in *Streptomyces coelicolor* morphological differentiation and antibiotic biosynthesis. *J Bacteriol* 2001, **183**(10): 3184-3192.
182. Mitchell, C. G., Anderson, S. C., el-Mansi, E. M. Purification and characterization of citrate synthase isoenzymes from *Pseudomonas aeruginosa*. *Biochem J* 1995, **309** (Pt 2): 507-511.
183. Duckworth, H. W., Nguyen, N. T., Gao, Y., Donald, L. J., Maurus, R., Ayed, A., Bruneau, B., Brayer, G. D. Enzyme-substrate complexes of allosteric citrate synthase: evidence for a novel intermediate in substrate binding. *Biochim Biophys Acta* 2013, **1834**(12): 2546-2553.
184. Wei, J., Dahl, J. L., Moulder, J. W., Roberts, E. A., O'Gaora, P., Young, D. B., Friedman, R. L. Identification of a *Mycobacterium tuberculosis* gene that enhances mycobacterial survival in macrophages. *J Bacteriol* 2000, **182**(2): 377-384.
185. Dahl, J. L., Wei, J., Moulder, J. W., Laal, S., Friedman, R. L. Subcellular localization of the intracellular survival-enhancing Eis protein of *Mycobacterium tuberculosis*. *Infect Immun* 2001, **69**(7): 4295-4302.
186. Cappelli, G., Volpe, P., Sanduzzi, A., Sacchi, A., Colizzi, V., Mariani, F. Human macrophage gamma interferon decreases gene expression but not replication of *Mycobacterium tuberculosis*: analysis of the host-pathogen reciprocal influence on transcription in a comparison of strains H37Rv and CMT97. *Infect Immun* 2001, **69**(12): 7262-7270.

187. Lella, R. K., Sharma, C. Eis (enhanced intracellular survival) protein of *Mycobacterium tuberculosis* disturbs the cross regulation of T-cells. *J Biol Chem* 2007, **282**(26): 18671-18675.
188. Samuel, L. P., Song, C. H., Wei, J., Roberts, E. A., Dahl, J. L., Barry, C. E., 3rd, Jo, E. K., Friedman, R. L. Expression, production and release of the Eis protein by *Mycobacterium tuberculosis* during infection of macrophages and its effect on cytokine secretion. *Microbiology* 2007, **153**(Pt 2): 529-540.
189. Shin, D. M., Jeon, B. Y., Lee, H. M., Jin, H. S., Yuk, J. M., Song, C. H., Lee, S. H., Lee, Z. W., Cho, S. N., Kim, J. M., Friedman, R. L., Jo, E. K. *Mycobacterium tuberculosis* eis regulates autophagy, inflammation, and cell death through redox-dependent signaling. *PLoS Pathog* 2010, **6**(12): e1001230.
190. Dyda, F., Klein, D. C., Hickman, A. B. GCN5-related N-acetyltransferases: a structural overview. *Annu Rev Biophys Biomol Struct* 2000, **29**: 81-103.
191. Zaunbrecher, M. A., Sikes, R. D., Jr., Metchock, B., Shinnick, T. M., Posey, J. E. Overexpression of the chromosomally encoded aminoglycoside acetyltransferase eis confers kanamycin resistance in *Mycobacterium tuberculosis*. *Proc Natl Acad Sci U S A* 2009, **106**(47): 20004-20009.
192. Chen, W., Biswas, T., Porter, V. R., Tsodikov, O. V., Garneau-Tsodikova, S. Unusual regioversatility of acetyltransferase Eis, a cause of drug resistance in XDR-TB. *Proc Natl Acad Sci U S A* 2011, **108**(24): 9804-9808.
193. Darley, D. J., Butler, D. S., Prideaux, S. J., Thornton, T. W., Wilson, A. D., Woodman, T. J., Threadgill, M. D., Lloyd, M. D. Synthesis and use of isotope-labelled substrates for a mechanistic study on human alpha-methylacyl-CoA racemase 1A (AMACR; P504S). *Org Biomol Chem* 2009, **7**(3): 543-552.

194. Xu, H., Hegde, S. S., Blanchard, J. S. Reversible acetylation and inactivation of *Mycobacterium tuberculosis* acetyl-CoA synthetase is dependent on cAMP. *Biochemistry* 2011, **50**(26): 5883-5892.
195. Yu, M., de Carvalho, L. P., Sun, G., Blanchard, J. S. Activity-based substrate profiling for Gcn5-related N-acetyltransferases: the use of chloroacetyl-coenzyme A to identify protein substrates. *J Am Chem Soc* 2006, **128**(48): 15356-15357.
196. Holm, L., Rosenstrom, P. Dali server: conservation mapping in 3D. *Nucleic Acids Res* 2010, **38**(Web Server issue): W545-549.
197. Green, K. D., Chen, W., Garneau-Tsodikova, S. Identification and characterization of inhibitors of the aminoglycoside resistance acetyltransferase Eis from *Mycobacterium tuberculosis*. *ChemMedChem* 2012, **7**(1): 73-77.
198. Chen, W., Green, K. D., Garneau-Tsodikova, S. Cosubstrate tolerance of the aminoglycoside resistance enzyme Eis from *Mycobacterium tuberculosis*. *Antimicrob Agents Chemother* 2012, **56**(11): 5831-5838.
199. Pricer, R. E., Houghton, J. L., Green, K. D., Mayhoub, A. S., Garneau-Tsodikova, S. Biochemical and structural analysis of aminoglycoside acetyltransferase Eis from *Anabaena variabilis*. *Mol Biosyst* 2012, **8**(12): 3305-3313.
200. Chen, W., Green, K. D., Tsodikov, O. V., Garneau-Tsodikova, S. Aminoglycoside multiacetylating activity of the enhanced intracellular survival protein from *Mycobacterium smegmatis* and its inhibition. *Biochemistry* 2012, **51**(24): 4959-4967.
201. Houghton, J. L., Green, K. D., Pricer, R. E., Mayhoub, A. S., Garneau-Tsodikova, S. Unexpected N-acetylation of capreomycin by mycobacterial Eis enzymes. *J Antimicrob Chemother* 2013, **68**(4): 800-805.

202. Labby, K. J., Garneau-Tsodikova, S. Strategies to overcome the action of aminoglycoside-modifying enzymes for treating resistant bacterial infections. *Future Med Chem* 2013, **5**(11): 1285-1309.
203. Jennings, B. C., Labby, K. J., Green, K. D., Garneau-Tsodikova, S. Redesign of substrate specificity and identification of the aminoglycoside binding residues of Eis from *Mycobacterium tuberculosis*. *Biochemistry* 2013, **52**(30): 5125-5132.
204. Kim, K. H., An, D. R., Song, J., Yoon, J. Y., Kim, H. S., Yoon, H. J., Im, H. N., Kim, J., Kim do, J., Lee, S. J., Kim, K. H., Lee, H. M., Kim, H. J., Jo, E. K., Lee, J. Y., Suh, S. W. *Mycobacterium tuberculosis* Eis protein initiates suppression of host immune responses by acetylation of DUSP16/MKP-7. *Proc Natl Acad Sci U S A* 2012, **109**(20): 7729-7734.